UNIVERSITÀ DEGLI STUDI DI NAPOLI FEDERICO II

DOTTORATO DI RICERCA IN INGEGNERIA AEROSPAZIALE,

NAVALE, E DELLA QUALITÀ (XXI CICLO)

DIPARTIMENTO DI INGEGNERIA AEROSPAZIALE

INDUSTRIAL CFD SIMULATION

OF AERODYNAMIC NOISE

Domenico Caridi

Il Coordinatore:

Ch.mo Prof. Antonio Moccia

Il Tutore:

Ch.mo Prof. Carlo De Nicola

A.A. 2007-2008

ABSTRACT

INDUSTRIAL CFD SIMULATION

OF AERODYNAMIC NOISE

Domenico Caridi

DIPARTIMENTO DI INGEGNERIA AEROSPAZIALE

Real challenges to suppress undesirable fluid-excited acoustics are posed by a wide variety of engineering disciplines. Noise regulations, passenger comfort and component stability are motivators which are continuing to stimulate substantial efforts towards the understanding of aeroacoustic phenomena, and not least to quantify the usability (practicability and value) of traditional and advanced prediction methods. The latter is the primary focus of this thesis, particularly as applied to the transportation industries, aerospace, automotive and rail.

Nowadays Computational Fluid Dynamics (CFD) is a tool well integrated into the industrial development and production life-cycles. This is possible now because of two main factors: the increase in the performance of relatively cheap personal computers and network facilities, and the progress made in general purpose CFD software between modeling complexity and practicability within the industrial environment.

While CFD methodologies are well established for lots of applications such as aerodynamics, heat exchange, etc., aeroacoustic CFD simulations still represent a challenge, in particular their industrial practicability. In these years this has given rise to heavy investments by the automotive industry in international aeroacoustics consortia, whereby all the major car companies work together to study the limitations and advantages of aeroacoustics CFD. The general aim of these consortia is to develop methodologies which fit into, and improve upon, current design processes.

The goal of the present work is to explore the multitude of different CFD modeling approaches for some typical industrial problems such as: cavity noise, vortex shedding noise, propeller and jet noise. Each of these problems has a particular mechanism for noise generation and different methods have been studied and tested, in order to develop and optimize a practical methodology for the analysis of each problem type. Furthermore each of the aeroacoustics problems considered are representative of a variety of industrial applications. Cavity noise is at the origin of phenomena such as sun-roof buffeting in convertibles or door-gap tonal noise. Vortex shedding noise is typical of any flows involving bluff bodies such as automobile antennas or aircraft landing gear. Propeller noise is typical to applications involving rotating machinery, such as fans, pumps and turbines.

Different approaches ranging from steady and transient RANS simulations with the acoustic analogy (including porous and solid surface formulations), to Computational Aero Acoustics (CAA) and Large Eddy Simulation (LES) type computations have been studied and applied.

Classic theories already exist to predict aerodynamically generated noise, which are both computationally and economically less expensive than CFD methods. However aeroacoustics CFD is the future, beginning as a promising present, for the following reasons:

- Industries are interested in modeling complex geometries.

- Many classic theories can be applied successfully but very often restrictions exist with respect to the configuration and flow conditions. For example, classic propeller theories cannot be used to model real-world configurations such as a propeller installed on a wing with some prescribed yaw or angle of attack.

- The progress of all other Computer Aided Design and Engineering tools, such as linear or non-linear structural codes, are driving design towards a virtual multi-physics approach for the simulation of complex geometries.

Due to previous experience and the wide availability of modeling options, it was decided to use the general purpose CFD software package ANSYS FLUENT for CFD investigations in this study.

ACKNOWLEDGMENTS

TABLE OF CONTENTS

NOMENCLATURE

c	speed of sound [m/s]
C_d	drag coefficient
d	diameter [m]
G	green function
k	turbulence kinetic energy [m^2/s^2]
M	Mach number
n	surface normal vector
p	pressure [Pa]
p_{ref}	reference pressure [Pa]
P	production of turbulent kinetic energy [kg/(m s^2)]
R	ideal gas constant [J/mol/K]
Re	Reynolds number
St	Strouhal number
t	time [s]
T	temperature [K] or [°C]
T$_j$	jet core temperature [K] or [°C]
T_{ij}	Lighthill stress tensor components [N/m^2]

U_j	axial jet velocity [m/s]
u_i	velocity component in the i direction [m/s]
x_i	coordinate vector [m]
y+	normalized wall coordinate
β	blade angle at 75 % of blade radius [degree]
δ{ij}	Kronecker delta tensor [dimensionless]
ε	turbulence dissipation rate [m^2/s^3]
λ	wavelength [m]
μ	dynamic viscosity [kg/(m s)]
μ_t	dynamic turbulence viscosity [kg/(m s)]
υ	kinematic viscosity [m^2/s]
ρ	density [kg/m^3]
τ	retarded time [s]
τ_{ij}	stress tensor components [N/m^2]
τ_w	wall shear stress [N/m^2]
prime (')	fluctuating quantity
overbar (⁻)	time averaged quantity

ACRONYMS

2D	Two Dimension
3D	Three Dimension
BL	Boundary Layer
CAA	Computational Aero Acoustics
CFL	Courant Number
CFD	Computational Fluid Dynamics
DES	Detached Eddy Simulation
DNS	Direct Numerical Simulation
FFT	Fast Fourier Transform
FW-H	Ffowcs Williams and Hawkings
LBL	Laminar Boundary Layer
LES	Large Eddy Simulation
MRF	Moving Reference Frame
MUSCL	Monotone Upstream-Centered Schemes for Conservation Laws
OPSL	Overall Sound Pressure Level
PBCS	Pressure Based Coupled Solver
NRBC	Non Reflective Boundary Condition

PISO   Pressure-Implicit with Splitting of Operators

PRESTO   PREssure STaggering Option

QUICK   Quadratic Upstream Interpolation for Convective Kinematics

RANS   Reynolds-Averaged Navier-Stokes

RMS   Root-Mean-Square

RSM   Reynolds Stress Model

SIMPLE   Semi-Implicit Pressure Linked Equations

SLM   Sliding Mesh

SPL   Sound Pressure Level

TBL   Turbulent Boundary Layer

TE   Trailing Edge

TI   Turbulent Intensity [%]

TKE   Turbulent Kinetic Energy [m^2/s^2]

UDF   User-Defined Function

VS   Vortex Shedding

1 ACOUSTICS FUNDAMENTALS

To provide the necessary background for the understanding of the topics covered in this thesis, basic definitions and other aspects related to the physics of sound and noise are presented. Most definitions have been internationally standardized and are listed in standards publications such as IEC 60050-801(1994).

1.1 PHYSICS OF SOUND

Noise can be defined as "disagreeable or undesired sound" or other disturbance. From the acoustics point of view, sound and noise constitute the same phenomenon of atmospheric pressure fluctuations about the mean atmospheric pressure; the differentiation is greatly subjective. What is sound to one person can very well be noise to somebody else.

Sound (or noise) is the result of pressure variations, or oscillations, in an elastic medium (e.g., air, water, solids), generated by a vibrating surface, or turbulent fluid flow. Sound propagates in the form of longitudinal (as opposed to transverse) waves, involving a succession of compressions and rarefactions in the elastic medium, as illustrated by Figure 1-1(a). When a sound wave propagates in air (which is the medium considered in this document), the oscillations in pressure are above and below the ambient atmospheric pressure.
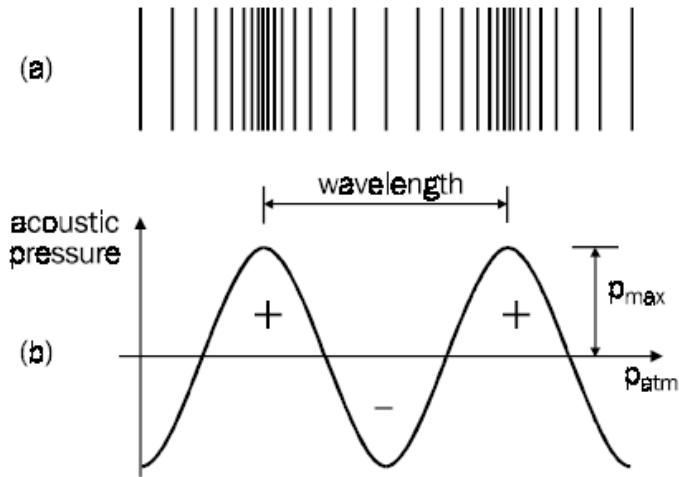
Figure 1-1 Representation of a sound wave.
(a) compressions and rarefactions caused in air by the sound wave.
(b) graphic representation of pressure variations above and below atmospheric pressure.
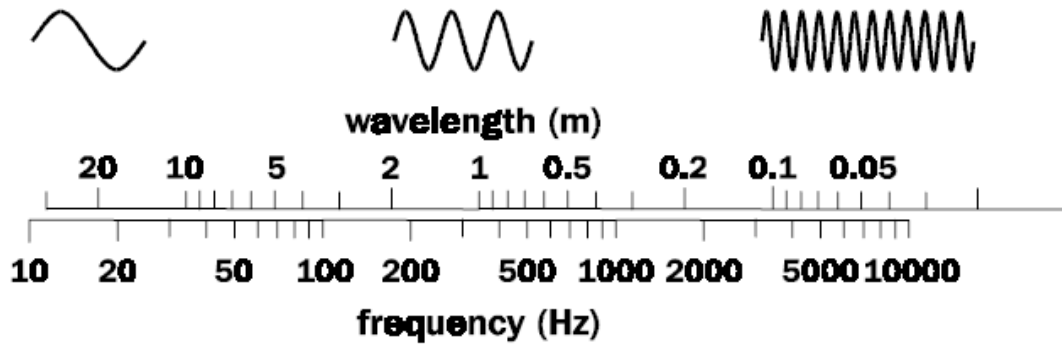
Figure 1-2 Wavelength in air versus frequency.

2

The speed of sound propagation, c, the frequency, f, and the wavelength, λ, are related by the following equation:

$$c = f\lambda$$

(1.1)

the speed of propagation, c, of sound in air is 343 m/s, at 20 °C and 1 atmosphere pressure. At other temperatures (not too different from 20 °C), it may be calculated using:

$$c = 332 + 0.6Tc$$

(1.2)

where Tc is the temperature in °C. Alternatively, making use of the equation of state for gases, the speed of sound may be written as:

$$c = \sqrt{\gamma R T_k / M}$$

(1.3)

where T_k is the temperature in K, R is the universal gas constant which has the value 8.314 J per mole K, and M is the molecular weight, which for air is 0.029 kg/mole. For air, the ratio of specific heats, γ, is 1.402.

All of the properties just discussed (except the speed of sound) apply only to a pure tone (single frequency) sound which is described by the oscillations in pressure shown in Figure 1-1. However, sounds usually encountered are not pure tones. In general, sounds are complex mixtures of pressure variations that vary with respect to phase, frequency, and amplitude. For such complex sounds, there is no simple mathematical relation between the different characteristics. However, any signal may be considered as a combination of a certain number (possibly infinite) of sinusoidal waves, each of which may be described as outlined above. These sinusoidal components constitute the

3

frequency spectrum of the signal. To illustrate longitudinal wave generation, as well as to provide a model for the discussion of sound spectra, the example of a vibrating piston at the end of a very long tube filled with air will be used, as illustrated in Figure 1-3.
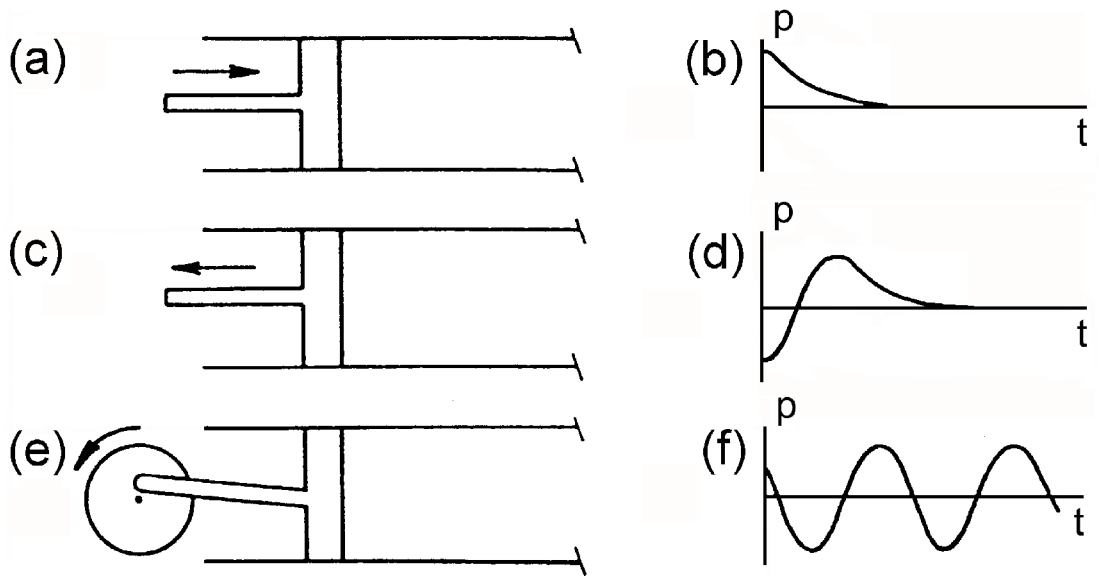
Figure 1-3 Wavelength in air versus frequency under normal Sound generation illustrated. (a) The piston moves right, compressing air as in (b). (c) The piston stops and reverses direction, moving left and decompressing air in front of the piston, as in (d). (e) The piston moves cyclically back and forth, producing alternating compressions and rarefactions, as in (f). In all cases disturbances move to the right with the speed of sound.

Let the piston in Figure 1-3 move forward. Since the air has inertia, only the air immediately next to the face of the piston moves at first; the pressure in the element of air next to the piston increases. The element of air under compression next to the piston will expand forward, displacing the next layer of air and compressing the next elemental volume. A pressure pulse is formed which travels down the tube with the speed of sound, c. Let the piston stop and subsequently move backward; a rarefaction is formed next to the surface of the piston which follows the previously formed compression down the tube. If the piston again moves forward, the process is repeated with the net result being a "wave" of positive and negative pressure transmitted along the tube.
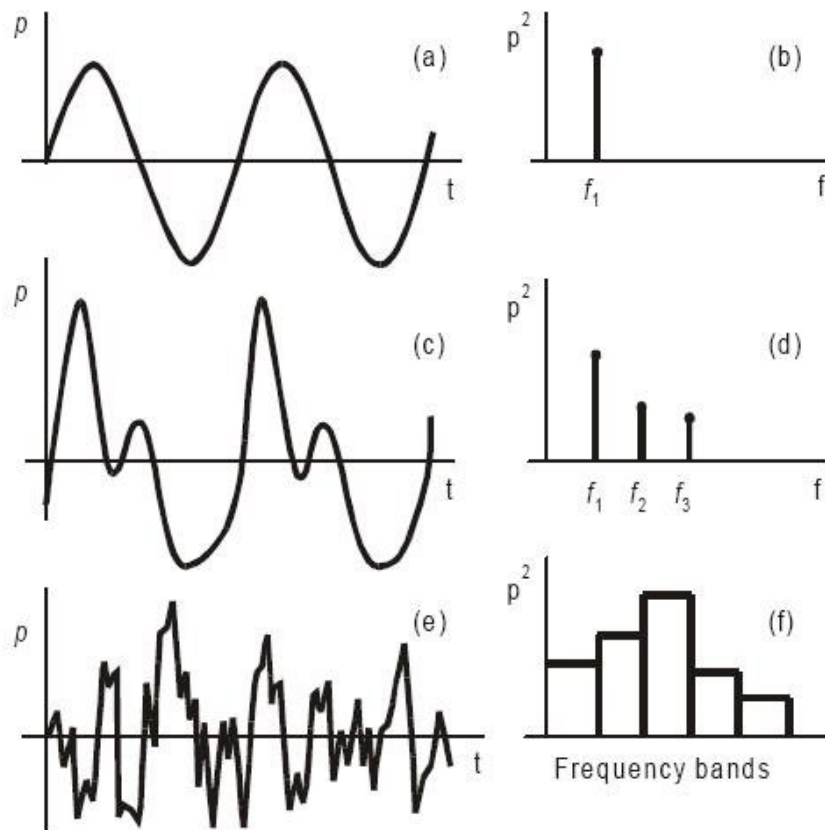
Figure 1-4 Spectral analysis illustrated. (a) Disturbance p varies sinusoidally with time t at a single frequency f1, as in (b). (c) Disturbance p varies cyclically with time t as a combination of three sinusoidal disturbances of fixed relative amplitudes and phases; the associated spectrum has three single-frequency components f1, f2 and f3, as in (d). (e) Disturbance p varies erratically with time t, with a frequency band spectrum as in (f).

If the piston moves with simple harmonic motion, a sine wave is produced; that is, at any instant the pressure distribution along the tube will have the form of a sine wave, or at any fixed point in the tube the pressure disturbance, displayed as a function of time, will have a sine wave appearance. Such a disturbance is characterized by a single frequency. The motion and corresponding spectrum are illustrated in Figure 1-4a and b.

If the piston moves irregularly but cyclically, for example, so that it produces the waveform shown in Figure 1-4c, the resulting sound field will consist of a combination of sinusoids of several frequencies. The spectral (or frequency) distribution of the energy in

this particular sound wave is represented by the frequency spectrum of Figure 1-4d. As the motion is cyclic, the spectrum consists of a set of discrete frequencies.

Although some sound sources have single-frequency components, most sound sources produce a very disordered and random waveform of pressure versus time, as illustrated in Figure 1-4e. Such a wave has no periodic component, but by Fourier analysis it can be shown that the resulting waveform may be represented as a collection of waves of all frequencies. For a random type of wave the sound pressure squared in a band of frequencies is plotted as shown in the frequency spectrum of Figure 1-4f.

It is customary to refer to spectral density level when the measurement band is one Hz wide, to one third octave or octave band level when the measurement band is one third octave or one octave wide and to spectrum level for measurement bands of other widths.

Two special kinds of spectra are commonly referred to as white random noise and pink random noise. White random noise contains equal energy per hertz and thus has a constant spectral density level. Pink random noise contains equal energy per measurement band and thus has an octave or one-third octave band level which is constant with frequency.

1.2 SOUND FIELD DEFINITIONS

Following Sound Field Definitions. For more detail see *ISO 12001*.

1.2.1 Free Field

The free field is a region in space where sound may propagate free from any form of obstruction.

1.2.2 Near Field

The near field of a source is the region close to a source where the sound pressure and acoustic particle velocity are not in phase. In this region the sound field does not decrease by 6 dB each time the distance from the source is doubled. The near field is limited to a distance from the source equal to about a wavelength of sound or equal to three times the largest dimension of the sound source (whichever is the larger).

1.2.3 Far Field

The far field of a source begins where the near field ends and extends to infinity. Note that the transition from near to far field is gradual in the transition region. In the far field, the direct field radiated by most machinery sources will decay at the rate of 6 dB each time the distance from the source is doubled. For line sources such as traffic noise, the decay rate varies between 3 and 4 dB.

1.2.4 Direct Field

The direct field of a sound source is defined as that part of the sound field which has not suffered any reflection from any room surfaces or obstacles.

1.2.5 Reverberant Field

The reverberant field of a source is defined as that part of the sound field radiated by a source which has experienced at least one reflection from a boundary of the room or enclosure containing the source.

1.2.6 Frequency Analysis

Frequency analysis may be thought of as a process by which a time varying signal in the time domain is transformed to its frequency components in the frequency domain. It can be used for quantification of a noise problem, as both criteria and proposed controls are frequency dependent. In particular, tonal components which are identified by the analysis may be treated somewhat differently than broadband noise. Sometimes frequency analysis is used for noise source identification and in all cases frequency analysis will allow determination of the effectiveness of controls.

There are a number of instruments available for carrying out a frequency analysis of arbitrarily time-varying signals . To facilitate comparison of measurements between instruments, frequency analysis bands have been standardized. Thus the International Standards Organization has agreed upon "preferred" frequency bands for sound measurement and analysis.

The widest band used for frequency analysis is the octave band; that is, the upper frequency limit of the band is approximately twice the lower limit. Each octave band is described by its "centre frequency", which is the geometric mean of the upper and lower frequency limits. The preferred octave bands are shown in the Table of Figure 1-5, in terms of their centre frequencies. Occasionally, a little more information about the detailed structure of the noise may be required than the octave band will provide. This

can be obtained by selecting narrower bands; for example, one-third octave bands. As the name suggests, these are bands of frequency approximately one-third of the width of an octave band. Preferred one-third octave bands of frequency have been agreed upon and are also shown in the Table of Figure 1-5.

Instruments are available for other forms of band analysis. However, they do not enjoy the advantage of standardization so that the inter-comparison of readings taken on such instruments may be difficult. One way to ameliorate the problem is to present such readings as mean levels per unit frequency. Data presented in this way are referred to as "Spectral Density Levels" as opposed to band levels. In this case the measured level is reduced by ten times the logarithm to the base ten of the bandwidth. For example, referring to the Table of Figure 1-5, if the 500 Hz octave band which has a bandwidth of 354 Hz were presented in this way, the measured octave band level would be reduced by $10 \log 10 (354) = 25.5$ dB to give an estimate of the spectral density level at 500 Hz.

The problem is not entirely alleviated, as the effective bandwidth will depend upon the sharpness of the filter cut-off, which is also not standardized. Generally, the bandwidth is taken as lying between the frequencies, on either side of the pass band, at which the signal is down 3 dB from the signal at the centre of the band.

There are two ways of transforming a signal from the time domain to the frequency domain. The first involves the use of band limited digital or analog filters. The second involves the use of Fourier analysis where the time domain signal is transformed using a Fourier series. This is implemented in practice digitally (referred to as the DFT - digital Fourier Transform) using a very efficient algorithm known as the FFT (Fast Fourier Transform).

9

1.2.6.1   A convenient property of the one-third octave band centre frequencies

The one-third octave band centre frequency numbers have been chosen so that their logarithms are one-tenth decade numbers. The corresponding frequency pass bands are a compromise; rather than follow a strictly octave sequence which would not repeat, they are adjusted slightly so that they repeat on a logarithmic scale. For example, the sequence 31.5, 40, 50 and 63 has the logarithms 1.5, 1.6, 1.7 and 1.8. The corresponding frequency bands are sometimes referred to as the 15th, 16th, etc., frequency bands.

Band number	Octave band center frequency	One-third octave band center frequency	Band limits Lower	Upper
14		25	22	28
15	31.5	31.5	28	35
16		40	35	44
17		50	44	57
18	63	63	57	71
19		80	71	88
20		100	88	113
21	125	125	113	141
22		160	141	176
23		200	176	225
24	250	250	225	283
25		315	283	353
26		400	353	440
27	500	500	440	565
28		630	565	707
29		800	707	880
30	1000	1000	880	1130
31		1250	1130	1414
32		1600	1414	1760
33	2000	2000	1760	2250
34		2500	2250	2825
35		3150	2825	3530
36	4000	4000	3530	4400
37		5000	4400	5650
38		6300	5650	7070
39	8000	8000	7070	8800
40		10000	8800	11300
41		12500	11300	14140
42	16000	16000	14140	17600
43		20000	17600	22500

NOTE: Requirements for filters see IEC 61260; there index numbers are used instead of band numbers. The index numbers are not identical, starting with No. "0" at 1 kHz.

Figure 1-5 Frequency Band Table.

11

1.3 QUANTIFICATION OF SOUND

1.3.1 Sound Power (*W*) and Intensity (*I*)

The Sound intensity is a vector quantity determined as the product of sound pressure and the component of particle velocity in the direction of the intensity vector. It is a measure of the rate at which work is done on a conducting medium by an advancing sound wave and thus the rate of power transmission through a surface normal to the intensity vector. It is expressed as watts per square meter (W/m^2). In a free-field environment, i.e., no reflected sound waves and well away from any sound sources, the sound intensity is related to the root mean square acoustic pressure as follows

$$I = \frac{p_{rms}^2}{\rho c}$$

(1.4)

where ρ is the density of air (kg/m^3), and c is the speed of sound (m/sec). The quantity, ρc is called the "acoustic impedance" and is equal to 414 Ns/m³ at 20° C and one atmosphere. At higher altitudes it is considerably smaller.

The total sound energy emitted by a source per unit time is the sound power, W, which is measured in watts. It is defined as the total sound energy radiated by the source in the specified frequency band over a certain time interval divided by the interval. It is obtained by integrating the sound intensity over an imaginary surface surrounding a source. Thus, in general the power, *W*, radiated by any acoustic source is,

$$W = \int_A \vec{I} \cdot \vec{n} \, dA$$

(1.5)

12

the where the dot multiplication of $\vec{I}$ with the unit vector, $\vec{n}$, indicates that it is the intensity component normal to the enclosing surface which is used. Most often, a convenient surface is an encompassing sphere or spherical section, but sometimes other surfaces are chosen, as dictated by the circumstances of the particular case considered. For a sound source producing uniformly spherical waves (or radiating equally in all directions), a spherical surface is most convenient, and in this case the above equation leads to the following expression:

$$W = 4\pi r^2 I$$

(1.6)

where the magnitude of the acoustic intensity, I, is measured at a distance r from the source. In this case the source has been treated as though it radiates uniformly in all directions.

1.3.2   Sound Pressure Level

The range of sound pressures that can be heard by the human ear is very large. The minimum acoustic pressure audible to the young human ear judged to be in good health, and unsullied by too much exposure to excessively loud music, is approximately 20×10^{-6} Pa, or 2×10^{-10} atmospheres (since 1 atmosphere equals 101.3×10^{3} Pa). The minimum audible level occurs at about 4,000 Hz and is a physical limit imposed by molecular motion. Lower sound pressure levels would be swamped by thermal noise due to molecular motion in air.

For the normal human ear, pain is experienced at sound pressures of the order of 60 Pa or 6 x 10^{-4} atmospheres. Evidently, acoustic pressures ordinarily are quite small fluctuations about the mean.

A linear scale based on the square of the sound pressure would require 1013 unit divisions to cover the range of human experience; however, the human brain is not organized to encompass such a range. The remarkable dynamic range of the ear suggests that some kind of compressed scale should be used. A scale suitable for expressing the square of the sound pressure in units best matched to subjective response is logarithmic rather than linear. Thus a unit named the Bel was introduced which is the logarithm of the ratio of two quantities, one of which is a reference quantity.

To avoid a scale which is too compressed over the sensitivity range of the ear, a factor of 10 is introduced, giving rise to the decibel. The level of sound pressure p is then said to be Lp decibels (dB) greater or less than a reference sound pressure p_{ref} according to the following equation:

$$L_p = 10\log_{10}\frac{p_{rms}^{\,2}}{p_{ref}^{\,2}} = 20\log_{10}\frac{p_{rms}}{p_{ref}} = 20\log_{10} p_{rms} - 20\log_{10} p_{ref} \quad \text{(dB)}$$

(1.7)

For the purpose of absolute level determination, the sound pressure is expressed in terms of a datum pressure corresponding to the lowest sound pressure which the young normal ear can detect. The result is called the sound pressure level, L_p (or SPL), which has the units of decibels (dB). This is the quantity which is measured with a sound level meter.

The sound pressure is a measured root mean square (r.m.s.) value and the internationally agreed reference pressure p_{ref} = 2 x 10^{-5} N m^{-2} or 20 μPa .

14

1.3.3 Sound Intensity Level

A sound intensity level, L_I, may be defined as follows:

$$L_I = 10 \log_{10} \frac{(sound\ intensity)}{(ref.\ sound\ intensity)} = 10 \log_{10} \frac{I}{I_{ref}}\ (\text{dB})$$

(1.8)

An internationally agreed reference intensity, I_{ref}, is 10^{-12} Wm^{-2}.

Use of the relationship between acoustic intensity and pressure in the far field of a source gives the following useful result:

$$L_I = L_P + 10 \log_{10} \frac{400}{\rho c}$$

(1.9)

$$L_I = L_P + 26 - 10 \log_{10}(\rho c)\ \ (\text{dB})$$

(1.10)

At sea level and 20°C the characteristic impedance, ρc, is 414 kg m^{-2} s^{-1}, so that for both plane and spherical waves,

$$L_I = L_P - 0.2\ \ (\text{dB})$$

(1.11)

1.3.4 Sound Power Level

The sound power level, L_w (or PWL), may be defined as follows:

$$L_W = 10 \log_{10} \frac{(sound\ power)}{(ref.\ sound\ power)} = 10 \log_{10} \frac{W}{W_{ref}}\ (\text{dB})$$

(1.12)

15

The internationally agreed reference power is 10^{-12} W.

1.3.5 Combining Sound Pressures

1.3.5.1 Addition of coherent sound pressures

Often, combinations of sounds from many sources contribute to the observed total sound. In general, the phases between sources of sound will be random and such sources are said to be incoherent. However, when sounds of the same frequency are to be combined, the phase between the sounds must be included in the calculation.

For two sounds of the same frequency, characterized by mean square sound pressures p^2_{1rms} and p^2_{2rms} and phase difference $\beta_1 - \beta_2$, the total mean square sound pressure is given by the following expression [43]:

$$p^2_{t rms} = p^2_{1rms} + p^2_{2rms} + 2[p_1 p_2]_{rms} \cos(\beta_1 - \beta_2)$$

(1.13)

When two sounds of slightly different frequencies are added an expression similar to that given by the above equation is obtained but with the phase difference replaced with the frequency difference, Δ, multiplied by time, t. In this case the total mean square sound pressure rises and falls cyclically with time and the phenomenon known as beating is observed, as illustrated in Figure 1-7.
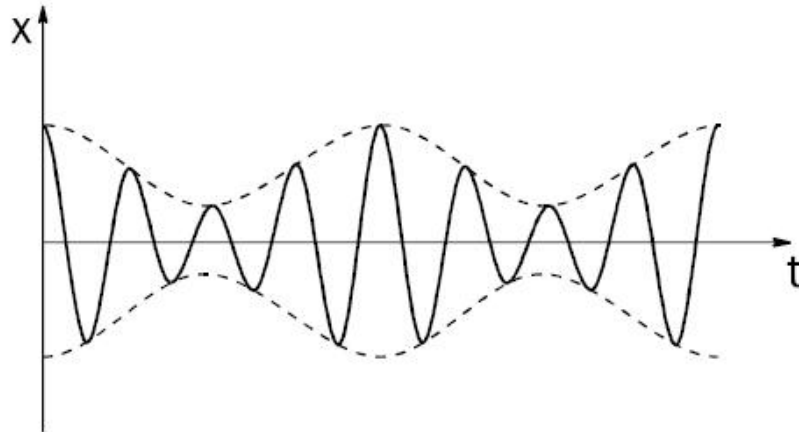
16

Figure 1-7 Illustration of beating.

1.3.5.2   Addition of incoherent sound pressures (logarithmic addition)

When bands of noise are added and the phases are random, the limiting form of the previous equation reduces to the case of addition of incoherent sounds; that is [43]:

$$p^2{}_{t_{rms}} = p^2{}_{1_{rms}} + p^2{}_{2_{rms}}$$

(1.14)

Incoherent sounds add together on a linear energy (pressure squared) basis. A simple procedure which may easily be performed on a standard calculator will be described. The procedure accounts for the addition of sounds on a linear energy basis and their representation on a logarithmic basis. Note that the division by 10 in the exponent is because the process involves the addition of squared pressures.

It should be noted that the addition of two or more levels of sound pressure has a physical significance only if the levels to be added were obtained in the same measuring point.

17

Example

Assume that three sounds of different frequencies (or three incoherent noise sources) are to be combined to obtain a total sound pressure level. Let the three sound pressure levels be (a) 90 dB, (b) 88 dB and (c) 85 dB. The solution is obtained by use of the previous equation.

Solution:

For source (a):

$$p^2_{1rms} = p^2_{ref} \cdot 10^{90/10} = p^2_{ref} \cdot 10 \cdot 10^8$$

For source (b):

$$p^2_{2rms} = p^2_{ref} \cdot 6.31 \cdot 10^8$$

For source (c):

$$p^2_{3rms} = p^2_{ref} \cdot 3.16 \cdot 10^8$$

The total mean square sound pressure is,

$$p^2_{t rms} = p^2_{1rms} + p^2_{2rms} + p^2_{3rms} = p^2_{ref} \cdot 19.47 \cdot 10^8$$

The total sound pressure level is,

$$L_{pt} = 10 \log_{10} \frac{p_{t rms}^2}{p_{ref}^2} = 10 \log_{10}(19.47 \cdot 10^8) = 92.9 \, \text{dB}$$

Alternatively, in short form,

$$L_{pt} = 10 \log_{10}(10^{90/10} + 10^{88/10} + 10^{85/10}) = 92.9 \, \text{dB}$$

The Table of Figure 1-8 can be used as an alternative for adding combinations of decibel values. As an example, if two independent noises with levels of 83 and 87 dB are produced at the same time at a given point, the total noise level will be 87 + 1.5 = 88.5

dB, since the amount to be added to the higher level, for a difference of 4 dB between the two levels, is 1.5 dB.

Difference between the two db levels to be added										dB
0	1	2	3	4	5	6	7	8	9	10
3.0	*2.5*	*2.1*	*1.8*	*1.5*	*1.2*	*1.0*	*0.8*	*0.6*	*0.5*	*0.4*
Amount to be added to the higher level in order to get the total level										*dB*

Figure 1-8 Table for combining decibel levels.

As can be seen in these examples, it is only when two noise sources have similar acoustic powers, and are therefore generating similar levels, that their combination leads to an appreciable increase in noise levels above the level of the noisier source. The maximum increase over the level radiated by the noisier source, by the combination of two random noise sources occurs when the sound pressures radiated by each of the two sources are identical, resulting in an increase of 3 dB over the sound pressure level generated by one source. If there is any difference in the original independent levels, the combined level will exceed the higher of the two levels by less than 3 dB. When the difference between the two original levels exceeds 10 dB, the contribution of the less noisy source to the combined noise level is negligible; the sound source with the lower level is practically not heard.

1.4   PROPAGATION OF NOISE

1.4.1   Free Field

A free field is a homogeneous medium, free from boundaries or reflecting surfaces. Considering the simplest form of a sound source, which would radiate sound equally in all directions from an apparent point, the energy emitted at a given time will diffuse in all directions and, one second later, will be distributed over the surface of a sphere of 340 m radius. This type of propagation is said to be spherical and is illustrated in Figure 1-9.
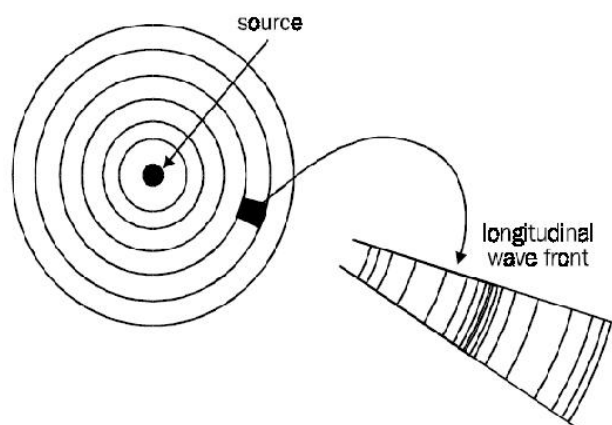

Figure 1-9 A representation of the radiation of sound from a simple source in free field.

In a free field, the intensity and sound pressure at a given point, at a distance r (in meters) from the source, is expressed by the following equation:

$$p^2 = \rho c I = \frac{\rho c W}{4 \pi r^2}$$

(1.15)

where ρ and c are the air density and speed of sound respectively.

In terms of sound pressure the preceding equation can be written as:

$$L_P = L_W + 10\log_{10}\left(\frac{\rho c}{400}\right) - 10\log_{10}(4\pi r^2)$$

(1.16)

which is often approximated as:

$$L_P = L_W - 10\log_{10}(4\pi r^2)$$

(1.17)

Measurements of source sound power, L_W, can be complicated in practice (see [43], Ch. 6). However, if the sound pressure level, L_m, is measured at some reference distance, r_m, from the noise source (usually greater than 1 meter to avoid source near field effects which complicate the sound field close to a source), then the sound pressure level at some other distance, r, may be estimated using:

$$L_P = L_m - 20\log_{10}\left(\frac{r}{r_m}\right)$$

(1.18)

From the preceding expression it can be seen that in free field conditions, the noise level decreases by 6 dB each time the distance between the source and the observer doubles. However, true free-field conditions are rarely encountered in practice, so in general the equation relating sound pressure level and sound power level must be modified to account for the presence of reflecting surfaces. This is done by introducing a directivity factor, Q, which may also be used to characterize the directional sound radiation properties of a source.

1.4.2 Directivity

Provided that measurements are made at a sufficient distance from a source to avoid near field effects (usually greater than 1 meter), the sound pressure will decrease with spreading at the rate of 6 dB per doubling of distance and a directivity factor, Q, may be defined which describes the field in a unique way as a function solely of direction.

A simple point source radiates uniformly in all directions. In general, however, the radiation of sound from a typical source is directional, being greater in some directions than in others. The directional properties of a sound source may be quantified by the introduction of a directivity factor describing the angular dependence of the sound intensity. For example, if the sound intensity I is dependent upon direction, then the mean intensity, I_{av}, averaged over an encompassing spherical surface is introduced and,

$$I_{av} = \frac{W}{4\pi r^2}$$

(1.19)

The directivity factor, Q, is defined in terms of the intensity I_θ in direction (θ, ψ) and the mean intensity [43]:

$$Q_\theta = \frac{I_\theta}{I_{av}}$$

(1.20)

The directivity index is defined as [43]:

$$DI = 10\log_{10} Q_\theta$$

(1.21)

1.4.3 Reflection effects

The presence of a reflecting surface near to a source will affect the sound radiated and the apparent directional properties of the source. Similarly, the presence of a reflecting surface near to a receiver will affect the sound received by the receiver. In general, a reflecting surface will affect not only the directional properties of a source but also the total power radiated by the source. As the problem can be quite complicated the simplifying assumption is often made and will be made here, that the source is of constant power output which means that its output sound power is not affected by reflecting surfaces (see [43] for a more detailed discussion).

For a simple source near to a reflecting surface outdoors ([43], Ch. 5):

$$W = I \frac{4\pi r^2}{Q} = p^2{}_{rms} \frac{4\pi r^2}{\rho c Q}$$

(1.22)

which may be written in terms of levels as

$$L_P = L_W + 10\log_{10}\left(\frac{Q}{4\pi r^2}\right) = L_W + 10\log_{10}\left(\frac{1}{4\pi r^2}\right) + DI$$

(1.23)

For a uniformly radiating source, the intensity I is independent of angle in the restricted region of propagation, and the directivity factor Q takes the value listed in the Table of Figure 1-10. For example, the value of Q for the case of a simple source next to a reflecting wall is 2, showing that all of the sound power is radiated into the half-space defined by the wall.

Situation	Directivity factor, Q	Directivity Index, DI (dB)
free space	1	0
centred in a large flat surface	2	3
centred at the edge formed by the junction of two large flat surfaces	4	6
at the corner formed by the junction of three large flat surfaces	8	9

Figure 1-10 Table of Directivity factors for a simple source near reflecting surfaces.

1.4.4   Reverberant fields

Whenever sound waves encounter an obstacle, such as when a noise source is placed within boundaries, part of the acoustic energy is reflected, part is absorbed and part is transmitted. The relative amounts of acoustic energy reflected, absorbed and transmitted greatly depend on the nature of the obstacle. Different surfaces have different ways of reflecting, absorbing and transmitting an incident sound wave. A hard, compact, smooth surface will reflect much more, and absorb much less, acoustic energy than a porous, soft surface.

If the boundary surfaces of a room consist of a material which reflects the incident sound, the sound produced by a source inside the room - the direct sound - rebounds from one boundary to another, giving origin to the reflected sound. The higher the proportion of the incident sound reflected, the higher the contribution of the reflected sound to the total sound in the closed space.

This "built-up" noise will continue even after the noise source has been turned off. This phenomenon is called reverberation and the space where it happens is called a reverberant sound field, where the noise level is dependent not only on the acoustic power radiated, but also on the size of the room and the acoustic absorption properties of the boundaries. As the surfaces become less reflective, and more absorbing of noise, the reflected noise becomes less and the situation tends to a "free field" condition where the only significant sound is the direct sound. By covering the boundaries of a limited space with materials which have a very high absorption coefficient, it is possible to arrive at characteristics of sound propagation similar to free field conditions. Such a space is called an anechoic chamber, and such chambers are used for acoustical research and sound power measurements.

In practice, there is always some absorption at each reflection and therefore most work spaces may be considered as semi-reverberant.

The phenomenon of reverberation has little effect in the area very close to the source, where the direct sound dominates. However, far from the source, and unless the walls are very absorbing, the noise level will be greatly influenced by the reflected, or indirect, sound. The sound pressure level in a room may be considered as a combination of the direct field (sound radiated directly from the source before undergoing a reflection) and the reverberant field (sound which has been reflected from a surface at least once) and for a room for which one dimension is not more than about five times the other two, the sound pressure level generated at distance r from a source producing a sound power level of L_W may be calculated using ([43], Ch. 7):

$$L_P = L_W + 10\log_{10}\left(\frac{Q}{4\pi r^2} + \frac{4(1-\overline{\alpha})}{S\overline{\alpha}}\right)$$

(1.24)

Where $\overline{\alpha}$ is the average absorption coefficient of all surfaces in the room.
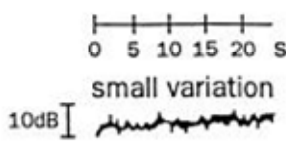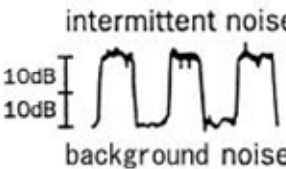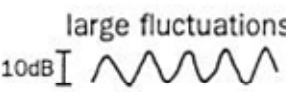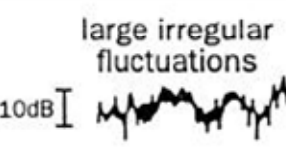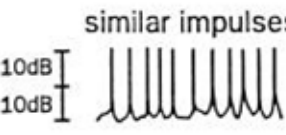
1.4.5 Types of Noise

Noise may be classified as steady, non-steady or impulsive, depending upon the temporal variations in sound pressure level (see ISO 12001). The various types of noise and instrumentation required for their measurement are illustrated in the Table of Figure 1-11.

Steady noise is a noise with negligibly small fluctuations of sound pressure level within the period of observation. If a slightly more precise single-number description is needed, assessment by NR (Noise Rating) curves may be used.

A noise is called **non-steady** when its sound pressure levels shift significantly during the period of observation. This type of noise can be divided into intermittent noise and fluctuating noise.

Fluctuating noise is a noise for which the level changes continuously and to a great extent during the period of observation.

Tonal noise may be either continuous or fluctuating and is characterized by one or two single frequencies. This type of noise is much more annoying than broadband noise characterized by energy at many different frequencies and of the same sound pressure level as the tonal noise.

26

	Characteristics	Type of Source
small variation — 0 5 10 15 20 S — 10dB	Constant continuous sound	Pumps, electric motors, gearboxes, conveyers
intermittent noise — 10dB 10dB — **background noise**	Constant but intermittent sound	Air compressor, automatic machineryduring a work cycle
large fluctuations — 10dB	Periodically fluctuating sound	Mass production, surface grinding
large irregular fluctuations — 10dB	Fluctuating non-periodic sound	Manual work, grinding, welding, component assembly
similar impulses — 10dB 10dB	Repeated impulses	Automatic press, pneumatic drill, riveting
isolated impulse — 10dB 10dB	Single impulse	Hammer blow, material handling, punch press, gunshot, artillery fire

Noise characteristics classified according to the way they vary with time. Constant noise remains within 5 dB for a long time. Constant noise which starts and stops is called intermittent. Fluctuating noise varies significantly but has a constant long term average ($L_{Aeq,T}$). Impulse noise lasts for less than one second.

Figure 1-11 Table of noise types and their measurement.

27

Intermittent noise is noise for which the level drops to the level of the background noise several times during the period of observation. The time during which the level remains at a constant value different from that of the ambient background noise must be one second or more.

This type of noise can be described by

- o   the ambient noise level

- o   the level of the intermittent noise

- o   the average duration of the on and off period.

In general, however, both levels are varying more or less with time and the intermittence rate is changing, so that this type of noise is usually assimilated to a fluctuating noise as described below, and the same indices are used.

Impulsive noise consists of one or more bursts of sound energy, each of a duration less than about 1s. Impulses are usually classified as type A and type B as described in Figure 1-12, according to the time history of instantaneous sound pressure (ISO 10843). Type A characterizes typically gun shot types of impulses, while type B is the one most often found in industry (e.g., punch press impulses). The characteristics of these impulses are the peak pressure value, the rise time and the duration (as defined in Figure 1-12) of the peak.
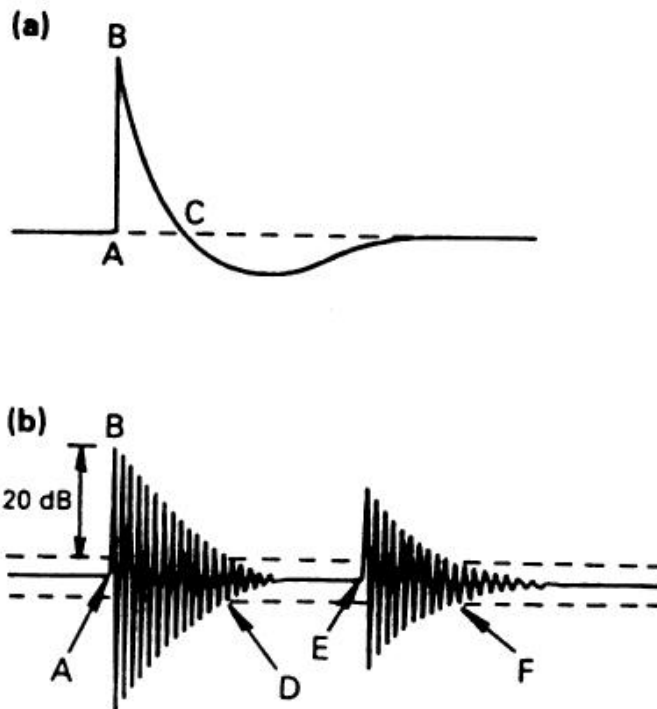
Figure 1-12 Idealized waveforms of impulse noises. Peak level = pressure difference AB; rise time = time difference AB; A duration = time difference AC; B duration = time difference AD (+ EF when a reflection is present). (a) Explosive generated noise. (b) Impact generated noise.

2   AERODYNAMIC SOUND

In contrast to computational aerodynamics, which has advanced to a fairly mature state, computational aeroacoustics (CAA) has only recently emerged as a separate area of study. Due to the nonlinearity of the governing equations it is very difficult to predict the sound production of fluid flows. This sound production occurs typically at high speed flows, for which nonlinear inertial terms in the equation of motion are much larger than the viscous terms (high Reynolds numbers). As sound production represents only a very minute fraction of the energy in the flow the direct prediction of sound generation is very difficult. This is particularly dramatic in free space and at low subsonic speeds. The fact that the sound field is in some sense a small perturbation of the flow, can, however, be used to obtain approximate solutions. Aero-acoustics provides such approximations and at the same time a definition of the acoustical field as an extrapolation of an ideal reference flow. The difference between the actual flow and the reference flow is identified as a source of sound. This idea was introduced by Lighthill who called this an analogy. While in acoustics of quiescent media it is rather indifferent whether we consider a wave equation for the pressure or the density, in aero-acoustics the choice of a different variable corresponds to a different choice of the reference flow and hence to another analogy [47].

2.1 HOMOGENOUS WAVE PROPAGATION

In order to make a simplification, let us consider a zero averaged flow field and the viscosity effects negligible. Since to an acoustic wave are related fluctuations of all the motion variables, each quantity can be considered the sum of an averaged component and a fluctuating component, usually called the acoustic component:

$$p(\vec{x},t) = \bar{p} + p'(\vec{x},t)$$
$$\rho(\vec{x},t) = \bar{\rho} + \rho'(\vec{x},t)$$
$$u_i(\vec{x},t) = \bar{u}_i + u_i'(\vec{x},t)$$

(2.1)

Because of the hypothesis on the averaged flow field, $\bar{u}_i = 0$, the quantities $\bar{p}$ and $\bar{\rho}$ have to be considered constants. Thanks to these assumptions and neglecting the higher order terms, the Navier Stokes equations can be linearized:

$$\frac{\partial \rho'}{\partial t} + \bar{\rho} \frac{\partial u_i'}{\partial x_i} = 0$$

(2.2)

$$\bar{\rho} \frac{\partial u_i'}{\partial t} + \frac{\partial \rho'}{\partial x_i}$$

(2.3)

assuming the air to be a perfect gas ($p = \rho R T$)

$$p' = c_o^2 \rho'$$

(2.4)

32

Taking the time derivative of the 2.2, and the divergence of 2.3 and then subtracting the first from the second:

$$\frac{\partial^2 \rho'}{\partial t^2} - \frac{\partial^2 p'}{\partial x_i^{\,2}} = 0$$

$$(2.5)$$

Applying the relation 2.4 to the equation 2.5 it is possible to obtain an homogeneous equation for the pressure fluctuation:

$$\frac{1}{c_o^{\,2}} \frac{\partial^2 p'}{\partial t^2} - \frac{\partial^2 p'}{\partial x_i^{\,2}} = 0$$

$$(2.6)$$

In a mono-dimensional case a solution of this equation is:

$$p(x,t) = f_1(c_o t - x) + f_2(c_o t + x)$$

$$(2.7)$$

where f_1 and f_2 are two arbitrarily functions.

2.2 NON-HOMOGENEOUS WAVE PROPAGATION

The theories that describes the aerodynamic sound often lead to a non-homogeneous wave equation. For a better understanding of these theories, the purpose of this section is to give a brief introduction to the way of solving a non-homogenous wave equation. In general a wave equation assumes the following form:

$$\left(\frac{1}{c_o^{\,2}} \frac{\partial^2}{\partial t^2} - \nabla^2 \right) p = f(\vec{x},t)$$

$$(2.8)$$

33

Where c_o is the wave speed propagation and $f(\vec{x},t)$ is a generic distribution of sources. In order to solve this equation there is the need to use the Green function, which is defined as the solution of the wave equation related to a punctual and impulsive source, localized in the point $\vec{x} = \vec{y}$, that exists only at time $t = \tau$. The Green function is the solution of the differential equation:

$$\left(\frac{1}{c_o^{\,2}} \frac{\partial^2}{\partial t^2} - \nabla^2 \right) G = \delta(\vec{x} - \vec{y}) \delta(t - \tau)$$

(2.9)

which leads to the following result,

$$G(\vec{x}, \vec{y}, t - \tau) = \frac{1}{4\pi |\vec{x} - \vec{y}|} \delta \left(t - \tau - \frac{|\vec{x} - \vec{y}|}{c_o} \right)$$

(2.10)

The analysis of the Green function shows that it represents a spherical impulsive wave which expands at the speed c_o starting from the point $\vec{y}$. The wave amplitude has an inverse proportionality with a distance $|\vec{x} - \vec{y}|$ from the point $\vec{y}$. If we consider $f(\vec{x},t)$ a generically distribution of infinitesimal impulsive sources, we have:

$$f(\vec{x},t) = \iint f(\vec{y}, \tau) \delta(\vec{x} - \vec{y}) \delta(t - \tau) dV(\vec{y}) d\tau$$

(2.11)

The solution of the wave equation of the type

$$f(\vec{y}, \tau) \delta(\vec{x} - \vec{y}) \delta(t - \tau) dV(\vec{y}) d\tau$$

(2.12)

34

is given by the wave

$$f(\vec{y},\tau)G(\vec{x},\vec{y},t-\tau)dV(\vec{y})d\tau$$

(2.13)

Summing all the contributions, it's possible to obtain a solution for the non-homogeneous wave equation:

$$p(\vec{x},t) = \iint_{\infty} f(\vec{y},\tau)G(\vec{x},\vec{y},t-\tau)dV(\vec{y})d\tau = \frac{1}{4\pi}\iint_{\infty} \frac{f(\vec{y},\tau)}{|\vec{x}-\vec{y}|}\delta\left(t-\tau-\frac{|\vec{x}-\vec{y}|}{c_o}\right)dV(\vec{y})d\tau =$$

$$= \frac{1}{4\pi}\iint_{\infty} \frac{f\left(\vec{y},t-\frac{|\vec{x}-\vec{y}|}{c_o}\right)}{|\vec{x}-\vec{y}|}dV(\vec{y})d\tau$$

(2.14)

2.3   LIGHTHILL'S ANALOGY

For a long period since Lighthill's ([1],1952) classical paper appeared, aeroacoustic computation has focused on solution of his acoustic analogy equation or variations thereof. In brief, Lighthill devised an arrangement of the continuity and momentum equations of fluid mechanics where all terms not appearing in the linear-wave operator are grouped into a double divergence of a source-like term now known as the Lighthill stress tensor. The result of the aforementioned manipulations is an equation featuring the wave operator (operating on the density perturbation) on the left-hand side and with all nonlinear effects accounted for by the Lighthill stress tensor:

$$\frac{\partial^2 \rho}{\partial t^2} - c_o^2 \frac{\partial^2 \rho}{\partial x_i^2} = \frac{\partial^2 T_{ij}}{\partial x_i \partial x_j}$$

35

where

$$T_{ij} = \rho u_i u_j - \tau_{ij} + (p - c_0{}^2 \rho)\delta_{ij}$$

(2.16)

This equation is obtained by subtracting to the time derivative of the continuity

equation the divergence of the momentum equation and the term $c_o{}^2 \dfrac{\partial^2 \rho}{\partial x_i{}^2}$.

Assuming the right hand side of equation 2.15 is known and independent from the

left hand side of the previous equation, it's possible to apply the methodology shown in

the previous section, which leads to

$$\rho(\vec{x},t) - \rho_o = \frac{1}{4\pi c_o{}^2} \int_\infty \frac{1}{r} \frac{\partial^2 T_{ij}}{\partial y_i \partial y_j} dV(\vec{y}) = \frac{1}{4\pi c_o{}^2} \frac{\partial^2}{\partial y_i \partial y_j} \int_\infty \frac{T_{ij}}{r} dV(\vec{y})$$

(2.17)

The square brackets indicate evaluation of the integrand at the retarded time,

$\tau = t - \dfrac{r}{c_o}$ and r is the distance between the source and the observer. It represents the time

at which the source emits the sound wave that will arrive to the observer location at time

t. This equation shows that the sound generated by turbulence is equivalent to the sound

generated in a steady fluid with a tensions distribution described by the Lighthill's tensor.

2.4   CURLE'S EQUATION

The Lighthill's theory sometimes can't be immediately applied since it doesn't

consider the presence of solid boundaries in the fluid domain. Curle extended the

Lighthill's theory in order to consider these effects, [3]. The general integral of the non homogeneous wave equation in a limited domain is

$$\rho(\vec{x},t) - \rho_o = \frac{1}{4\pi c_o^2} \int_\infty \frac{1}{r} \frac{\partial^2 T_{ij}}{\partial y_i \partial y_j} dV(\vec{y}) - \frac{1}{4\pi} \int_S \left(\frac{1}{r} \frac{\partial \rho}{\partial n} + \frac{1}{r^2} \frac{\partial r}{\partial n} \rho + \frac{1}{rc_o} \frac{\partial r}{\partial n} \frac{\partial \rho}{\partial \tau} \right) dS(\vec{y})$$

(2.18)

where n is the unit versor orthogonal to the surface, pointing to the fluid domain. Starting from this solution, Curle obtains a formulation analogous to Lighthill's, with the addition of an integration on an integration on the surface immersed in the fluid domain. To obtain this formulation the integrals of the previous equation have been rearranged. For the volume integration we have:

$$\frac{1}{4\pi c_o^2} \int_\infty \frac{1}{r} \frac{\partial^2 T_{ij}}{\partial y_i \partial y_j} dV(\vec{y}) = \int_\infty \int_V \frac{\partial^2 T_{ij}}{\partial y_i \partial y_j} (\vec{y},\tau) G(\vec{x}-\vec{y},t-\tau) dV(\vec{y}) d\tau$$

(2.19)

Since the argument of the Green function is $\vec{x}-\vec{y}$ it is possible to say that

$\dfrac{\partial G}{\partial y_i} = -\dfrac{\partial G}{\partial x_i}$. Using the divergence theorem we have:

$$\frac{1}{4\pi c_o^2} \int_\infty \frac{1}{r} \frac{\partial^2 T_{ij}}{\partial y_i \partial y_j} dV(\vec{y}) = \int_\infty \int_V \frac{\partial}{\partial y_i} \left(\frac{\partial T_{ij}}{\partial y_i} (\vec{y},\tau) G(\vec{x}-\vec{y},t-\tau) \right) dV(\vec{y}) d\tau +$$

$$- \int_\infty \int_V \frac{\partial T_{ij}}{\partial y_i} (\vec{y},\tau) \frac{\partial}{\partial y_i} G(\vec{x}-\vec{y},t-\tau) dV(\vec{y}) d\tau = - \int_\infty \int_S n_i \frac{\partial T_{ij}}{\partial y_i} (\vec{y},\tau) G(\vec{x}-\vec{y},t-\tau) dS(\vec{y}) d\tau +$$

$$+ \int_\infty \int_V \frac{\partial T_{ij}}{\partial y_i} (\vec{y},\tau) \frac{\partial}{\partial x_i} G(\vec{x}-\vec{y},t-\tau) dV(\vec{y}) d\tau$$

(2.20)

37

Since the dependent variables are τ and $\vec{y}$, $\dfrac{\partial}{\partial x_i}$ can be carried out from the

integral. The same work for the y_i leads to

$$\frac{1}{4\pi c_o^2}\int_{\infty}\frac{1}{r}\frac{\partial^2 T_{ij}}{\partial y_i \partial y_j}dV(\vec{y}) = -\int_{\infty}\int_{S} n_i \frac{\partial T_{ij}}{\partial y_i}(\vec{y},\tau)G(\vec{x}-\vec{y},t-\tau)dS(\vec{y})d\tau +$$

$$+\frac{\partial}{\partial x_i}\int_{\infty}\int_{V}\frac{\partial}{\partial y_i}\Big(T_{ij}(\vec{y},\tau)G(\vec{x}-\vec{y},t-\tau)\Big)dV(\vec{y})d\tau - \frac{\partial}{\partial x_i}\int_{\infty}\int_{V}T_{ij}(\vec{y},\tau)\frac{\partial}{\partial y_i}G(\vec{x}-\vec{y},t-\tau)dV(\vec{y})d\tau =$$

$$= -\int_{\infty}\int_{S}n_i\frac{\partial T_{ij}}{\partial y_i}(\vec{y},\tau)G(\vec{x}-\vec{y},t-\tau)dS(\vec{y})d\tau + \frac{\partial}{\partial x_i}\int_{\infty}\int_{S}n_j T_{ij}(\vec{y},\tau)G(\vec{x}-\vec{y},t-\tau)dS(\vec{y})d\tau +$$

$$-\frac{\partial^2}{\partial x_i \partial x_j}\int_{\infty}\int_{V}T_{ij}(\vec{y},\tau)G(\vec{x}-\vec{y},t-\tau)dV(\vec{y})d\tau$$

(2.21)

making an integration over the delta Dirac functions, it leads to

$$\frac{1}{4\pi c_o^2}\int_{\infty}\frac{1}{r}\frac{\partial^2 T_{ij}}{\partial y_i \partial y_j}dV(\vec{y}) = \frac{1}{4\pi c_o^2}\frac{\partial^2}{\partial x_i \partial x_j}\int_{\infty}\frac{T_{ij}(\vec{y},\tau)}{r}dV(\vec{y}) - \frac{1}{4\pi c_o^2}\frac{\partial}{\partial x_i}\int_{S}n_j\frac{T_{ij}(\vec{y},\tau)}{r}dS(\vec{y}) +$$

$$-\frac{1}{4\pi c_o^2}\int_{S}\frac{n_i}{r}\frac{\partial T_{ij}(\vec{y},\tau)}{\partial y_i}dS(\vec{y})$$

(2.22)

where τ represents the retarded time. The last steps of Curle's formulation are the

rearrangements of the surface integrals making use of the following relationships,

$$\frac{\partial}{\partial n} = n_i \frac{\partial}{\partial y_i} \qquad\qquad \frac{\partial}{\partial x_i}\left[\frac{f(\tau)}{r}\right] = -\left[\frac{f}{r^2}+\frac{1}{c_o r}\frac{\partial}{\partial \tau}\right]\frac{\partial r}{\partial x_i}$$

(2.23)

Hence the surface integral becomes,

$$\int_S \left(\frac{1}{r} \frac{\partial \rho}{\partial n} + \frac{1}{r^2} \frac{\partial r}{\partial n} \rho + \frac{1}{rc_o} \frac{\partial r}{\partial n} \frac{\partial \rho}{\partial \tau} \right) dS(\vec{y}) = \int_S n_i \left(\frac{1}{r} \frac{\partial \rho}{\partial y_i} + \frac{1}{r^2} \frac{\partial r}{\partial y_i} \rho + \frac{1}{rc_o} \frac{\partial r}{\partial y_i} \frac{\partial \rho}{\partial \tau} \right) dS(\vec{y}) =$$

$$= \int_S n_i \left(\frac{1}{r} \frac{\partial (\rho \delta_{ij})}{\partial y_i} - \frac{1}{r^2} \frac{\partial r}{\partial y_i} \rho + \frac{1}{rc_o} \frac{\partial r}{\partial y_i} \frac{\partial \rho}{\partial \tau} \right) dS(\vec{y}) = \int_S \frac{n_i}{r} \frac{\partial (\rho \delta_{ij})}{\partial y_i} dS(\vec{y}) + \frac{\partial}{\partial x_i} \int_S \frac{n_i}{r} \rho \delta_{ij} dS(\vec{y})$$

<div align="right">(2.24)</div>

which leads to

$$\rho(\vec{x},t) - \rho_o = \frac{1}{4\pi c_o^2} \frac{\partial^2}{\partial x_i \partial x_j} \int_\infty \frac{T_{ij}}{r} dV(\vec{y}) - \frac{1}{4\pi c_o^2} \frac{\partial}{\partial x_i} \int_S \frac{n_j}{r} \left(T_{ij} + c_o^2 \rho \delta_{ij} \right) dS(\vec{y}) +$$

$$- \frac{1}{4\pi c_o^2} \int_S \frac{n_i}{r} \frac{\partial}{\partial y_i} \left(T_{ij} + c_o^2 \rho \delta_{ij} \right) dS(\vec{y})$$

<div align="right">(2.25)</div>

From the definition of the Lighthill tensor and from the momentum equation it is possible to obtain

$$\frac{n_i}{r} \frac{\partial}{\partial y_i} \left(T_{ij} + c_o^2 \rho \delta_{ij} \right) = -\frac{n_i}{r} \frac{\partial \rho u_i}{\partial t}$$

<div align="right">(2.26)</div>

leading to

$$\rho(\vec{x},t) - \rho_o = \frac{1}{4\pi c_o^2} \frac{\partial^2}{\partial x_i \partial x_j} \int_\infty \frac{T_{ij}}{r} dV(\vec{y}) - \frac{1}{4\pi c_o^2} \frac{\partial}{\partial x_i} \int_S \frac{n_j}{r} \left(\rho u_i u_j + p \delta_{ij} - \tau_{ij} \right) dS(\vec{y}) +$$

$$+ \frac{1}{4\pi c_o^2} \int_S \frac{\rho u_i n_i}{r} dS(\vec{y})$$

<div align="right">(2.27)</div>

For solid surfaces the velocity on the surface vanishes, hence the final result of Curle's equation is:

$$\rho(\vec{x},t) - \rho_o = \frac{1}{4\pi c_o^2} \frac{\partial^2}{\partial x_i \partial x_j} \int_\infty \frac{T_{ij}}{r} dV(\vec{y}) - \frac{1}{4\pi c_o^2} \frac{\partial}{\partial x_i} \int_S \frac{n_j}{r} \left(p\delta_{ij} - \tau_{ij} \right) dS(\vec{y})$$

(2.28)

2.5   THE FFOWCS WILLIAMS & HAWKINGS'S ANALOGY

A generalization of Lighthill's theory to include aerodynamic surfaces in motion, proposed by Ffowcs Williams & Hawkings ([6], 1969) has provided the basis for a significant amount of analysis of the noise produced by rotating blades, including helicopter rotors, propeller blades, and fans,

The Ffowcs Williams & Hawkings (FW-H) theory includes surface source terms in addition to the quadrupole-like source introduced by Lighthill. The surface sources are generally referred to as thickness (or monopole) sources and loading (or dipole) sources.

They are also often termed linear in that no explicitly nonlinear terms appear in them and the propagation from the surfaces has no nonlinear component. It should be noted, however, that the loading sources, which consist of surface pressures, may be computed using nonlinear aerodynamic methods.

The following work is the same reported by Crighton [4].

Let us consider a surface S immersed in a fluid, which moves at a speed equal to v_i and defined by the function $f(\vec{x},t)$:

$$\begin{cases} f(\vec{x},t) < 0, & inside\ S \\ f(\vec{x},t) = 0 & on\ S \\ f(\vec{x},t) > 0 & outside\ S \end{cases}$$

$$(2.29)$$

Typically S is the surface of the body. However it is not strictly necessary since the theory developed in this section is not only true for surfaces that limit the body but also for surfaces that simply contain the body.

The $f(\vec{x},t)$ function satisfies the following,

$$\frac{\partial f}{\partial t} + v_i \frac{\partial f}{\partial x_i} = 0$$

$$(2.30)$$

since the density at an infinite distance from the body is constant, it's possible to obtain

$$\frac{\partial(\rho - \rho_o)}{\partial t} + \frac{\partial \rho u_i}{\partial x_i} = 0$$

$$(2.31)$$

Multiplying the continuity equation by the Heaviside function:

$$\frac{\partial(\rho - \rho_o)}{\partial t} H(f) + \frac{\partial \rho u_i}{\partial x_i} H(f) = 0$$

$$(2.32)$$

or equivalently

$$\frac{\partial(\rho - \rho_o)H(f)}{\partial t} + \frac{\partial \rho u_i H(f)}{\partial x_i} = \frac{\partial H(f)}{\partial t}(\rho - \rho_o) + \frac{\partial H(f)}{\partial x_i} \rho u_i$$

$$(2.33)$$

Remembering the proprieties of the Heaviside function:

$$\frac{\partial(\rho - \rho_o)H(f)}{\partial t} + \frac{\partial \rho u_i H(f)}{\partial x_i} = \left[\frac{\partial f}{\partial t}(\rho - \rho_o) + \frac{\partial f}{\partial x_i}\rho u_i\right]\delta(f) =$$

$$= \left[\rho_o v_i + \rho(u_i - v_i)\right]\frac{\partial f}{\partial x_i}\delta(f) = Q|\nabla f|\delta(f)$$

(2.34)

where it has been considered that $\frac{\partial f}{\partial x_i} = n_i|\nabla f|$, while for Q it has been considered

that

$$Q = \left[\rho_o v_i + \rho(u_i - v_i)\right]n_i$$

(2.35)

and it has to be considered like a source term which exist only on the surface S.

It's possible to rearrange the momentum equation in the same way, leading to

$$\frac{\partial \rho u_i H(f)}{\partial t} + \frac{\partial \rho u_i u_j H(f)}{\partial x_j} + \frac{\partial p H(f)}{\partial x_i} - \frac{\partial \tau_{ij} H(f)}{\partial x_i} = \rho u_i \frac{\partial H(f)}{\partial t} + \rho u_i u_j \frac{\partial H(f)}{\partial x_j} +$$

$$+ p\frac{\partial H(f)}{\partial x_i} - \tau_{ij}\frac{\partial H(f)}{\partial x_i} = \left[\rho u_i \frac{\partial f}{\partial t} + \rho u_i u_j \frac{\partial f}{\partial x_j} + p\delta_{ij}\frac{\partial f}{\partial x_j} - \tau_{ij}\frac{\partial f}{\partial x_j}\right]\delta(f) =$$

$$= \left[\rho u_i(u_i - v_i)\frac{\partial f}{\partial x_j} + p\delta_{ij}\frac{\partial f}{\partial x_j} - \tau_{ij}\frac{\partial f}{\partial x_j}\right]\delta(f) = F_i|\nabla f|\delta(f)$$

(2.36)

where

$$F_i = \left[\rho u_i(u_j - v_j) + p\delta_{ij} - \tau_{ij}\right]n_i$$

(2.37)

42

$$\left[\frac{\partial^2}{\partial t^2} - c_o{}^2\frac{\partial^2}{\partial x_i{}^2}\right](\rho - \rho_o)H(f) = \frac{\partial^2 T'_{ij}H(f)}{\partial x_i\partial x_j} - \frac{\partial F_i|\nabla f|\delta(f)}{\partial x_i} + \frac{\partial Q|\nabla f|\delta(f)}{\partial t}$$

(2.38)

where

$$T'_{ij} = \rho u_i u_j - \tau_{ij} + \left(p - c_o{}^2(\rho - \rho_o)\right)\delta_{ij}$$

(2.39)

looks similar to Lighthill's tensor and ρ_o does not affect the sound generation, since it is a constant.

The solution of this wave equation is given by

$$\rho(\vec{x},t) - \rho_o = \frac{\partial^2}{\partial x_i\partial x_j}\iint_\infty[T_{ij}H(f)](\vec{y},\tau)\frac{\delta(r - c_o(t-\tau))}{4\pi c_o r}dV(\vec{y})d\tau +$$

$$-\frac{\partial}{\partial x_i}\iint_\infty[F_i|\nabla f|\delta(f)](\vec{y},\tau)\frac{\delta(r - c_o(t-\tau))}{4\pi c_o r}dV(\vec{y})d\tau +$$

$$+\frac{\partial}{\partial t}\iint_\infty[Q|\nabla f|\delta(f)](\vec{y},\tau)\frac{\delta(r - c_o(t-\tau))}{4\pi c_o r}dV(\vec{y})d\tau$$

(2.40)

In the case of a moving surface, the $f(\vec{x},t)$ function and the sources terms are better expressed in a surface reference system. If we refer to the new reference system with $\vec{y}^*$, it follows that:

$$y_i = y_i{}^* + v_i\tau$$
$$u_i = u_i{}^* + v_i\tau$$

(2.41)

The Jacobean of this transformation is equal to unit. Since $\vec{y}$ and r are now both functions of τ, we have to consider the following variable substitution to integrate on τ:

43

$$g(\tau) = r - c_o(t - \tau)\tau$$

$$dg = (\partial r / \partial \tau + c_0)d\tau$$

(2.42)

where

$$\frac{\partial r}{\partial \tau} = \frac{\partial r}{\partial y_i}\frac{\partial y_i}{\partial \tau} = \frac{-2(x_i - y_i)}{2\sqrt{(x_i - y_i)^2}}\frac{\partial y_i}{\partial \tau} = -\frac{x_i - y_i}{r}v_j = -l_j v_j$$

(2.43)

Where l_j is the j-component of a unit versor pointing from the source to the observer location. Hence we have,

$$dg = (c_o - l_j v_j)d\tau$$

(2.44)

Applying the variable substitution to the previous solution it yields:

$$\rho(\vec{x},t) - \rho_o = \frac{\partial^2}{\partial x_i \partial x_j}\iint_\infty \left[T'_{ij}{}^* H(f^*)\right](\vec{y}^*,\tau)\frac{\delta(g)}{4\pi c_o r(c_o - l_j v_j)}dV(\vec{y}^*)d\tau +$$

$$-\frac{\partial}{\partial x_i}\iint_\infty \left[F_i^* \left|\nabla f^*\right|\delta(f^*)\right](\vec{y}^*,\tau)\frac{\delta(g)}{4\pi c_o r(c_o - l_j v_j)}dV(\vec{y}^*)d\tau +$$

$$+\frac{\partial}{\partial t}\iint_\infty \left[Q^* \left|\nabla f^*\right|\delta(f^*)\right](\vec{y}^*,\tau)\frac{\delta(g)}{4\pi c_o r(c_o - l_j v_j)}dV(\vec{y}^*)d\tau$$

(2.45)

Where the source terms in the new reference system are

$$Q^* = \left[\rho_o v_i + \rho u_i{}^*\right]n_i$$

(2.46)

$$F_i^* = \left[\rho u_j{}^*\left(u_i{}^* + v_i\right) + p\delta_{ij} - \tau_{ij}{}^*\right]n_i$$

(2.47)

44

$$T_{ij}^{'\ *} = \rho(u_i^{\ *} + v_i)(u_j^{\ *} + v_j) - \tau_{ij}^{\ *} + \left(p - c_o^{\ 2}(\rho - \rho_o)\right)\delta_{ij}$$

(2.48)

It has to be noticed that $\tau_{ij}^{\ *} = \tau_{ij}$. Integrating on dg,

$$\rho(\vec{x},t) - \rho_o = \frac{1}{4\pi c_o^{\ 2}} \frac{\partial^2}{\partial x_i \partial x_j} \iint_\infty \frac{\left[T_{ij}^{'\ *} H(f^*)\right]}{r(1 - l_j v_j / c_o)} dV(\vec{y}^*) d\tau +$$

$$-\frac{1}{4\pi c_o^{\ 2}} \frac{\partial}{\partial x_i} \iint_\infty \frac{\left[F_i^{\ *} |\nabla f^*| \delta(f^*)\right]}{r(1 - l_j v_j / c_o)} dV(\vec{y}^*) d\tau + \frac{1}{4\pi c_o^{\ 2}} \frac{\partial}{\partial t} \iint_\infty \frac{\left[Q^* |\nabla f^*| \delta(f^*)\right]}{r(1 - l_j v_j / c_o)} dV(\vec{y}^*) d\tau$$

(2.49)

Where the integrand functions have to be evaluated at $g=0$ or at $\tau = t - r/c_o$.

Integrating on the δ-functions it is possible to obtain the final formulation of the wave equation

$$\rho(\vec{x},t) - \rho_o = \frac{1}{4\pi c_o^{\ 2}} \frac{\partial^2}{\partial x_i \partial x_j} \iint_\infty \frac{T_{ij}^{'\ *}}{r(1 - l_j v_j / c_o)} dV(\vec{y}^*) d\tau +$$

$$-\frac{1}{4\pi c_o^{\ 2}} \frac{\partial}{\partial x_i} \iint_\infty \frac{F_i^{\ *}}{r(1 - l_j v_j / c_o)} dS(\vec{y}^*) d\tau + \frac{1}{4\pi c_o^{\ 2}} \frac{\partial}{\partial t} \iint_\infty \frac{Q^*}{r(1 - l_j v_j / c_o)} dS(\vec{y}^*) d\tau$$

(2.50)

For a solid surface we have, $u_i^{\ *} = 0$, thus

$$Q^* = \left[\rho_o v_i\right] n_i$$

(2.51)

$$F_i^{\ *} = \left[p\delta_{ij} - \tau_{ij}^{\ *}\right] n_i$$

(2.52)

The $Q*$ term is equal to zero in the case of steady surface. In the case of a steady surface and S equal to the body surface the FW-H's equation reduces to the Curle equation.

2.6   CONSIDERATIONS ON THE SOUND GENERATED AERODYNAMICALLY

A first way to proceed is the direct calculation of the acoustic pressure through a direct simulation of the compressible fluid.

Typically this method is not widely used since it is too computationally expensive, requiring higher order numerical schemes to reduce the dissipation and the dispersion of the acoustic waves, and complicated boundary conditions. For example, non-reflecting boundary conditions (NRBCs) may be required to avoid unphysical reflections contaminating the computational domain. Other methods exist to avoid this phenomenon when NRBCs are not available, including the use of purposefully dissipative grid regions close to domain boundaries.

Alternatively to make an estimation of the aerodynamically generated sound, the acoustic analogy with a turbulence model simulation for computing the sources can be used. This last approach needs sophisticated turbulence models since the good resolution of the flow field is the primary requirement to obtain an accurate prediction of sound sources. Let us investigate the advantages and the weaknesses of the acoustic analogy. In obtaining Lighthill's equation, from a simple manipulation of the Navier-Stokes Equations, we have supposed that $c_o{}^2 \dfrac{\partial^2 \rho}{\partial x_i{}^2}$ was independent from the left hand side of

equation 2.15. This hypothesis is never satisfied since the Lighthill's tensor is dependent on the density itself. In other word the acoustic analogy leads to a good result if the turbulent flow field and the acoustics one are not coupled, that is when we can neglect the effect of acoustics on the flow. The acoustic analogies divide the generation of sound from the propagation, computing the latter by a wave operator.

Let us consider the Lighthill's tensor, 2.16,

$$T_{ij} = \rho u_i u_j - \tau_{ij} + (p - c_0^2 \rho)\delta_{ij}$$

(2.16)

The dominant term, if the flow is turbulent, is the fluctuating Reynolds tensor, hence it's possible to consider

$$T_{ij} \cong \rho u_i u_j$$

(2.54)

The Reynolds tensor represents a stress related to the particles exchanges in the fluid. Hence this tensor has an effect similar to the viscous stress. In the same way, from a generation of sound point of view, the fluctuating Reynolds tensor has an effect similar to the viscous stresses and is relatively more important than them.

The double divergence of the Reynolds fluctuating tensor, as noticed by Howe [5], can be rearranged for low-Mach number as

$$\frac{\partial^2 \rho_o u_i u_j}{\partial x_i \partial x_j} \cong div(\rho_o \vec{\omega} \wedge \vec{v})$$

(2.55)

This relationship shows that the vorticity is the main cause of the aerodynamic sound and the main acoustic sources are related to surfaces.

A better evaluation of the wall effect can be made analyzing the order of magnitude of the various terms of the FW-H equation

$$\rho(\vec{x},t) - \rho_o = \frac{1}{4\pi c_o^2} \frac{\partial^2}{\partial x_i \partial x_j} \iint_\infty \frac{T'^*_{ij}}{r\left(1 - l_j v_j / c_o\right)} dV(\vec{y}^*) d\tau +$$

$$-\frac{1}{4\pi c_o^2} \frac{\partial}{\partial x_i} \iint_\infty \frac{F_i^*}{r\left(1 - l_j v_j / c_o\right)} dS(\vec{y}^*) d\tau + \frac{1}{4\pi c_o^2} \frac{\partial}{\partial t} \iint_\infty \frac{Q^*}{r\left(1 - l_j v_j / c_o\right)} dS(\vec{y}^*) d\tau$$

(2.56)

If S corresponds to the body surface, the three terms of the right hand side of previous equation are related to different causes. The first term corresponds to the sound produced by turbulent structures and from dimensional analysis it results

$$p(\vec{x},t) \cong \frac{\rho D}{4\pi r c^2} U^4$$

(2.57)

and the sound intensity is

$$I(r) \cong \frac{p^2(\vec{x},t)}{\rho_o c_o} \cong \frac{\rho D^2}{16\pi^2 r^2 c^5} U^8$$

(2.58)

or equivalently

$$I(r) \cong U^3 M^5$$

(2.59)

known as the Lighthill's v^8-law

The second term represents the component due to the forces that act on the surface, for which the pressure fluctuations can be estimated as

$$p(\vec{x},t) \cong \frac{\rho D}{4\pi r c} U^3$$

(2.60)

and the sound intensity results in

$$I(r) \cong \frac{p^2(\vec{x},t)}{\rho_o c_o} \cong \frac{\rho D^2}{16\pi^2 r^2 c^3} U^6$$

(2.61)

or equivalently

$$I(r) \cong U^3 M^3$$

(2.62)

The third term is equal to zero if the surface S is attached to the body and this last one is not affected by vibration.

Comparing the first and the second term it is possible to say that the contribution of the surface sources (second term) is dominant.

Another approximation in an acoustic analogy is the use of a linear wave operator, in fact this one describes well the wave propagation only for low speed cases (M<0.4).

2.7 FLUENT IMPLEMENTATION OF ACOUSTIC ANALOGY

The commercial code FLUENT estimates the acoustic pressure through the use of the Ffowcs Williams and Hawkings Analogy, neglecting the terms related to the Lighthill's tensor as they are relatively unimportant compared to the other source terms.. The formulation used is the one of Farassat and Brentner:

$$4\pi(p(\vec{x},t)-p_o) = \frac{1}{c_0}\int_S\left[\frac{c_0\rho_0(\dot{U}_n+U_n)+\dot{L}_r}{r(1-M_r)^2}\right]dS$$

$$+\int_S\left[\frac{c_0U_n(r\dot{M}_r+c_0(M_r-M^2))+L_r-L_M}{r^2(1-M_r)^3}\right]dS$$

$$+\frac{1}{c_0}\int_S\left[\frac{L_r(r\dot{M}_r+a_0(M_r-M^2))+L_r-L_M}{r^2(1-M_r)^3}\right]dS$$

(2.63)

where

$$U_i = v_i + \frac{\rho}{\rho_0}(u_iv_i)$$

(2.64)

$$L_i = P_{ij}n_j + \rho u_i(u_n-v_n)$$

(2.65)

$$P_{ij} = p\delta_{ij} + \mu\left[\frac{\partial u_i}{\partial x_j}+\frac{\partial u_j}{\partial x_i}-\frac{2}{3}\frac{\partial u_k}{\partial x_k}\delta_{ij}\right] \quad ; \quad L_M = L_iM_i$$

(2.66)

and M_i is the Mach number estimated using the velocity in the i-direction .

This formulation is equivalent to the FW-H proposed in the section 2.5 with all the derivatives carried inside the integrals.

All the integrand functions have to be evaluated at the retarded time. The sources have to be evaluated in a time instant dependent on their position. This causes the complication to save the entire time history of the fluid-dynamic variables that constitute the acoustic sources. To clarify let us consider two different punctual sources located at a certain distance from observer and indicated by r_1 and r_2.

The acoustic pressure is given by a relationship

$$p(\vec{x},t) \cong f_1(\vec{y_1},\tau_1) + f_2(\vec{y_2},\tau_2)$$

(2.67)

Where f_1 and f_2 are generic function that depend on the acoustic analogy adopted. This equation can only be resolved if f_1 and f_2 are known at the times τ_1 and τ_2 coming before the time t.

Simulation	Surface S	Quantities stored	Simulation
Incompressible	Wall	p	Incompressible
Incompressible	Porous surface	p, u, v, w	Incompressible
Compressible	Wall	P	Compressible
Compressible	Porous surface	p, ρ, u, v, w	Compressible

In the case of steady surfaces:

$$4\pi(p(\vec{x},t) - p_o) = \frac{1}{c_0} \int_S \left(\frac{c_0 \rho_0 \dot{U}_n + \dot{L}_r}{r} \right) dS + \int_S \frac{L_r}{r^2} dS$$

(2.68)

In the case of non-permeable surfaces:

$$4\pi(p(\vec{x},t) - p_o) = \int_S \left(\frac{\dot{L}_r}{c_0 r} + \frac{L_r}{r^2} \right) dS =$$

$$\int_S \left(\frac{\dot{p}\delta_{ij} - \dot{\tau}_{ij}}{c_0 r} + \frac{p\delta_{ij} - \tau_{ij}}{r^2} \right) dS$$

(2.69)

the contributions related to the viscous stresses are negligible compared to that due to pressure source. The pressure fluctuation is finally calculated by

$$p(\vec{x},t) - p_o \cong \frac{1}{4\pi} \sum_{f=1}^{N_f} \left[\frac{\dot{p}\delta_{ij}}{c_0 r} + \frac{p\delta_{ij}}{r^2} \right]_{f,\tau} A_f$$

(2.70)

3 AEROACOUSTICS SIMULATION APPROACHES

As we have seen in the previous Chapters, Aeroacoustics is a subtopic of acoustics pertaining to situations where sound is generated by fluid flow.

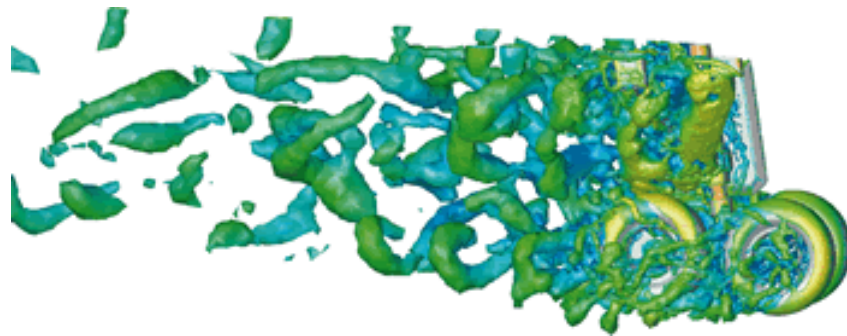In contrast, Vibro-Acoustics is the field pertaining to sound caused by vibrating objects such as the diaphragm of a speaker.

Figure 3-1 Pressure fluctuations on an aircraft landing gear.

There are four primary entities in any aeroacoustics problem: the acoustic medium, sources (flow), sound, and receivers [48]. The acoustic medium in most problems is the air and sound sources are the flow structures that induce pressure fluctuations in air.

The sources can be in the form of any unsteady flow structure such as vortices, shear-layers, or turbulent eddies. Sounds are pressure waves travelling through the

acoustic medium and the receiver is the observer of these sound waves, which can be a microphone or the human ear in practice.

Computational Fluid Dynamics (CFD) is an essential part of aeroacoustics simulations since it is the only viable way to simulate all varieties of source flow structures such as vortices, shear-layers, turbulent eddies, and others. There are four primary ways to model sound generation and transmission with a general purpose CFD solver. In decreasing order of accuracy, extent of applicability, and computational effort they are:

· Computational Aeroacoustics (CAA)

· Coupling of CFD and wave-equation-solver

· Using integral acoustic models

· Acoustics source strength estimation from local turbulence scales

3.1 COMPUTATIONAL AEROACOUSTICS

Computational Aeroacoustics (CAA) is the most comprehensive way to simulate aeroacoustics. It does not rely on any model and therefore in aeroacoustics its position is analogous to that of Direct Numerical Simulation (DNS) in the field of turbulent flow simulation. CAA essentially is a general transient simulation of the entire fluid region encompassing the sources, receivers, and the entire sound transmission path in between. The simulation computes pressure disturbances created in the source regions by rigorously calculating the time-varying flow structure in these regions. It also simulates sound transmission by actually resolving the pressure waves travelling in the fluid. Finally at the receiver location it records the time-varying static pressure. This is the

sound signal heard by the receiver. As can be imagined, such a simulation needs to incorporate a range of physical phenomena.

It is essential to properly capture turbulence in the source region in order to predict source pressure fluctuations accurately. Likewise, fluid compressibility needs to be incorporated in the simulation for properly simulating the transmission of sound (pressure) waves. The most general equations that govern all these physical phenomena in a fluid region are the Navier-Stokes equations. A CAA simulation therefore involves obtaining a complete transient solution of the Navier-Stokes equations on a fluid domain encompassing the sound sources, receivers, and the transmission path in between.

Though CAA is the most general and accurate theoretical approach for simulating aeroacoustics, it is unrealistic for most engineering problems due to a number of practical limitations, as range of scales and range of pressure.

3.1.1   Range of Scales

A CAA simulation needs to resolve a wide range of both time and length scales.

Sound frequencies audible to the human ear span from 20 Hz to 20,000 Hz. To properly simulate the highest frequency, it is necessary to use a time-step (sampling duration) nearly 10-20 times smaller than the time period of that frequency. Likewise, for accurately capturing the lowest frequency, at least 10 time periods of that frequency need to be simulated. Thus the real time to be simulated is more than 100,000 times greater than the time-step size, necessitating many time-steps. Similarly, the simulation needs to be carried out at a very fine spatial resolution to capture both the generation and transmission of high frequency sound. The source of high pitch sound often are tiny micron sized turbulent eddies. Also the wavelength of high frequency sound waves is of

the order of a few cm. Yet the computational domain has to span large distances to encompass the sources and receivers. For instance, for sound produced by an aircraft jet, the distance between the source (jet) and the receiver (an observer standing on the ground) is many kilometres. In effect to resolve such a wide range of length and time scales a CAA simulation needs a massive number of computational cells, a very short time-step and to model for a relatively long time period. Such computational expense is unrealistic for most practical applications with current state-of-the-art computing resources.

3.1.2   Range of Pressures

Another complication in CAA simulations is the wide range of pressures involved. Typically, pressure fluctuations are in the range of a few to a few hundred kPa in a transient flow such as that in the wake of a cylinder. On the other hand, sound pressure is of the order of milli-Pascals. As seen in Figure 3.2, sound pressure corresponding to a 60 dB sound pressure level (SPL) is 20 mPa. A CAA simulation therefore needs to keep track of pressures that differ by a factor of 10^6 or more. Thus the accuracy of the simulation becomes highly sensitive to truncation error. Even second order discretization schemes typically used for flow computations rapidly deteriorate the tiny sound pressure component in the overall pressure.
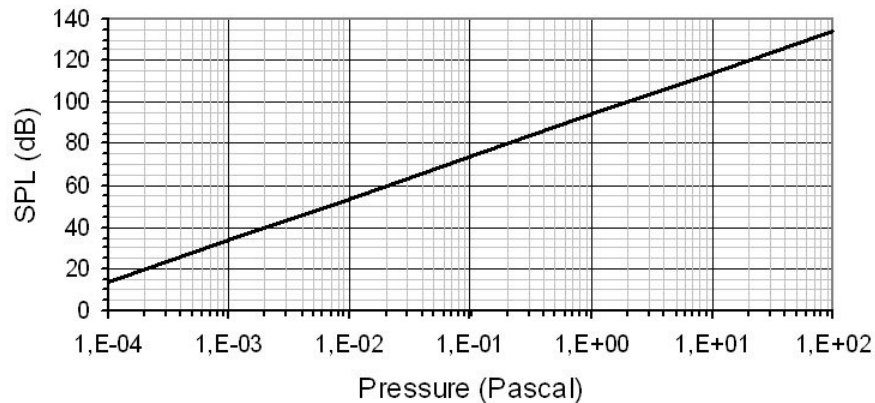
Figure 3-2 Relation between sound pressure (Pa) and sound pressure level (dB).

Computationally expensive higher order schemes are essential to accurately transport the sound signal through the computational domain. However, even 6th or 7th order schemes are unable to accurately transport small sound signals over large distances encountered in many practical problems.

3.2 CFD-WAVE-EQUATION-SOLVER COUPLING

Computational Aeroacoustics (CAA) is prohibitively expensive for most practical problems due to the large difference in time, length, and pressure scales involved in sound generation and transmission. However, this large difference in scales provides a good opportunity of greatly simplifying the simulation by splitting the problem into two parts and modeling them separately. Sound generation involves small length scales and tiny pressure scales. Since the scales involved in these two phenomena differ so significantly, the two can be treated separately. The Navier-Stokes equations govern the first part while the latter is governed by the wave equation.

57

Splitting the problem into two parts thus is advantageous in several ways. First, the expensive high-resolution, transient solution of Navier-Stokes equations can be restricted only to a small area close to the source regions. Secondly, the computational grid can be optimized to suit flow simulation requirements close to the source region, and to meet the transmission simulation requirements in the transmission region.

Further, this approach allows easier use of analytical models for the source as well as the transmission part, e.g. the analytical model proposed by Ffowcs-Williams and Hawkings can be used for the transmission.

However, splitting the problem into two parts this way has inherent limitations. First, the approach is valid only when the scales involved in sound generation and transmission are distinctly different. Secondly, this approach cannot effectively handle the backward effect of sound on the flow field. For example, Ffowcs-Williams and Hawkings approach cannot be used to simulate whistles in automotive air intake manifolds since a whistle is caused by resonance between a shear-layer fluctuating in the mouth of a cavity and the sound waves reflecting off the cavity bottom.

Solving the wave equation using the Boundary Element Method can take into account reflection and scattering. Generally it can be used in closed domain too or when obstacles or reflective surfaces are present in the propagation region, but it can not still handle the backward effect of sound on the flow field. For example, a CFD simulation can be used to calculate the time varying pressure signals at a multitude of points on the acoustics source surfaces as dipole boundary conditions, which will be used by the BEM solver performing the computation of the radiated acoustic field in the region of interest.

3.3   INTEGRAL ACOUSTICS METHODS

The approach of splitting the flow and sound fields from each other and solving them separately can be simplified further if the receiver is in straight, unobstructed view from every individual point of the source region. Sound transmission from a source point to the receiver can be computed by simple analytical formulation. By integration of such sound transmission over all points on the source surface, the complete sound signal at the receiver can be obtained. As we saw in the previous Chapter, the Lighthill Acoustic Analogy provides the mathematical foundation for such an integral approach. The Ffowcs-Williams and Hawkings (FW-H) method extends the analogy to cases were solid, permeable, or rotating surfaces are sound sources, and is the most complete formulation of the acoustic analogy to date.

To compute sound with the FW-H method, one needs to perform a well-resolved transient CFD simulation only in the source region. Flow quantities, such as pressure and velocity are stored as functions of time on every point of every source surface during the simulation. At the end, this source data is in the FW-H integral to compute sound at the receiver. Since the FW-H is quite general and allows arbitrarily moving source surfaces, it can also be applied to predicting noise radiating from fans.

3.4   SYNTHETIC NOISE GENERATION METHOD

All the three methods described so far require well-resolved transient CFD simulations since they aim at determining the actual time-varying sound pressure signal at the receiver and from that the sound spectrum. In several practical engineering

situations one needs to determine locations and relative strengths of sound sources rather than such spectra at the receivers. If the sound is broadband, i.e. without any prominent tones characterized by sharp peaks in spectrum, then source strengths can be evaluated with reasonable accuracy from the time-averaged structure of the turbulent flow in the source regions.

Figure 3-3 Iso-surface of Lilley's acoustic source (total) strength around a generic sedan [48].

Turbulence is the primary cause of sound in aeroacoustics, therefore, in a broad sense, regions of the flow field where turbulence is strong are louder sources of sound. To-date there are a number of analytical models which synthesize sound at points in the flow field from local flow and turbulence quantities to estimate local sound source strengths. These are collectively referred to as broad-band noise source models and are based on an approach referred to as the synthetic noise generation method. The key advantage of these models is that they require very modest computational resources compared to the methods described in the previous sections. Broadband noise models only need a steady state flow solution whereas the other methods essentially require well-resolved transient flow solutions.

4   NOISE GENERATION MECHANISM

In the following section we will discuss in detail the mechanism of noise generation for some typical problems of strong engineering interest. A good understanding of the physics involved in sound generation is crucial when choosing the models and methodologies to simulate it. This will also help in interpreting the results obtained from a simulation and to figure out the limitations of the information we can get.

4.1   CAVITY NOISE

A typical example of Aeroacoustics is cavity noise. Air flowing past a cavity produces a distinct sound. There are no moving parts in this case. The flow itself is the source of sound. A shear layer establishes in the mouth of the cavity and oscillates at a particular frequency causing pressure fluctuations to propagate away from the cavity mouth that manifest as sound.

The flow over a cavity is characterized by a complex feedback process that can lead to large-amplitude, self-sustained oscillations of the pressure, velocity, and density fields in and around the cavity. The feedback process involves the growth and convection of instability waves in the shear layer spanning the cavity, the generation of a large-amplitude acoustic source associated with shear-layer impingement on the cavity trailing edge, feedback of an acoustic disturbance to the separation edge, and conversion of the

feedback disturbance to shear-layer instability waves through a receptivity process, Figure 4-1.
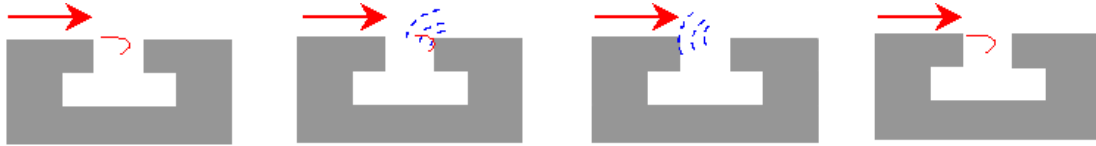
Figure 4-1 Triggering of vortex shedding.

Hence the process involves a time-dependent, quasi-periodic vortex shedding that can interact with the acoustic resonance of the cavity which acts as a Helmholtz resonator. When the frequency of the flow fluctuations is far from that of acoustic resonance, the two phenomena are weakly coupled and can be treated independently. However, when these two frequencies are close an intense energy exchange between the driving flow oscillations and fluid inside the cavity can occur.

These strong oscillations are undesirable in many engineering applications as they can induce structural vibration and fatigue, noise radiation, and drag on bodies possessing the cavity. Cavity flows are pertinent to a wide range of real-world applications, ranging from landing gear and weapons bays in aircraft to flow over ground vehicles. The importance of cavity flows in these engineering applications is evidenced by the large number of review articles on the subject.

The whole phenomena can be simplified by the following mechanical analogy of a mass-spring-damped oscillator, Figure 4-2. The driving force in our case can be the vortex shedding over the opening of the cavity, the mass M is the mass of the air in the neck, the spring constant K corresponds to the elasticity of the air contained in the cavity,

the resistance R is related to the viscous and radiation losses through the neck of the cavity and to the absorption and compliance of the walls.
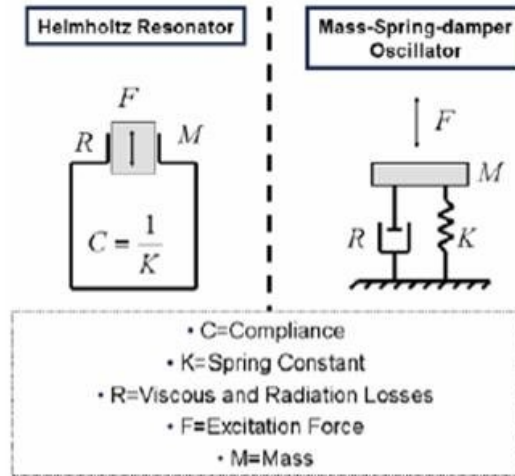
Figure 4-2 Mechanical analogy of acoustic resonant cavity.
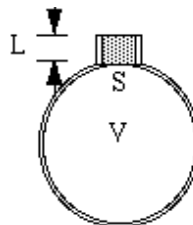
Figure 4-3 Acoustic cavity.

If we assume that the volume of the cavity is V, the length of the neck is L, the speed of sound to be c, and S is the cross section area of the neck of the cavity as shown in Figure 4-3, the frequency of the Helmholtz resonator can be shown to be:

$$f_H = \frac{c}{2\pi} \sqrt{\frac{S}{VL}}$$

<div align="right">(4.1)</div>

A classic example of the use of CAA is the cavity noise that can be generated in the cabin of a car, sometimes called aerodynamic buffeting. Buffeting is a wind noise of high intensity and low frequency heard in a moving vehicle when a window or sunroof is open. There are two sources of this sound (1) the transient vortex shedding in the wake of the side view mirror and (2) a shear-layer flapping in the window or sun-roof opening. Both sources contribute to side window buffeting while only the latter acts as a source of sun-roof buffeting. Pressure fluctuations induced by these flow structures propagate in the vehicle cabin and are heard by the driver and passengers. Consequently, the sources and receivers are located fairly close to each other.

Two other characteristics of buffeting allow it to be modelled with CAA. First, buffeting sound frequency is very low, in the range of 15 to 25 Hz. As a result the CAA simulation can be conducted with a relative few number of large time-steps without exorbitant computational expense. Secondly, buffeting sound pressure levels are very high, often over 100 dB. Thus, the sound pressure fluctuation is fairly large (2 Pa as per Figure 3-2) and can be captured accurately without undue truncation errors with usual second order discretization schemes.

Similar considerations can be used for the cavity noise that is generated in the door gap of any ground vehicle at moderate speed, although the frequency of the noise produced can be up to thousands of hertz as it depends on the velocity of the shed vortices (proportional to the free stream velocity) and on the characteristic dimension of

65

the cavity. The higher frequencies involved make the CAA simulation more difficult, but it will be shown that is still affordable with a moderate computational effort.

4.2   VORTEX SHEDDING NOISE

For describing this type of noise we can refer, to the noise generated by a cylinder in a flow field, which is representative of several bluff body flows found in engineering applications (e.g., automobile antenna noise, aircraft landing gear noise, etc.). As it was said in the Chapter 3, it was shown ("The influence of solid boundaries on aerodynamic sound", Curle, 1955, Proc. Roy. Soc. London A 231, 505.) that the sound generated by turbulent flow in the region of a solid body is exactly analogous to the sound radiated by a "free space" distribution of quadrupole sources plus a surface distribution of dipoles. When the Mach number is low the main contribution to noise is the dipole surface distribution.

Let's first introduce the Kármán vortex street. A Kármán vortex street is a repeating pattern of swirling vortices caused by the unsteady separation of flow over bluff bodies. They are named after the engineer and fluid-dynamicist, Theodore von Kármán.

A vortex street will only be observed over a given range of Reynolds numbers *Re*, typically above a limiting *Re* value of about 70. The range of *Re* values will vary with the size and shape of the body from which the eddies are being shed, as well as with the kinematic viscosity of the fluid. The governing parameter, the Reynolds number, is essentially a measure of the ratio of inertial to viscous forces in the flow and is defined as

$$Re = \frac{Vd}{\nu}$$

(4.2)

where:

- d = diameter of the cylinder (or some other suitable measure of width of non-circular bodies)

- V = steady velocity of the flow upstream of the cylinder

- ν = The kinematic viscosity of the fluid.

Over a large Re range ($70<Re<10^7$ for circular cylinders), eddies are shed continuously from each side of the body, forming rows of vortices in its wake. The alternation leads to the core of a vortex in one row being opposite the point midway between two vortex cores in the other row, giving rise to the distinctive pattern shown in Figure 4-4.
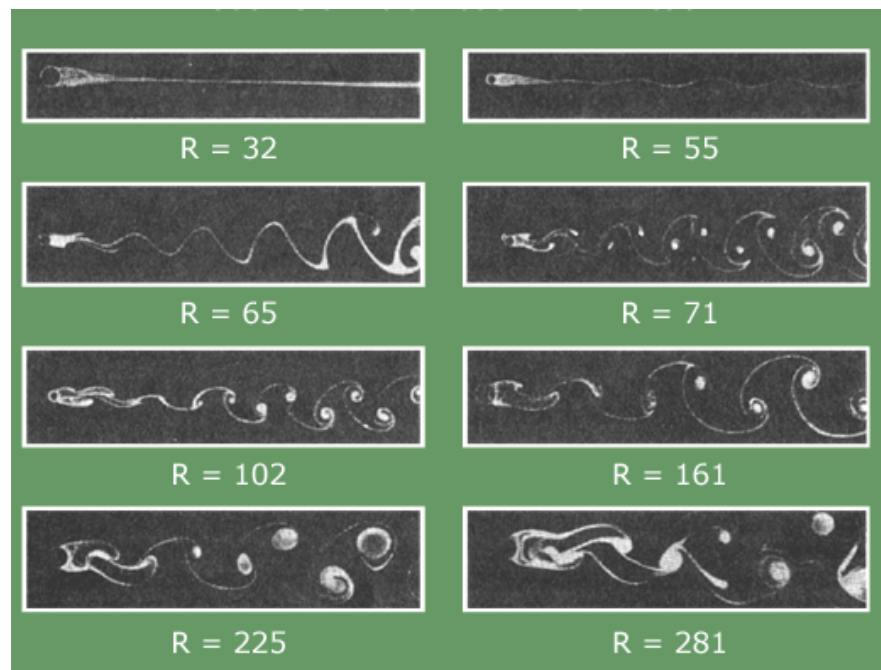
Figure 4-4 Von Karman vortex street in the wake of a cylinder (Reynolds>70).

Ultimately, the energy of the vortices is consumed by viscosity as they move further down stream and the regular pattern disappears, Figure 4-5.
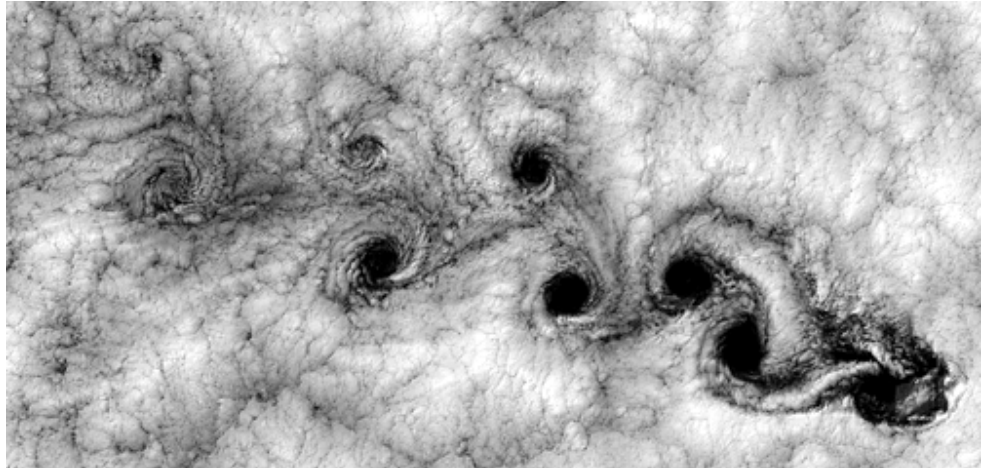
Figure 4-5 Von Kármán vortex street off the Chilean coast near the Juan Fernandez Islands.

The mechanism of noise generation is that the vortex shedding due to the unsteady wake induces a pressure fluctuation on the surface that radiates as sound, this will often be in form of tonal noise as the vortices are shed with a precise frequency. This vortex shedding can result in the production of whistles such as around car aerials or even structural damage as in the case of tall chimneys. This problem can be reduced dramatically by wrapping a helical strake around the cylinder, Figure 4-6.

The ability to accurately compute cylinder noise across a broad range of Reynolds numbers with numerical methods would enhance the understanding of bluff body noise generation mechanisms.

Anyway, a complete understanding of circular cylinder flow is particularly elusive because transition from laminar to turbulent flow occurs in a distinct succession over an enormous range of Reynolds numbers, and each transition state is sensitive to extremely
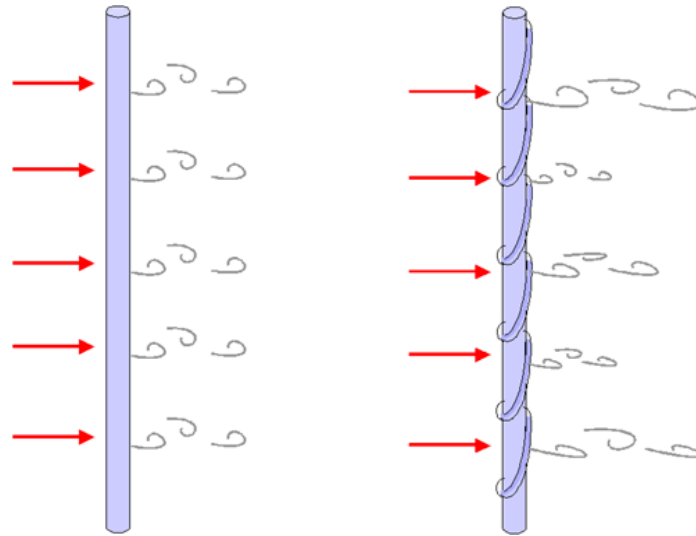
Figure 4-6 The helical strake around the cylinder breaks up the vortex shedding coherence along the span.

small disturbances. These disturbances, such as free stream turbulence and surface roughness, can significantly alter the range of Reynolds numbers over which each transition state occurs. Especially at Reynolds numbers at and above roughly 100,000, experiments can show widely different behaviour due to differences in the experimental flow conditions.

The flow around a circular cylinder is often characterized into three distinct flow regimes: *subcritical*, *supercritical*, and *transcritical*. Subcritical flow indicates purely laminar boundary layer separation. In this regime, regular vortex shedding at a Strouhal number of about 0.2 is observed over a range of Reynolds numbers from roughly 200 to 100,000. The supercritical regime, from Reynolds numbers of roughly 100,000 to 4 million, is characterized by either a dramatic rise in the Strouhal number or else a loss of organized vortex shedding altogether. Also, the wake is noticeably narrower and the forces are much smaller in magnitude. [17] It is somewhere in this regime that transition

69

to turbulence begins to occur on the body at or near the point of separation. In the transcritical regime, above a Reynolds number of roughly 4 million, periodic vortex shedding re-establishes at a higher Strouhal number of 0.26 - 0.30. The cylinder now experiences fully turbulent boundary layer separation and higher force coefficients than in the supercritical regime.

Any attempt to numerically model circular cylinder flow is complicated by the fact that the flow above a Reynolds number of around 180 is three-dimensional, [19,20] raising doubts about the applicability of two-dimensional simulations. Additionally, transition occurs off-body in the wake or shear layer at Reynolds numbers between roughly 200 and the supercritical regime. [13] Without performing very expensive direct numerical simulations (DNS), this behaviour is not captured by numerical methods that solve the Navier-Stokes equations on typical grids used for aerodynamic analysis. This deficiency may or may not be important at lower Reynolds numbers, depending on how far behind the cylinder transition occurs and what feature of the flow is of interest. But it certainly has an adverse effect at higher Reynolds numbers for which transition occurs at or near the separation point on the cylinder. For Reynolds numbers at and above the supercritical regime, Reynolds-averaging with the use of a turbulence model is one way to introduce the important effect of turbulence into a numerical simulation. However, without an accurate built-in transition model, it is difficult, if not impossible, to model the important effects of transition, particularly when it occurs on or near the body. It is not surprising, then, that most numerical studies of flow around a circular cylinder have focused primarily on low Reynolds number flows less than about1000.

At Reynolds numbers of roughly 200 or less, many researchers have successfully computed the Strouhal number and mean drag over circular cylinders (see for example references [21]). At higher Reynolds numbers, however, two-dimensional numerical methods cannot predict the drag and lift forces accurately, due to the increasingly prominent three-dimensionality of the real flow field. Nonetheless, it is still important to try to understand and characterize the capabilities and limitations of two-dimensional analysis as this may yield a deeper insight into the physics of both Aerodynamics and Aeroacoustics at a relatively low cost.

4.3   AIRFOIL SELF-NOISE

Inflow turbulence noise caused by the interaction of the leading edge of an airfoil with a turbulent inflow is often called leading edge noise. Researchers currently think that sharp leading edge geometries are more susceptible to inflow turbulence noise.

Airfoil self-noise is instead due to the interaction between an airfoil blade and the turbulence produced in its own boundary layer and near wake. It is important because it represents the total noise produced when an airfoil encounters smooth non-turbulent inflow. Over the last 20 years, research has been conducted (e.g. at NASA Langley Research Centre) to develop fundamental understanding, as well as prediction capability, of the various self-noise mechanisms. The interest is motivated by its importance to broadband helicopter rotor, wind turbine, and airframe noises.

In Figure 4-7, the subsonic flow conditions for five self-noise mechanisms of concern here are illustrated. At high Reynolds number Rc (based on chord length), turbulent boundary layers (TBL) develop over most of the airfoil. Noise is produced as

this turbulence passes over the trailing edge (TE). At low *Rc,* largely laminar boundary layers (LBL) develop, whose instabilities result in vortex shedding (VS) and associated noise from the TE. For nonzero angles of attack, the flow can separate near the TE on the suction side of the airfoil to produce TE noise due to the shed turbulent vorticity. At very high angles of attack, the 'separated flow near the TE gives way to large-scale separation (deep stall) causing the airfoil to radiate low-frequency noise similar to that of a bluff body in flow.
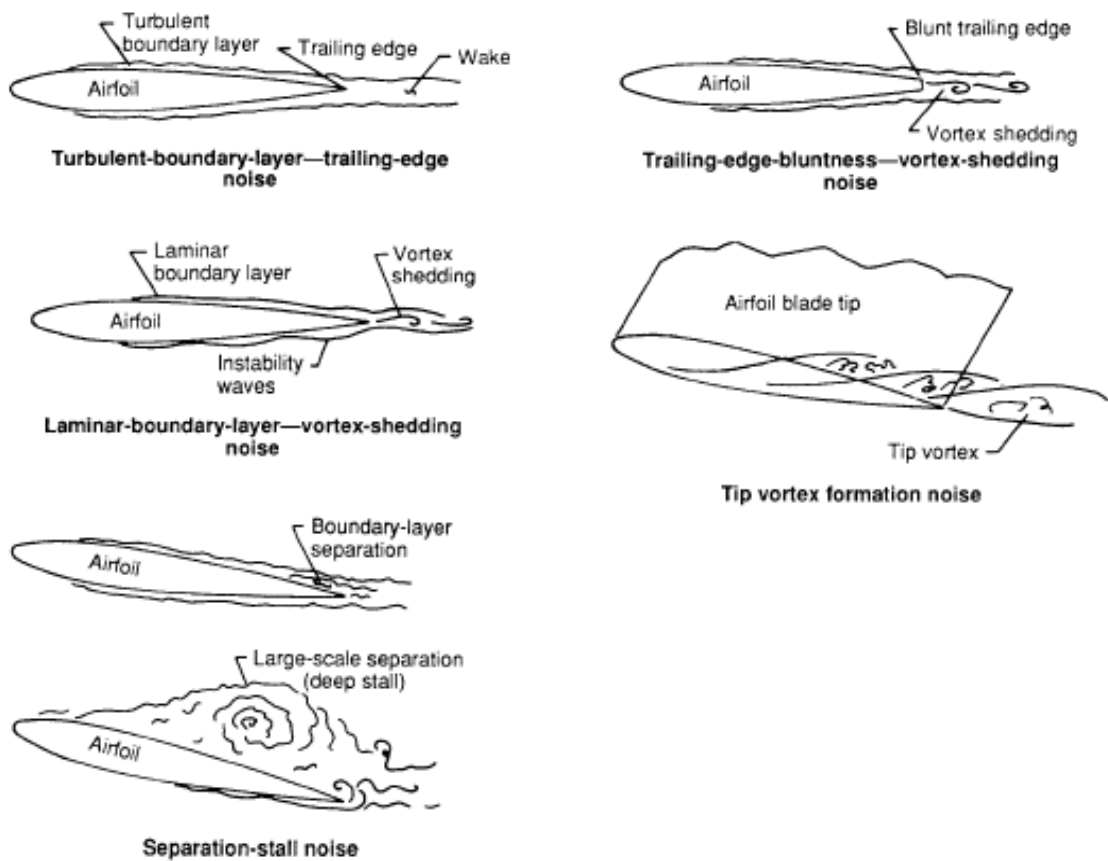
Figure 4-7 Airfoil self-noise generation mechanism.

Another noise source is vortex shedding occurring in the small separated flow region after of a blunt TE. The remaining source considered here is due to the formation of the tip vortex, containing highly turbulent flow, occurring near the tips of lifting blades or wings.

Lots of semi-empirical models have been studied and developed to predict airfoil noise but as it will be shown in the next sections none of them has been really successful and robust over a wide range of different angles of attack, geometries and flow conditions.

4.3.1 Turbulent-Boundary-Layer-Trailing-Edge (TBL-TE) Noise

Using measured surface pressures, Brooks and Hodgson [24] demonstrated that if sufficient information is known about the TBL convecting surface pressure field passing the TE, then TBL-TE noise can be accurately predicted. Schlinker and Amiet [24] employed a generalized empirical description of surface pressure to predict measured noise. However, the lack of agreement for many cases indicated a need for a more accurate pressure description than was available. The NASA Langley Research Centre supported a research effort [24] to model the turbulence within boundary layers as a sum of discrete "hairpin" vortex elements. In a parallel and follow-up effort, in [24] the authors matched measured and calculated mean boundary layer characteristics to prescribed distributions of the discrete vortex elements so that associated surface pressure could be determined. The use of the model to predict TBL TE noise proved disappointing because of its inability to show correct trends with angle of attack or velocity. The results showed that to successfully describe the surface pressure the history of the turbulence must be accounted for in addition to the mean TBL characteristics.

4.3.2 Separation-Stall Noise

Assessments of the separated flow noise mechanism for airfoils at moderate to high angles of attack have been very limited [24]. The relative importance of airfoil stall noise was illustrated in the data of Fink and Bailey [24] in an airframe noise study. At stall, noise increased by more than 10 dB relative to TBL-TE noise, emitted at low angles of attack. Paterson et al. [24] found evidence through surface to far field cross-correlations that for mildly separated flow the dominant noise is emitted from the TE, whereas for deep stall the noise radiated from the chord as a whole. No predictive methods are known to have been developed. A successful method would have to account for the gradual introduction of separated flow noise as airfoil angle of attack is increased. Beyond limiting angles, deep stall noise would be the only major contributing source.

4.3.3 Laminar-Boundary-Layer-Vortex-Shedding (LBL-VS) Noise

When a LBL exists over most of at least one side of an airfoil, vortex shedding noise can occur. The vortex shedding is apparently coupled to acoustically excited aerodynamic feedback loops [24]. The feedback loop is taken between the airfoil TE and an upstream "source" point on the surface, where Tollmien-Schlichting instability waves originate in the LBL. The resulting noise spectrum is composed of quasi-tones related to the shedding rates at the TE. The gross trend of the frequency dependence was found by Paterson et al. [24] by scaling on a Strouhal number basis with the LBL thickness at the TE being the relevant length scale. Simple flat plate LBL theory was used to determine the boundary layer thicknesses δ in the frequency comparisons. The use of measured values of δ [24] verified the general Strouhal dependence. Additionally, for zero angle of

attack, Brooks and Marcolini [24] found that overall levels of LBL-VS noise could be normalized so that the transition from LBL-VS noise to TBL-TE noise is a unique function of Rc. There have been no LBL-VS noise prediction methods proposed, because most studies have emphasized the examination of the rather erratic frequency dependence of the individual quasi-tones in attempts to explain the basic mechanism. However, the scaling successes described above in [24] can offer initial scaling guidance for the development of predictions in spite of the general complexity of the mechanism.

4.3.4   Tip Vortex Formation Noise

The tip noise source has been identified with the turbulence in the local separated flow associated with formation of the tip vortex [24]. The flow over the blade tip consists of a vortex with a thick viscous turbulent core. The mechanism for noise production is taken to be TE noise due to the passage of the turbulence over the TE of the tip region. George and Chou [24] proposed a prediction model based on spectral data from delta wing studies (assumed to approximate the tip vortex flow of interest), mean flow studies of several tip shapes, and TE noise analysis. Brooks and Marcolini [24] conducted an experimental study to isolate tip noise in a quantitative manner. The data were obtained by comparing sets of two- and three-dimensional test results for different model sizes, angles of attack, and tunnel flow velocities.

4.3.5   Noise Trailing-Edge-Bluntness Vortex-Shedding

Noise due to vortex shedding from blunt trailing edges was established by Brooks and Hodgson [24] to be an important airfoil self-noise source. Other studies of bluntness effects, as reviewed by Blake and Brooks and Schlinker [24], were only aerodynamic in

scope and dealt with TE thicknesses that were large compared with the boundary-layer displacement thicknesses. For rotor blade and wing designs, the bluntness is likely to be small compared with boundary-layer thicknesses. Grosveld [24] to obtained a scaling law for TE bluntness noise. He found that the scaling model could explain the spectral behaviour of high-frequency broadband noise of wind turbines. Chou and George [24] followed suit with an alternative scaling of the data to model the noise. For both modelling techniques neither the functional dependence of the noise on boundary-layer thickness (as compared with the TE bluntness) nor the specifics of the blunted TE shape were incorporated. A more general model is needed.

4.3.6   Airfoil Tonal Noise

It is interesting to report the experimental investigations at National Aerospace Laboratory NLR in The Netherlands [49]. A wide testing was performed on different airfoils and airflow conditions to investigate leading edge, trailing edge and tonal noise.

One of the most interesting observations of the test campaign was the presence of intense, narrowband peaks in the trailing edge noise spectra for several airfoils at different operating conditions. These are called "pure tones" and are perceived as such by a listener. They are illustrated in Figure 4-8 for the trailing edge noise spectra of the untripped S834 (α=10°), SG6043 (α=0°) and SD2030 (α=0°) airfoils. The nature of these tones was investigated in more detail at 22.4 m/s, because they were most pronounced at this tunnel speed. The spectra for these cases show peaks at around 1 kHz and 2 kHz for all three airfoils. The angle of attack range for which these tones occurred was estimated by listening in the test section during a sweep of angle of attack. This gave the following ranges: 7.5°<α<13° for S834, -8°<α<2° for SG 6043, and -10°<α<4° for SD 2030.
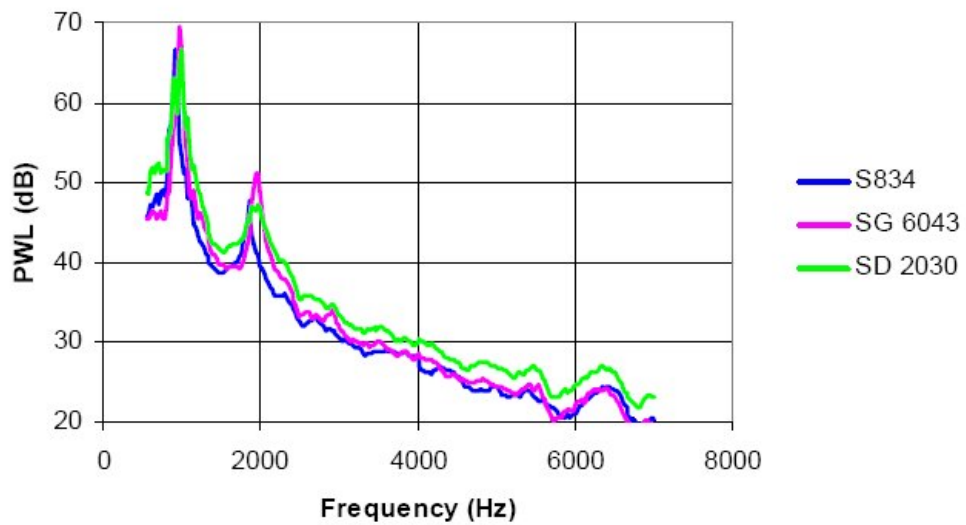
Figure 4-8 Narrowband trailing edge noise spectra for three untripped airfoils that showed intense tones (U=22.4 m/s; α=10° for S834, α=0° for SG 6043 and SD 2030).

Although such tones sometimes result from blunt trailing edge vortex shedding, the extremely thin trailing edges of the models made this unlikely. Calculations of the Strouhal number (*St)*, which is approximately 0.2 for von Kármán vortex shedding, confirmed this was not the cause. It was hypothesized, therefore, that laminar boundary layer vortex shedding caused the tones. To investigate this hypothesis, they applied a different thickness of zigzag tape and observed the effects. By tripping one side of the airfoil at a time, it could be determine where the tones originated. For the S834 and SD2030 airfoils, it was the pressure side, whereas for the SG6043 airfoil, the tones originated from the suction side. Stethoscope measurements on the pressure side of the untripped S834 model indicated a laminar boundary layer up to about 80% chord. With tripping, transition to a turbulent boundary layer occurred directly behind the trip at 5%

chord. This observation supported the hypothesis that the tones were due to laminar boundary layer vortex shedding.

Another interesting observation was that the tones disappeared in the presence of upstream turbulence. Observation of the source plots with and without the turbulence grid showed that the inflow turbulence removed the trailing edge tones, and the grid noise became dominant. Evidently, the inflow turbulence interrupts the feedback mechanism responsible for the tones.

Figure 4-9 shows the airfoils used for the tests at NLR.

Figure 4-9 Wind tunnel airfoil models.

4.4 PROPELLER NOISE

A propeller can be generally described as an open (un-shrouded), rotating, bladed device. Although there are many differences in details among various designs and applications, such as number of blades, blade shape, and airfoil section, the noise-generating process is basically the same for all. The major propeller noise components are thickness noise (due to the volume displacement of the blades), steady-loading noise (due to the steady forces on the blades), unsteady-loading noise (due to circumferentially non-uniform loading), quadrupole (nonlinear) noise, and broadband noise. Although the relative importance of these sources depends on design and operating conditions, defining them will completely describe the acoustic signature of a propeller.

One important consideration is the effect of installation on the noise produced by a propeller. This effect is essentially the difference between the laboratory environment and the real world. It is generally assumed that in a laboratory environment conditions are ideal, that is, the propeller is operating in perfectly uniform flow. For an operational propeller, this is never the case. Propellers are always operating in a flow field that has some distortion. This can be from the wing up-wash, the pylon wake, the airplane angle of attack, or the inflow turbulence. Since this distortion leads to additional noise, it is a factor which must be considered in defining the total noise of an operational propeller.

4.4.1 High Performance Propeller and Installation Noise

The blades of a propeller are designed to produce a region of low pressure on one side and high pressure on the other. The resulting forces induce air from the front and

push it back, resulting in thrust. Because propellers impart a relatively small amount of velocity to a large mass of air, their efficiencies are high.
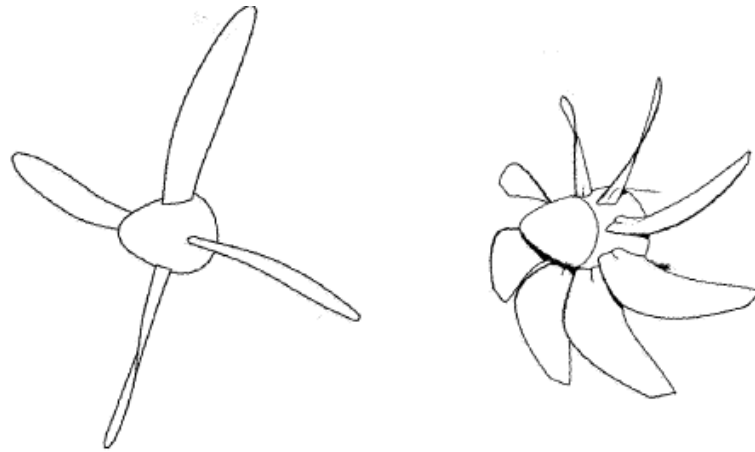
High-performance, low-speed propeller for moderate-flight-speed commuter airplane propulsion.

Propfan propulsion system for high subsonic cruise speed applications.
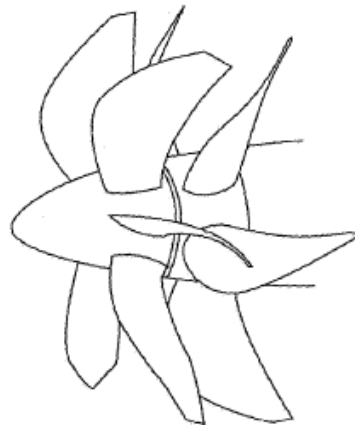
Counterrotating-propfan propulsion system for high subsonic cruise speed applications.

Figure 4-10 High Performance Propellers.

However, the efficiencies of conventional propellers tend to fall off at high speed. This has led to a variation of the propeller called the propfan. The propfan is also an open rotor, but compared with conventional propellers it has a smaller diameter for a given

thrust and has more blades, which are swept. To improve efficiency further, a second rotor can be added behind a propeller, resulting in a counter-rotating propeller.

A typical high-performance, modern propeller in widespread use on commuter airplanes is shown in Figure 4-10. These propellers have two to six relatively straight, narrow blades. Although this type of propeller is well-suited for moderate flight speed (below a Mach number of about 0.65), its performance decreases at higher flight speeds. The primary limitation of this propeller is associated with high drag at high speed due to blade thickness and large relative blade section speed.

The propfan, shown in Figure 4-10, has been developed to extend the practical flight envelope of the propeller. Compared with conventional propellers, the propfan has more blades (from 6 to 12), uses thin airfoils and swept blades to provide good aerodynamic performance at high speed, and operates at much higher power loading to reduce the diameter. One factor leading to loss of efficiency in propellers is swirl in the wake resulting from engine torque. Generation of swirl uses energy but does not contribute to thrust. The amount of swirl is related to the power loading. One concept to recover the swirl losses is to add a second blade row behind the first. This is shown in Figure 4-10 for the propfan. The second blade row rotates in the direction opposite to that of the first, thus cancelling its swirl. This cancellation can result in performance increases of 8 to 10 percent compared with that of single rotation propellers [23].

In considering the noise of propellers and propfans, it is important to address the installation of these devices, as this can have a significant effect on the noise generation process. In their simplest forms noise calculation procedures and analyses assume uniform conditions, that is, the loads on the blades are absolutely steady.

81

In actuality, that is rarely the case. Although laboratory tests can be conducted such that the incoming flow is uniform and free of turbulence, the real environment is never as ideal. The amount of distortion is generally related to two parameters: operating conditions and installation.

Operating conditions include static (zero flight speed) or forward flight. In flight, the propeller can be at an angle of attack. Static conditions give rise to severe inflow distortion and the resulting noise is vastly different than that from propellers in flight. Angle of attack or skewed inflow causes unsteady loading, with periodicities equal to one cycle per rotation. Regarding installations, the cleanest configuration is in front of a long, slender, axisymmetric nacelle. The worst is probably behind a wing. Intermediate configurations include wing-mounted tractors, aft-mounted tractors in front of a pylon, and aft-mounted pushers behind a pylon. These installations result in varying degrees of inflow distortion which typically results in added sources (unsteady loading noise) and increases the noise produced by the propeller.

It is thus important to evaluate the propeller as an installed system rather than as an isolated component when noise requirements are addressed. If a propeller is designed to meet the noise goals, even with a comfortable margin of error, ignoring installation effects can result in a substantial under-prediction of the system noise, with the strong possibility that the airplane will not meet the noise requirements.

Thus, there is a growing interest in CFD Aeroacoustics Simulations because they could address the issue of modelling the whole system: installed propeller in real operating conditions.

4.4.2 Propeller Noise Characteristics

Propeller noise can be classified into three categories: harmonic noise, broadband noise, and narrow-band random noise.

Harmonic noise is the periodic component, that is, its time signature can be represented by a pulse which repeats at a constant rate. If an ideal propeller with B blades is operating at constant rotational speed N, then the resulting noise appears as a signal with fundamental frequency BN. The blade-passage period is $1/BN$. Typically the generated pulse is not a pure sinusoid, so that many harmonics exist. These occur at integer multiples of the fundamental frequency. The first harmonic is the fundamental, the second harmonic occurs at twice the fundamental frequency, and so on. Figure 4-11 illustrates the characteristics of harmonic noise in both the time and frequency domains.
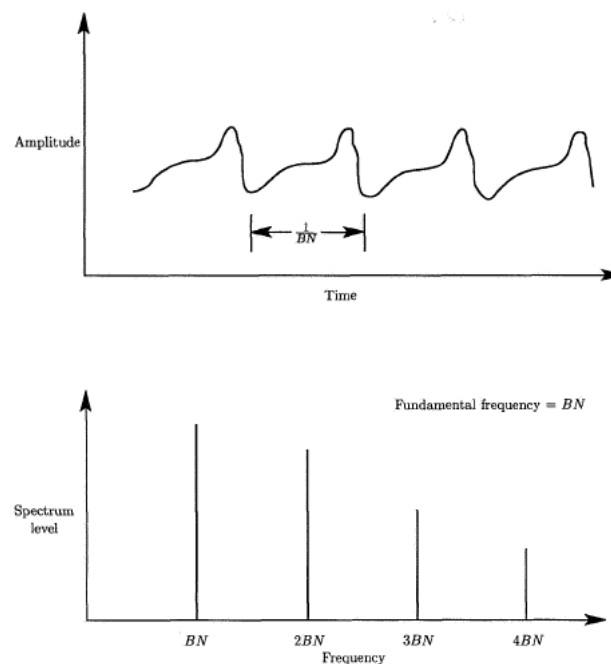
Figure 4-11 Characteristics of propeller rotational noise.

Broadband noise is random in nature and contains components at all frequencies.

A typical broadband noise signal for propellers is shown in Figure 4-12. The frequency spectrum is continuous, although there may be a "shape" to it because not all frequencies have the same amplitude.
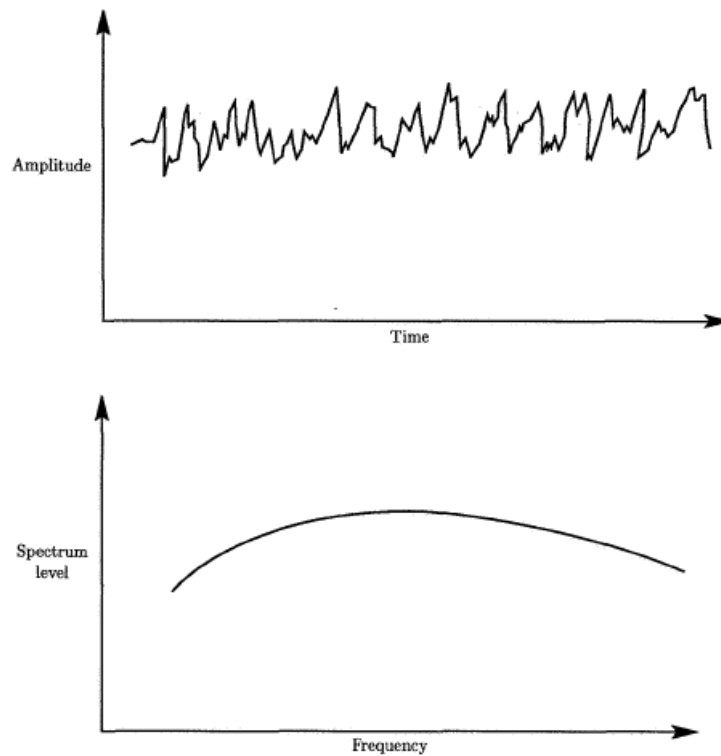
Figure 4-12 Characteristics of propeller broadband noise.

Narrow-band random noise is almost periodic. However, examination of the harmonics reveals that the energy is not concentrated at isolated frequencies, but rather it is spread out. As illustrated in Figure 4-13 the signal may appear periodic, but certain components do not repeat exactly with time. The frequency spectrum shows discrete components, but these spread out, particularly at the higher frequencies.
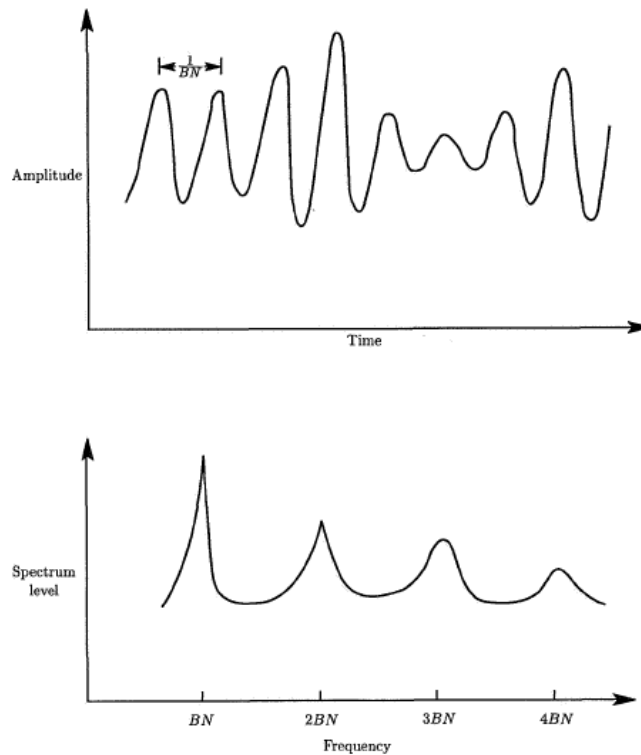
Figure 4-13 Characteristics of propeller narrow-band random noise.

The mechanisms which lead to the generation of the spectral characteristics discussed above are described in this section.

4.4.3   Steady Sources

Steady sources are those which would appear constant in time to an observer on the rotating blade. They produce periodic noise because of their rotation. Noise sources are usually divided into three categories: linear thickness, linear loading, and (nonlinear) quadrupole.

Thickness noise arises from the transverse periodic displacement of the air by the volume of a passing blade element. The amplitude of this noise component is

proportional to the blade volume, with frequency characteristics dependent on the shape of the blade cross section (airfoil shape) and rotational speed.

Thickness noise can be represented by a monopole source distribution and becomes important at high speeds. Thin blade sections and planform sweep are used to control this noise.

Loading noise is a combination of thrust and torque (or lift and drag) components which result from the pressure field that surrounds each blade as a consequence of its motion. This pressure disturbance moving in the medium propagates as noise. Loading is an important mechanism at low to moderate speeds.

For moderate blade section speed, the thickness and loading sources are linear and act on the blade surfaces. When flow over the blade sections is transonic, nonlinear effects can become significant. In aeroacoustic theory these can be modelled with quadrupole sources distributed in the volume surrounding the blades.

In principle, the quadrupole could be used to account for all the viscous and propagation effects not covered by the thickness and loading sources. However, the only practical application of this term to propeller acoustics has been its evaluation in the non viscous flow close to the blade surface. At transonic blade section speeds the quadrupole enhances the linear thickness and loading sources and causes a noise increase for unswept, high-tip-speed propellers and helicopter rotors.

4.4.4 Unsteady Sources

Unsteady sources are time dependent in the rotating-blade frame of reference. They include periodic and random variation of loading on the blades. A typical example of periodic blade loading in propellers is the effect of shaft angle of attack. When the

propeller axis is tilted relative to the inflow, each blade sees a cyclic change in local angle of attack. As a consequence, the loading on the blade varies during a revolution. The loading change may be once per revolution or several times per revolution, depending on the source of inflow distortion. All inflow distortion which is invariant with time results in blade-loading changes which repeat exactly for every propeller revolution. The resulting periodic unsteady-loading noise occurs at harmonics of blade-passage frequency.

Depending on the circumferential location of the loading disturbance relative to the observer, unsteady-loading noise can add or subtract from the steady-loading noise. The noise directivity is no longer axisymmetric and a third coordinate is needed to define it. The circumferential directivity exhibits lobes-peaks and valleys-with the number of lobes dependent on the order of the distortion and unrelated to the number of blades. For example, a propeller behind a wing might show two circumferential directivity lobes regardless of the number of blades on the propeller. Unsteady loading is an important source in the counter-rotating propeller.

Although the counter-rotating propeller does not contain any additional or unique sources of noise, the aerodynamic interference between the two rotors gives rise to significant levels of unsteady-loading noise which are particularly significant at low flight speeds, such as during takeoff and landing. Each front rotor blade leaves a wake which convects into the rear rotor. This wake can be complex, consisting of downwash due to the lift on the blades, velocity deficits due to the drag of the blade sections, and tip vortices. This convection results in a sequence of lift pulses on the rear rotor blades. Another mechanism is the potential field (due to blade loading) of the rear rotor creating

a disturbance which is felt by the aft part of the front rotor blades. The magnitude of this source depends on the level of loading on the rear rotor and the spacing between the two rotors.

Aerodynamic interaction in counter-rotating propellers is a significant source of noise for low-speed operation. At higher flight speeds, such as during cruise, the aerodynamic interaction becomes less important because the steady sources (thickness, steady loading, and quadrupole) become dominant.

Under certain conditions blade loading which is nearly periodic can occur. An example of this is the ingestion of a vortex, which could be induced by the propeller and attached to the fuselage or to the ground ahead of the propeller. In this example, a local distortion is induced by and drawn into the propeller. The blades chop through the distortion and a blade-loading pulse is produced. Because the distortion can persist for several propeller revolutions, the unsteady-loading noise can appear at blade-passage frequency harmonics. However, as conditions change, the location of the distortion changes and the amplitude and phase of the unsteady-loading noise change. These changes broaden the noise spectrum, as previously described for narrow-band random noise.

4.4.5   Random Sources

Unsteady Random sources give rise to broadband noise. For propellers there are two sources which may be important, depending on the propeller design and operating conditions. The first broadband noise source is the interaction of inflow turbulence with the blade leading edges. Because the inflow is turbulent, the resulting noise is random. The importance of this noise source depends on the magnitude of the inflow turbulence,

but it can be quite significant under conditions of high turbulence at low speeds. In the second broadband mechanism, noise is generated near the blade trailing edge. A typical propeller develops a turbulent boundary layer over the blade surfaces, which can result in fluctuating blade loading at the trailing edge. The noise is characterized by the boundary-layer properties. A related mechanism occurs at the blade tips, where turbulence in the core of the tip vortex interacts with the trailing edge.

It has been determined for full-scale propellers in flight that the broadband noise sources are relatively unimportant and do not contribute significantly to the total noise [23].

4.4.6 Non Linear Effects

Unsteady Blade sections of propfans and of many other high-speed propellers operate at transonic velocities. In the aerodynamics of wings and bodies, this is a regime frequently dominated by nonlinear effects. The corresponding propeller issues are discussed below under the categories of nonlinear source effects from the acoustic analogy quadrupole and full aerodynamic solutions by applying finite element methods.

At high speeds, nonlinearity may occur at the source (i.e., at the blade section) because of transonic effects. One way of dealing with this is via the quadrupole source term in the acoustic analogy. The first valid analysis of the importance of the quadrupole source for high-speed rotors was made based on a two-dimensional aerodynamic calculation [23]. The quadrupole contribution was compared with the linear thickness source for a propfan airfoil section; the results are shown in Figure 4-14. These results show that quadrupole, or nonlinear, source effects are important sources of additional

noise in the blade section speed range between critical Mach number (when flow over the airfoil exceeds the speed of sound) and a Mach number of 1.
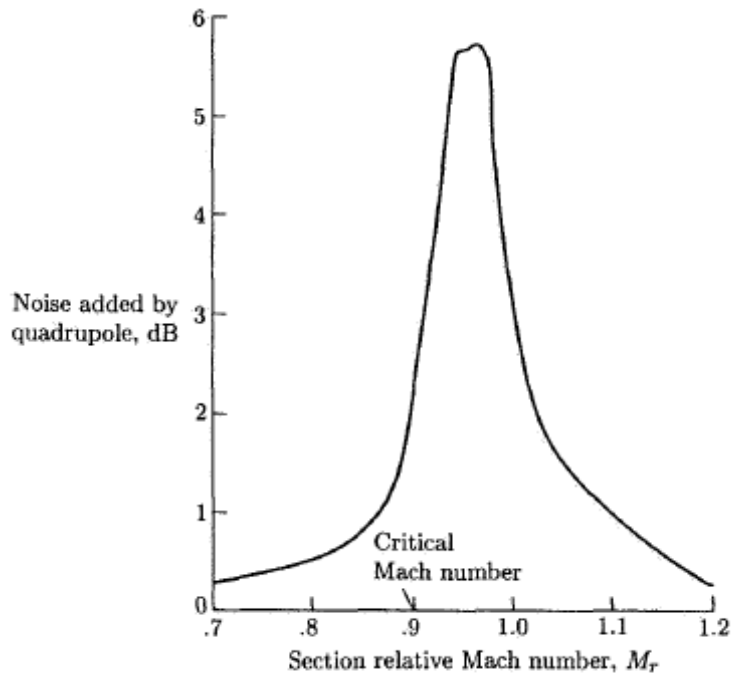
Figure 4-14 Increase of blade thickness sound pressure level caused by including quadrupole noise [23].

Quadrupole strength can be reduced to below that of linear thickness and loading sources by blade sweep so the airfoil sections operate effectively below their critical Mach numbers. To shed more light on the role of the quadrupole term in flow with solid surfaces, Blackburn examined the field of a two-dimensional wedge in fully supersonic flow [23]. He was able to compute the acoustic analogy source terms exactly and found that the quadrupole was not a significant source of extra noise in this flow regime. This finding agrees with Figure 4-14, since the Mach number in Blackburn's analysis is well to the right of the peak. However, Blackburn did find that the quadrupole term

90

repositioned wave fronts along the shocks, rather than on the Mach surfaces as in linear theory.

Quadrupole sources have been treated more extensively in the helicopter literature because supercritical blade section speeds are common. However, for propellers and propfans, nonlinear effects are minimized by blade designs with sweep and thin airfoil sections.

Another approach to nonlinear effects is as a by-product of an aerodynamics calculation. There is considerable work on the transonic regime in progress to develop numerical methods for aerodynamic design and analysis from full-potential, Euler, and Navier-Stokes equations. For the steady-loading problem, it is tempting to believe that since these methods compute all the flow-field variables in a finite domain surrounding the propeller, the noise signal is available simply by sampling the pressure field at the appropriate locations. This, in principle, is true. However, the currently existing aerodynamic analysis methods are designed to give the best accuracy on the surfaces of the blades. For field points at a distance from the blades, predictions are degraded because the mesh sizes used in the calculation increase, numerical damping smoothes the waves, and the boundary conditions at the outer edges of the computational domain are treated approximately. These problems all appear to be manageable for the steady-loading aerodynamics problem, but so far they have not been addressed for acoustic calculations. However, recent advances in computational fluid dynamics are now making this approach look more practical.

4.5   JET NOISE

Jet noise has become an important issue today because the current levels of noise produced by jet engines are still above acceptable limits, particularly during takeoff. This leads to unacceptable noise pollution and consequently places a financial burden on an already struggling commercial aerospace industry. This is because some airports have flight restrictions during certain hours based on noise generated and a reduced number of flights must be flown. Also, if the noise level of aircraft engines is above a certain level, airports can be financially penalized. The development of high-bypass ratio turbofan engines has helped to alleviate jet noise somewhat by reducing the effective velocity of the jet exhaust, Figure 4-15. Further reductions in jet noise are still needed, as the large bypass ratios of modern commercial engines are reaching their limits [39].
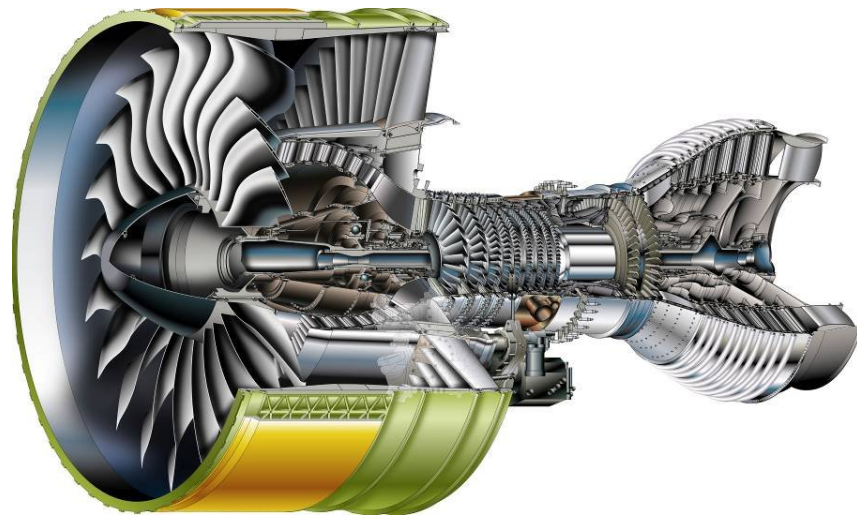
Figure 4-15 High bypass turbofan.

4.5.1   Jet Noise Physics

The development of jet noise theory began in 1952 when Lighthill linked the intensity of jet noise to the 9th power of the relative jet exhaust velocity. It was later determined that for lower Mach number jets, the noise intensity is proportional to the 8th power of the relative jet velocity and for higher Mach number jets the noise intensity is proportional to the 3rd power of the relative jet exhaust velocity [23]. Lighthill's approach was strictly mathematical, though, and his governing equation did not lend insight into the specific physical mechanisms that govern jet noise.

Through various research efforts over the years, it has been determined that jet noise is physically caused by the interaction of turbulence structures in the jet's shear layer. A general schematic of the different regions of jet exhaust is shown in Figure 4-16.
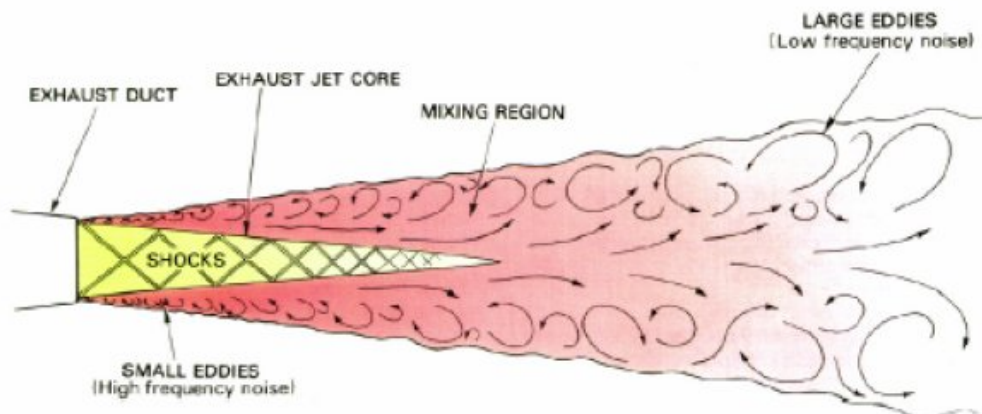
Figure 4-16 Schematic showing the different regions of an exhausting jet flow (ref. Antoine 2000).

The jet's shear layer, referred to as the mixing region of the jet in Figure 4-16, is the boundary between the exhausting jet flow and the ambient air. In this shear layer, the turbulence structures (referred to as "eddies" in Figure 4-16) are formed from the shearing between the high-speed jet flow and the ambient air. These turbulence structures

have different length scales associated with them. The fine-scale turbulence structures ("small eddies" in Figure 4-16) are formed near the jet exit and radiate noise in directions close to perpendicular with the jet axis. The large-scale turbulence structures ("large eddies" in Figure 4-16) are formed further downstream of the nozzle exit as the shear layer grows and the smaller-scale turbulence structures begin to interact and combine. The large-scale turbulence structures tend to radiate noise in the downstream direction as they travel downstream [40].

The cone shaped area close to the nozzle exit and before the mixing layer is known as the "potential core" of the jet and is the region where the jet flow is still uniform and no mixing is taking place.

Since different turbulence structure scales radiate noise in different directions, the SPL observed from the jet will be different depending upon the angular location relative to the jet axis. Figure 4-17 shows how the jet noise spectra changes for an observer at an angle, θ, from the jet axis. As θ is increased, the SPL peak levels are over a narrower frequency band and peak amplitude increases with the maximum SPL observed at $\theta = 30^{\circ}$. The lowest SPL peak amplitude is observed at $\theta = 90^{\circ}$.

Gas Dynamics and Turbulence Laboratory at the Ohio State University, a 3-D eight microphone array oriented at $\theta = 30^{\circ}$ was used to determine the locations where noise is generated in a Mach 1.3 cold jet flow. In conjunction with the 3-D microphone array, a laser-based flow visualization system was used to capture images of the Mach 1.3 jet. By correlating the data from the 3-D microphone array and the flow visualization
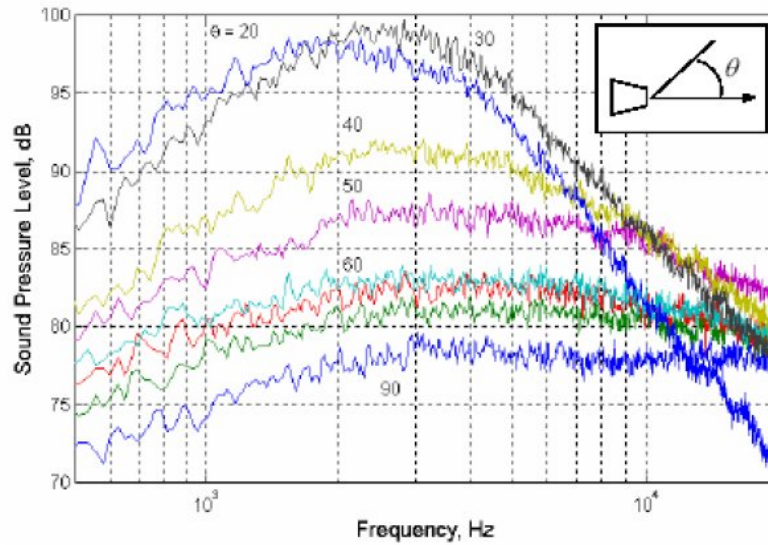
Figure 4-17 The effect of changing observation angle on the observed far-field acoustic spectra of a jet [40].

system, the interactions and physical characteristics of the large-scale turbulence structures during periods of noise generation were captured. From these experiments it was shown that the loudest noise peaks were produced in the jet when the large-scale turbulence structures interact near the end of the potential core, roll up into each other, tear and stretch [40].

This was the first time that the specific interactions of the large-scale turbulence structures in the jet mixing layer were visualized during actual periods of noise generation and tremendous insight was gained as to the physical mechanisms in a jet that cause noise. Still the data was mostly qualitative in nature and much work still needs to be done.

From Lighthill's theory it was derived that in the initial mixing region the overall effective source strength is constant, but downstream of the end of the potential core the

95

strength falls as $1/y_1^7$, Figure 4-18. This result was found by Lilley and independently by Ribner [23].
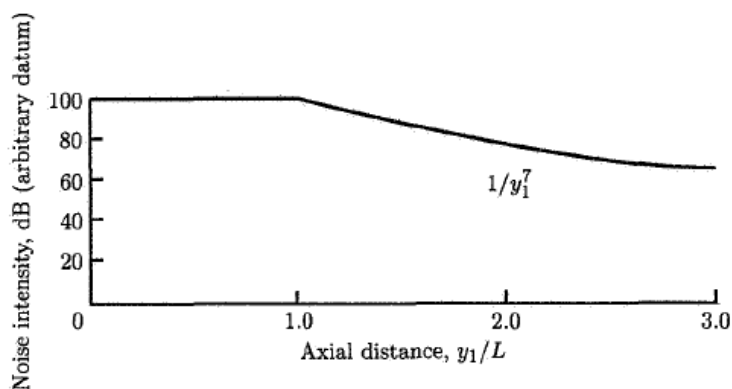
Figure 4-18 Jet noise effective source distribution at low Mach numbers for static jet.

In Figure 4-19 the corresponding results are given for the effective source distribution along the jet axis for a series of constant values of the far-field Strouhal number. These results show that the high-frequency end of the far-field spectrum is generated almost entirely from turbulence in the initial mixing region, whereas the low frequencies are generated over a very large region of the jet extending far downstream (this is also shown qualitatively in Figure 4-16). The region of most intense radiation is near the end of the potential core and is centred at St = 2.0 (St is the Strouhal number = $\omega D_j/V_j$ where $\omega=2\pi f$, D_j is the diameter of the jet at the exit, and V_j is the jet velocity at the nozzle exit). In summary, we see that the main contribution to the power spectral density for Strouhal numbers from 0.1 to 2.0 comes from the region $y_1/D_j = 5$ to 20, while for Strouhal numbers greater than 2.0 the region of greatest contribution stretches from $y_1/D_j = 0$ to 5. In the region near the end of the potential core the dominant frequency has values of $\omega D_j/V_j = 0.3$ to 0.5. Although the low-frequency noise-generating

region is spread over a very large region of the jet downstream of the potential core, its

contribution to the total far-field noise power is small.
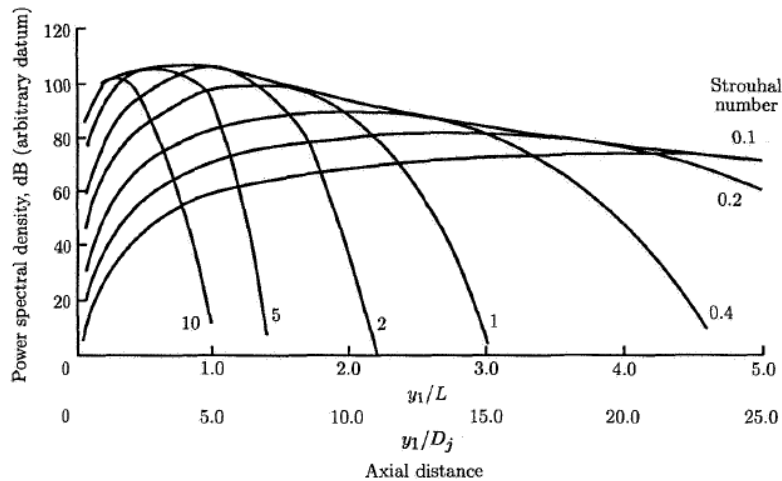
**Figure 4-19 Jet noise effective source distribution at low Mach numbers for constant
Strouhal number.**

4.5.2 Heated Jet Noise – The Effects of Increased Temperature

Due to the success at the Gas Dynamics and Turbulence Laboratory at the Ohio

State University in observing the physical structures that are responsible for the loudest

jet noise in Mach 1.3 cold jets, the interest has turned to studying heated jets. Since an

actual jet engine's exhaust is heated to around $1000\ ^{\circ}F$, a Mach 0.9 heated jet provides a

better model for a jet engine exhaust flow since the temperature effects on the jet noise

can be captured.

To begin to understand the effects of temperature on jet flow it is necessary to

first define a few terms and equations. First off, the jet Mach number, M_j, is the ratio of

the jet velocity, V_j, at the nozzle exit to the local speed of sound in the jet flow, a_j, and

is given by the following equation:

$$M_j = \frac{V_j}{a_j}$$

(4.2)

where, $$a_j = \sqrt{\gamma R T_j}$$

(4.3)

In equation 4.3, γ is the ratio of specific heats and is equal to 1.4 for air. R is the

gas constant and is equal to 287 J/(kg-K). T_j is the static exit temperature of the jet in

absolute units. Substituting equation 4.3 into 4.2 and solving for V_j yields:

$$V_j = M_j \sqrt{\gamma R T_j}$$

(4.4)

From equation 4.4, it follows that for a constant Mach number, V_j will increase in

proportion to $T^{1/2}$. Since jet noise is proportional to the 8th -power of V_j it seems that the

jet noise will increase as temperature increases (again, assuming a constant Mach

number), Figure 4-20 [39].

Temperature also impacts the Reynold's number of the jet, based on the jet diameter

and jet velocity. In general, as the Reynold's number of the jet increases the turbulence in

the jet increases. As shown before, V_j increases with increasing temperature, which

would thus increase the Reynold's number. However, the kinematic viscosity also

increases with increasing temperature and more rapidly than V_j. Thus, as temperature is

increased the Reynold's number of the jet decreases.
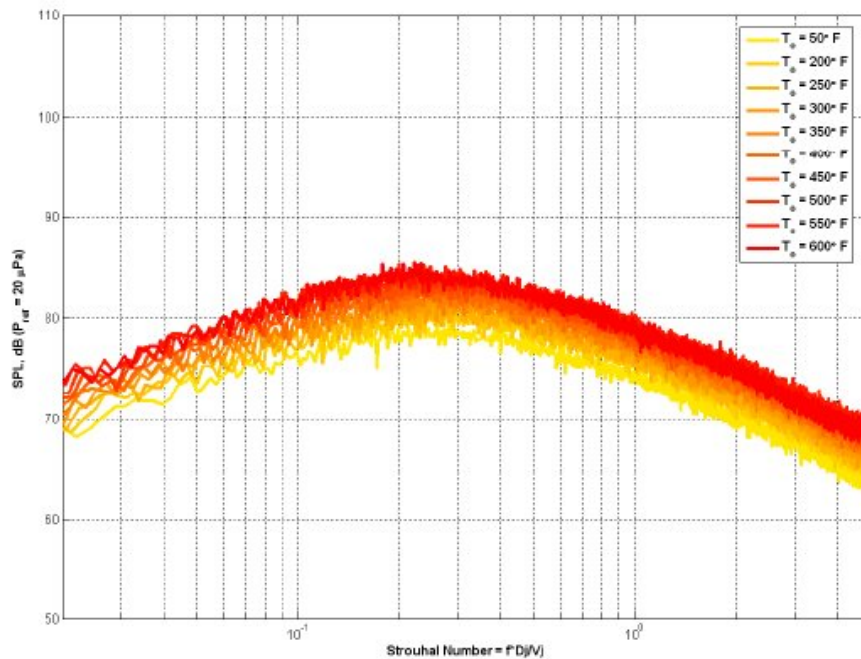
Figure 4-20 Mach 0.9 heated jet spectra taken at θ = 90^0 with the jet axis (in the nozzle exit plane). Frequency has been normalized by the Strouhal number. The noise is higher for increasing temperature [39].

As the Reynold's number of the jet decreases, the turbulence in the jet decreases and if the Reynold's number decreases far enough, it is possible for the jet's boundary layer to change from turbulent to transitional or laminar. This is known as the "Reynold's number effect".

If the jet boundary layer transitions away from turbulent, the physical structure of the jet will change and different mechanisms will become responsible for jet noise.

In fact it must be highlighted that other experiments right at M=0.9, but with some different conditions, shows different trends indeed, that is at increasing temperature the noise emitted for a wide range of frequencies is reduced [37, 38], Figure 4-21, this can also depend on the scaling of the spectrum [37].
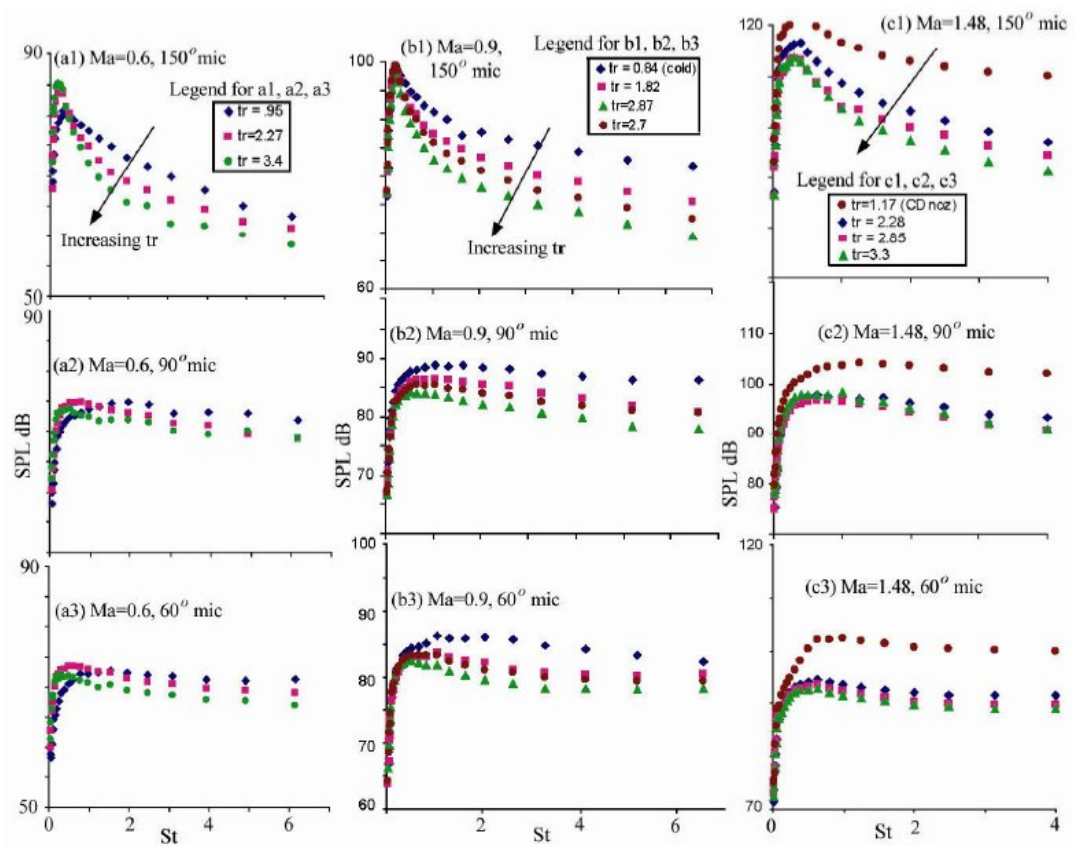
Figure 4-21 Mach 0.6, 0.9, 1.47 heated jet spectra taken at different angle to jet axis (in this case the positive jet axis is opposite to the jet flow direction). Frequency has been normalized by the Strouhal number. The noise is lower for increasing temperature [37].

5 EXAMPLES OF AEROACOUSTICS SIMULATIONS

5.1 CAVITY NOISE

The discrete frequency sound produced by the flow of air at low subsonic speeds over a deep cavity was investigated. This benchmark problem is reported in "Fourth Computational Aeroacoustics (CAA) Workshop on Benchmark Problems, NASA/CP—2004-212954", [36]. A long aspect ratio rectangular cavity with a leading edge overhang that cut off ½ of the cavity opening was placed flush with the top surface of a wind tunnel, see Figure 5-1. The approach flow velocity is 50 m/s. Boundary layer measurements conducted with a single element hotwire anemometer indicated that the boundary layer thickness just upstream of the cavity was equal to 17 mm. Sound pressure level measurements were made at three locations in the cavity: the centre of the leading edge wall, the centre of the cavity floor, and the centre of the trailing edge wall. Three discrete tones were measured at all three locations with corresponding Strouhal numbers (based on cavity opening length and approach flow velocity) equal to 0.24, 0.26, and 0.41. The amplitudes of each tone were approximately equal at each measurement location in the cavity. Measurements made at other approach flow conditions indicated that the approach flow velocity and the boundary layer thickness affected the frequency characteristics of the discrete tones.
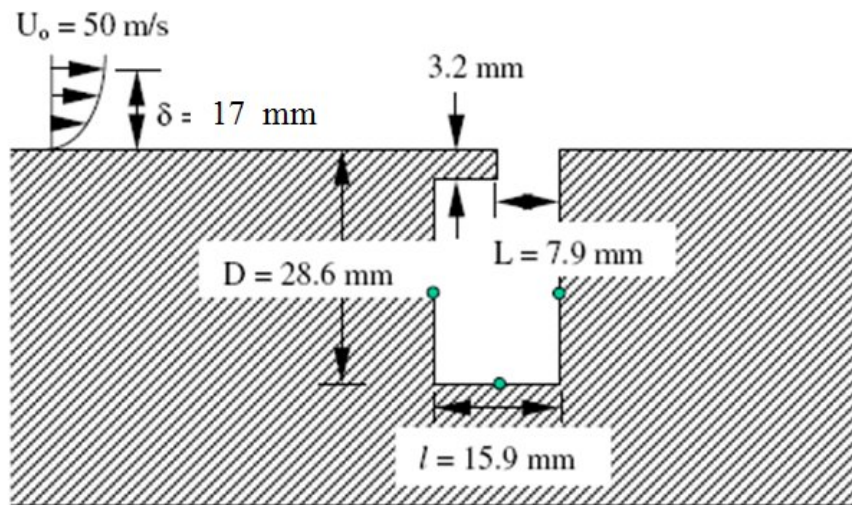
Figure 5-1 The cavity geometry used for the benchmark problem. The microphone measurements are located at the green circles.

The production of discrete frequency sound by the flow of air over a cavity occurs at low subsonic approach flow speeds for many automotive applications such as those associated with car door gaps and sunroofs, and at high subsonic or supersonic approach flow speeds for many aeronautical applications.

5.1.1 Experiments

The experiments were conducted in the 0.46 m x 0. 46 m test section of the recirculating wind tunnel at Kettering University. The tunnel was equipped with silencers before and after the fan.

The Plexiglas cavity shown in Figure 5-2 was placed along the upper surface of the wind tunnel and spanned the entire tunnel cross section. End caps were placed at the outer edges of the cavity so that only the cavity mouth remained open to the flow.

Condenser microphones, 6.35 mm in diameter, were mounted in the centre of the cavity leading edge wall, the centre of the cavity trailing edge wall, and the centre of the cavity floor at a single cavity cross-section. The resulting power spectra were obtained with an 8 Hz bandwidth FFT.

(a)

(b)
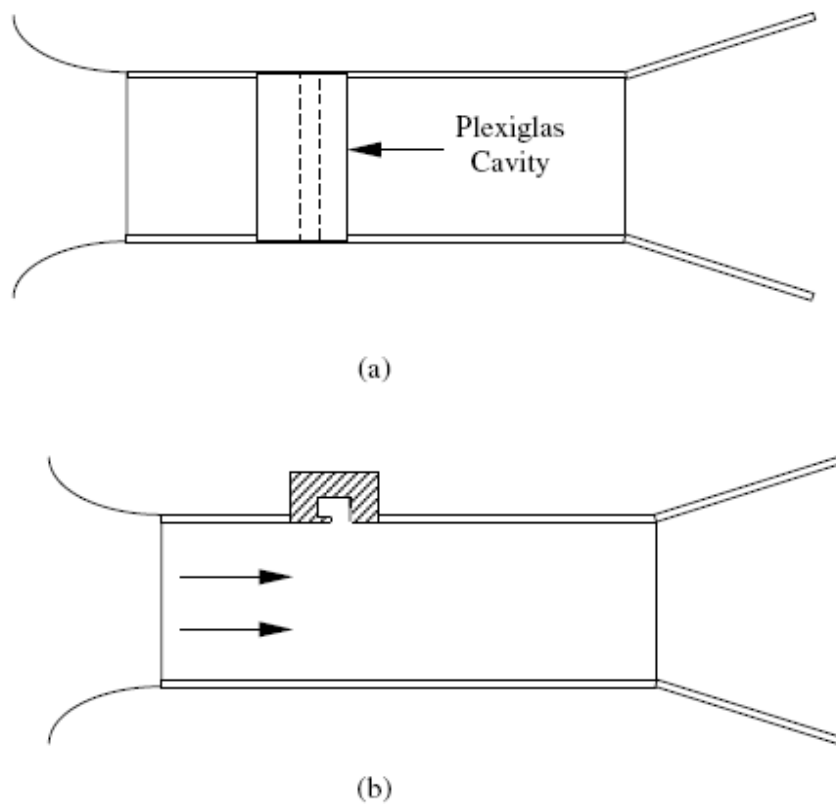
Figure 5-2 Schematics of the wind tunnel test section with the cavity showing (a) the top view and (b) the side view.

Boundary layer measurements were made with a single element hot wire anemometer traversed vertically near the wind tunnel top surface at different axial locations in the test section. A continuous test section surface (no cavity present) was used during the boundary layer studies. Although the benchmark problem statement

103

called for a boundary layer thickness of 14 mm, the boundary layer studies indicated that the thickness of the boundary layer at a location corresponding to the cavity entrance was 17 mm when the approach flow velocity was 50 m/s. Additional acoustic measurements were made for a second axial position in the test section 65 cm upstream of the original cavity location. The boundary layer was thinner in this region of the test section. Measurements made at the second location served to determine the sensitivity of the acoustic radiation to changes in the boundary layer thickness.

5.1.2   Simulation Set Up

An URANS compressible simulation was performed with the commercial code FLUENT 6.3.26. In Figure 5-3 it is showed the computational hexahedral grid of 59785 cells. CAA approach was used for noise computation as motivated in Section 4.1.

It is very important to accurately design the grid according to the particular aeroacoustic simulation. In this case it is known that the driving phenomenon is the instability in the shear layer region which couples with the acoustic response of the cavity. Hence, the grid must be highly refined in the shear layer region. It must also be considered that the cavity acts as a Helmholtz resonator, which means that the wave-length of the pure tone of the coupled system is larger than the dimension of the cavity itself. This tells us that we do not need a high resolution mesh in the cavity. The grid is stretched as it approaches the boundaries in order to dissipate the pressure waves and prevent unwanted reflections at the domain boundaries. This is done because the FLUENT 6.3.26 Pressure Based Coupled Solver does not allow for use of non-reflective boundary conditions. Larger cells at the boundaries also act as a numerical filter, dumping high frequency information from the flow field.

The simulation was started as steady state to reach a good developed flow field and then unsteady solver settings were selected to introduce transient effects. This speeds up the over-all run time of the simulation.
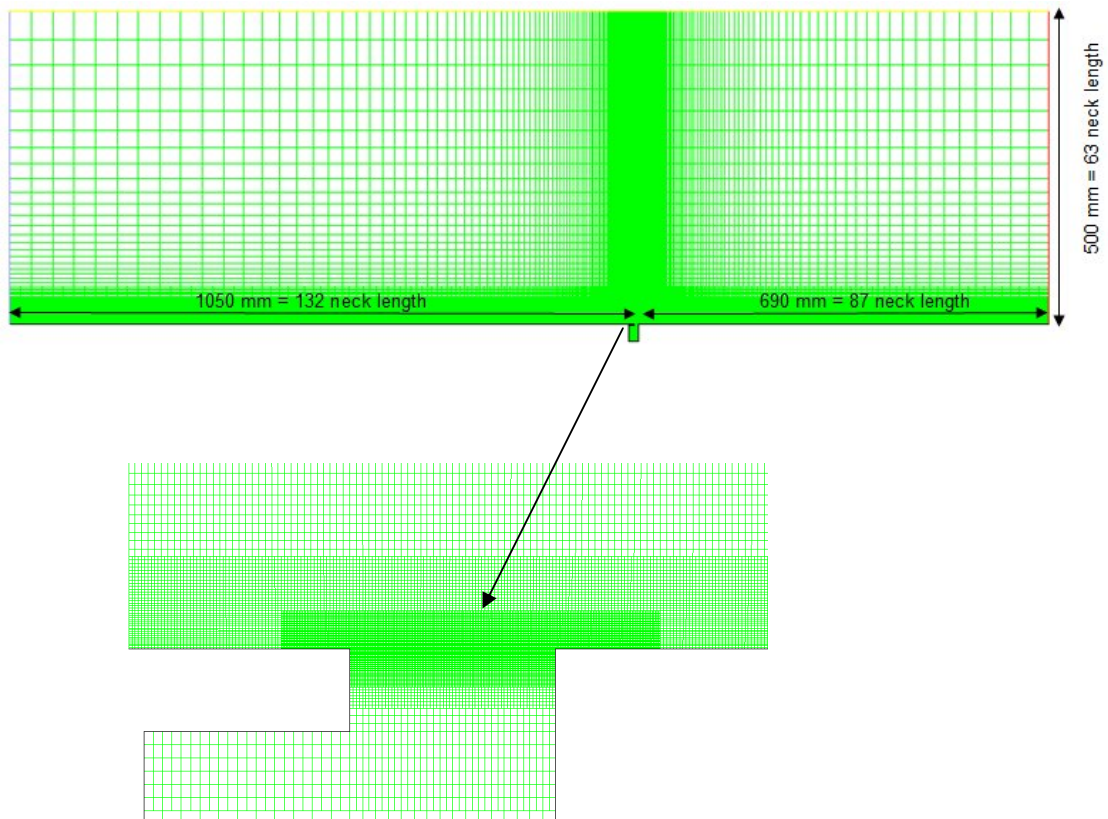
Figure 5-3 Detail of the computational Grid.

The main settings used for this simulation are listed below:

- Pressure Based Coupled Double Precision Solver

- II order implicit Unsteady formulation

- Discretization Scheme: Standard Pressure, III order QUICK for all the other convective terms

- Viscous Model: k-ω SST, transitional flow

- Green Gauss Node Based gradient discretization

- The time-step used is 1e-05 s (0.00048 s is the time taken by a convected vortex to pass the neck cavity, assuming $V_{conv} \sim V_{inf}/3$, so this time-step corresponds to about 50 time-step sampling for the shed vortex to pass the cavity)

5.1.3   Results

In Figure 5-4 it is shown that the Boundary Layer computed at the leading edge of the cavity (based on mean_x_velocity) is 16mm which is very close to the experimental measurement of 17mm.
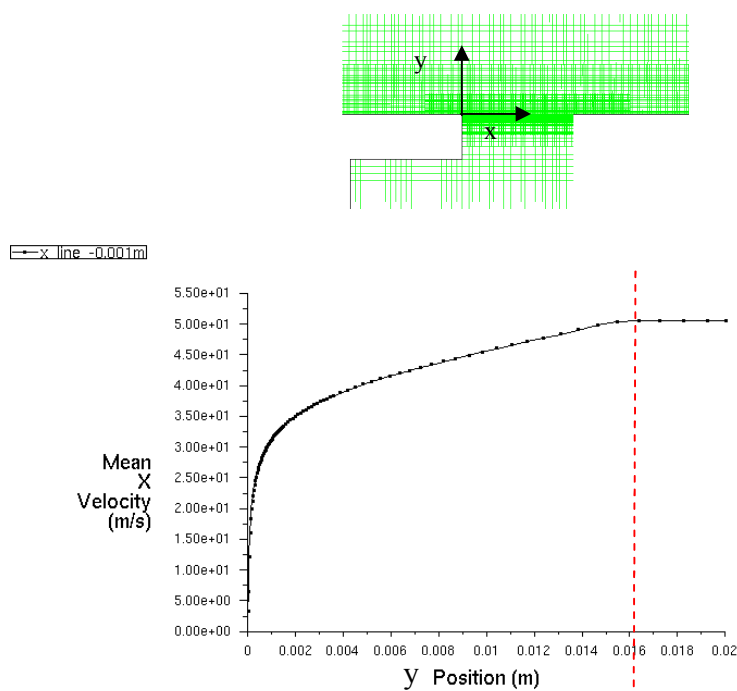
Figure 5-4 Computed Boundary Layer at the leading edge of the cavity.

To achieve the required boundary layer height, the length of the domain upstream of the cavity leading edge in the x direction was calculated according to the formula for Flat Plate Turbulent Boundary Layer development. Figure 5-5 shows a graph of boundary layer thickness development with distance. This illustrates that an upstream domain of length 1050 mm was required to achieve a boundary layer height of 17 mm.
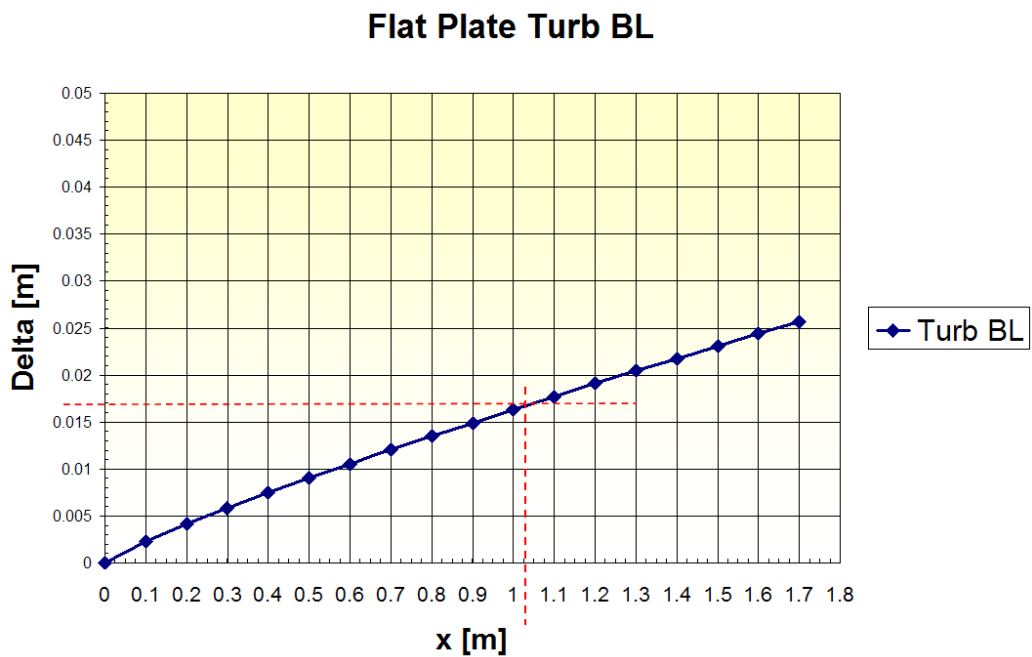
Flat Plate Turb BL

Figure 5-5 **Flat Plate Turbulent Boundary Layer Thickness (δ) development.**

In Figure 5-6 the results in term of the dB peak level of the fundamental tone and the according frequency are shown. Microphone is placed inside the cavity. The exact location is not important as the wavelength of fundamental tone is larger then the cavity dimension and the whole cavity pulsate with almost uniform pressure).

	Experimental	Present Simulation
SPL Peak (dB)	118	137
Peak Frequency (Hz)	1624	1810

Figure 5-6 **Comparison of simulated vs. experimental data.**

The physics of the buffeting phenomenon is well captured as it will be shown shortly. The frequency is well predicted (the difference exp. vs. simulated is 186 Hz, 11% error), while we have an over prediction of the SPL of the fundamental peak. This may be expected as the cavity in the simulation is completely rigid which will not be true in the real world. Then we must notice that the frequency is more related to the correct prediction of the vortex dynamics in the cavity opening while the magnitude of the SPL depends strongly on the acoustic response of the cavity. We do not have experimental information about the acoustics of the cavity which would be necessary to tune the numerical model.

Figure 5-7 shows the numerical URANS results obtained by the Rocketdyne Propulsion & Power, The Boeing Company, using the CFD code TIDAL on the same benchmark problem, [36]. It can be seen that the error on the computation of the peak frequency is greater than the one obtained in the present work (the difference exp. vs. simulated is 243 Hz). Furthermore, the SPL in this case is under predicted.
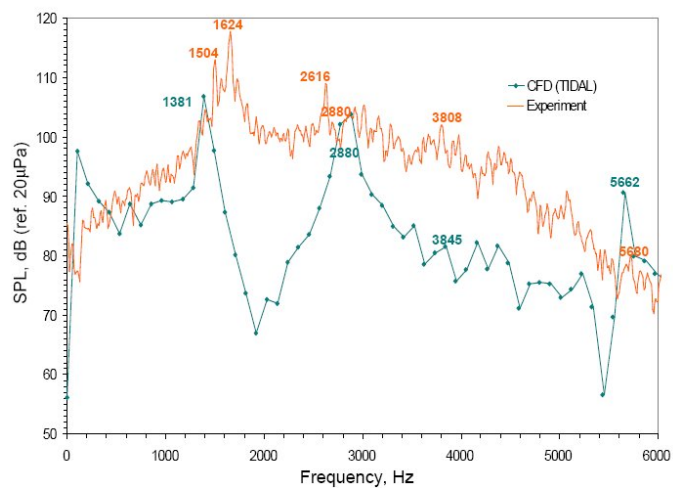
Figure 5-7 Comparison of the experimental data from the present benchmark (NASA/CP2004-212954) with the simulation performed with the CFD code TIDAL by Rocketdyne Propulsion & Power, The Boeing Company.

108
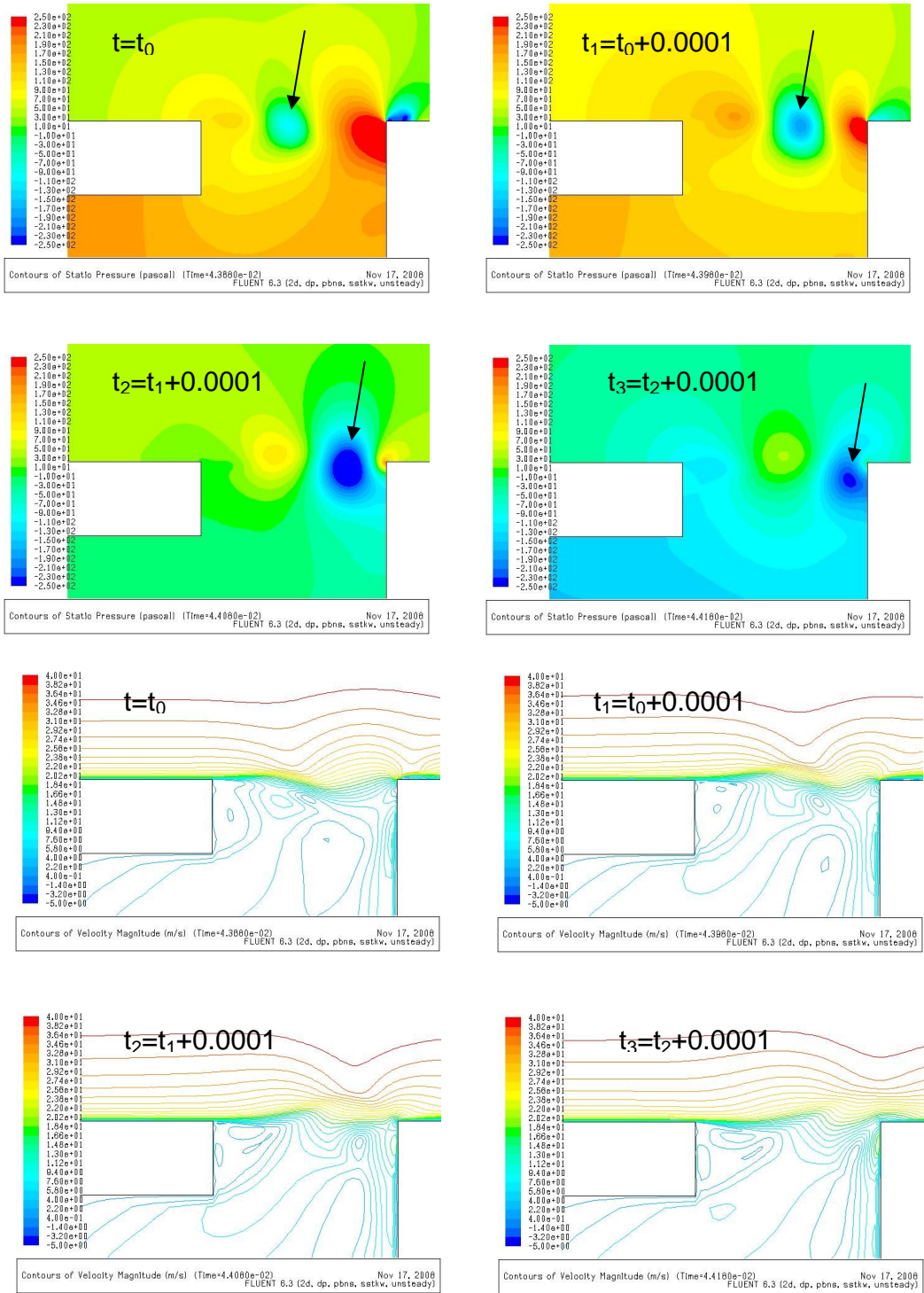
Figure 5-8 Detail of the flow field computed in the cavity: in the four upper pictures it is shown the pressure contour in the ones above the velocity-magnitude iso-line-values.

In the four upper pictures of Figure 5-8 it is clearly visible the convection of the vortices as they travel downstream (pressure contour). In the four above pictures the dynamics of the fluctuating shear layer can be seen in the iso-value-lines of the velocity-magnitude contours.

An analysis of the influence of the boundary layer thickness on the results was also performed. An other shorter domain was built, in order to obtain a reduction of the Boundary Layer height at the leading edge of the cavity, Figure 5-9. The simulation on the short domain was giving a Boundary Layer thickness of 12 mm.

Figure 5-9 The two domains used in order to obtain different BL thickness at the leading edge of the cavity (indicated with the arrow).

The simulation of the shorter domain with a smaller BL thickness gave an increase of the frequency of the fundamental peak when compared with the longer domain simulation (1930 Hz vs. 1810 Hz). This trend is in agreement with experimental test [36]. A smaller BL thickness creates higher convective velocity close to the cavity opening thus increasing the frequency of the fundamental peak, as the time taken by the vortices to cross the opening is shorter.

5.2   VORTEX SHEDDING NOISE

5.2.1   Experiments

To simulate vortex shedding noise it was decided to study the cylinder as it can represent a general bluff body and because lots of data are available about its unsteady aerodynamics and also some aeroacoustic ones.

The unsteady aerodynamics data considered here are from [11]: drag coefficient and Strouhal number are presented for a wide range of Reynolds number. These data give upper and lower bound curves as they were derived from a collection of data obtained from different experiments. This is very good because it is always desirable to have the experimental data dispersion when comparing to CFD simulation which is instead a very repeatable "virtual experiment" for a certain code and set up.

Acoustic data are available only for Reynolds number of 89,000 from [22]: they show the SPL measured by a microphone placed at a distance of 128 diameter at 90 degree to the flow direction. The diameter of the cylinder in this case is 19 mm.

5.2.2   Simulation Set Up

To investigate the unsteady aerodynamics and the noise produced by the cylinder, 2D and 3D grids were built. Simulations were carried our using both URANS and LES approaches with FLUENT 6.3.26. To investigate the sensitivity of aerodynamics towards Reynolds number, different 2D grids were designed in order to always have $y^+ < 1$ on the surface. Both grid refinement and time-step sensitivity were performed.

Because the Mach number is always about 0.2, non-compressible simulations for both URANS and LES simulations were performed. Figure 5-10 shows the 2D and 3D grid used for URANS simulations.
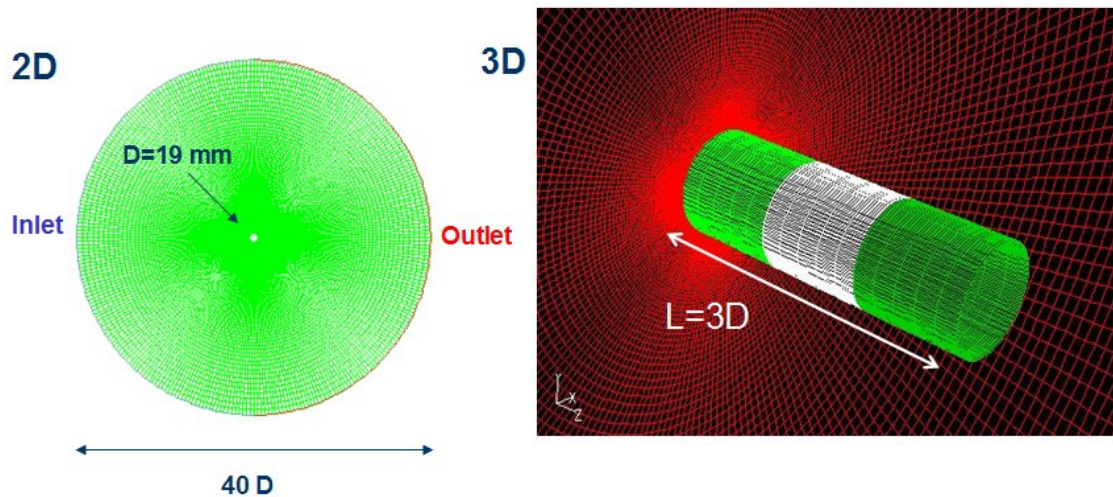
Figure 5-10 2D and 3D grid used for URANS simulations.

In this case the noise has been computed using the FW-H Acoustic Analogy which is well suited because the microphone is located at a large distance and the noise sources are all dipoles distributed on the surface of the cylinder. Furthermore there are no obstacles between the sources and the receiver and, because the simulation is basically incompressible, there is no coupling between the acoustics and the aerodynamics.

The 2D grids tested are listed below:

- Grid1 – 50x100 nodes ($\cong$ 9000 cells)

- Grid2 (*default*) – 100x200 nodes ($\cong$ 39000 cells)

- Grid3 – 150x300 nodes($\cong$ 89000 cells)

- for Re <10e5   *ds*_at_wall=0.00005 D

- for Re >10e5   *ds*_at_wall=0.000005 D

The 3D grid used for URANS simulation was the Grid2 extruded in the z direction for a length of 3 diameters and divided in 15 planes along the span, for a total of about 600,000 hexahedral-cells.

To build up the grid for a LES simulation a more detailed investigation was necessary. In a near wall resolving LES approach, the general guidelines that can be found in literature require:

$$y^+ < 1, \qquad \Delta x^+ \cong 50, \ \Delta z^+ \cong 15$$

where these non dimensional coordinates are defined as (i.e. for y coordinate):

$$y^+ = \frac{u_* y}{\upsilon}$$

(5.1)

Where $u_* = (\tau_w/\rho)^{1/2}$ is the so called friction velocity which can be derived from dimensional analysis, τ_w is the wall shear stress, ρ is the local density of the fluid and υ is the local kinematic viscosity.

As noticed by others, a minimum of three grid points have to be placed in the zone $y^+ < 10$ to obtain a good representation of the inner sub-layer.

In the Figure 5-11 a summary is shown of the physical sizes that must be respected to obtain a good resolved LES grid near the wall for the cylinder test case. From this it is evident that a full 3D LES simulation for Reynolds number of 89,000 was not affordable with the HW resources available in 2007 (dual-core PC).

Reference length (m)	Re (x10^6)	Non dimensional length	Dimensional length (m)
0.019	0.089	$y^+ < 1$	$y < 0.0000039$
0.019	0.089	$\Delta x^+ \cong 50$	$\Delta x \cong 0.0001963$
0.019	0.089	$\Delta z^+ \cong 15$	$\Delta z \cong 0.0000588$
0.019	0.089	$y^+ < 10$	$y < 0.0000392$
0.019	0.001	$y^+ < 1$	$y < 0.0001899$
0.019	0.001	$\Delta x^+ \cong 50$	$\Delta x \cong 0.0095$
0.019	0.001	$\Delta z^+ \cong 15$	$\Delta z \cong 0.00285$
1.045	4.9	$y^+ < 1$	$y < 0.0000032$
1.045	4.9	$\Delta x^+ \cong 50$	$\Delta x \cong 0.0001625$
1.045	4.9	$\Delta z^+ \cong 15$	$\Delta z \cong 0.0000487$

Figure 5-11 Grid size specifications required near the wall for a well resolved LES.

The above recommendations for the sizing of the LES grid are valid in the near wall region, indeed far from the wall it is possible to check if the grid is adequate or not by analyzing the turbulent length scale. This can be done by post-processing a much computationally cheaper URANS or RANS simulation. It must be pointed out that this method is not rigorous but can give some useful indications at a low computational effort. The size of the grid for a LES simulation in a free high Reynolds turbulent flow should be smaller than $l_0/6$ where l_0 is the integral length scale. This comes from Kolmogorov's theory of turbulence.

Kolmogorov argued that the directional biases of the large scales are lost in the chaotic scale-reduction process as energy is transferred to successively smaller eddies. Hence Kolmogorov's hypothesis of local isotropy states that *at sufficiently high Reynolds numbers, the small-scale turbulent motions (l<<l$_0$) are statistically isotropic.* Here, the term local isotropy means isotropy at small scales. Large scale turbulence may still be anisotropic [10].

In Figure 5-12 l_{EI} is the length scale that forms the demarcation between the large scale anisotropic eddies ($l>l_{EI}$) and the small scale isotropic eddies ($l<l_{EI}$). For many high Reynolds number flows l_{EI} can be estimated as $l_{EI} \approx l_0/6$.
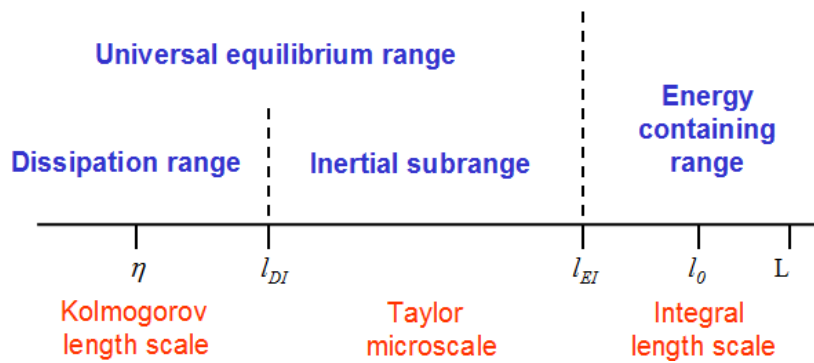
Figure 5-12 Kolmogorov scales, eddy sizes.

Hence because LES is based on subgrid scale models which model isotropic eddies, the LES grid size should be smaller than $l_0/6$. An estimation of l_0 can be obtained by a RANS simulation considering that $l_0 \sim k^{1.5}/\varepsilon$.

The timestep should be small enough to have the courant-cell number <1.5, thus it is also dependent on the Reynolds number.

For URANS the timestep size was taken as a function of Strouhal number, having at least 100-200 time-steps per cycle [11].

The main settings used for the simulations are listed below:

- Pressure Based Double Precision Solver

- II order implicit Unsteady formulation

- Non Iterative Time Advancement Scheme (for 3D URANS Iterative Time Advancement and coupled pressure-velocity indeed)

- Discretization Scheme: PRESTO Pressure, II order upwind for all the other convective terms

- Viscous Model: k-ω SST, transitional flow for URANS, Smagorinsky-Lilly for LES

- Green Gauss Celle Based gradient discretization

5.2.3   Results

Figure 5-13 shows the grid sensitivity study to the Strouhal number for 2D URANS simulation at Reynolds 1000. Grid2 was chosen as a good compromise between accuracy and computational cost, considering that for Re <10e5 the height of the first cell at the wall was *ds*_at_wall=0.00005D, and for Re >10e5 *ds*_at_wall=0.000005D, to have always y$^+$ < 1.
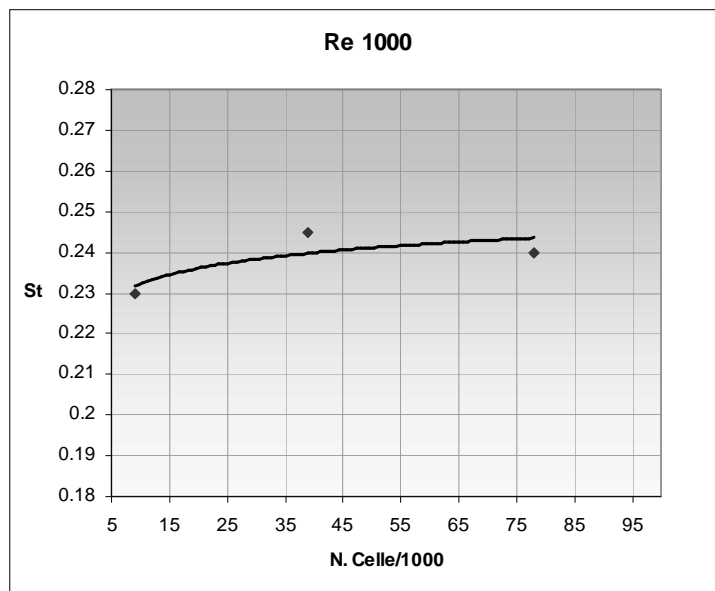
Figure 5-13 Grid sensitivity study to the Strouhal number for 2D cylinder.

Figure 5-14 shows the time-step sensitivity study to the Strouhal number for 2D URANS simulation at Re = 1000.
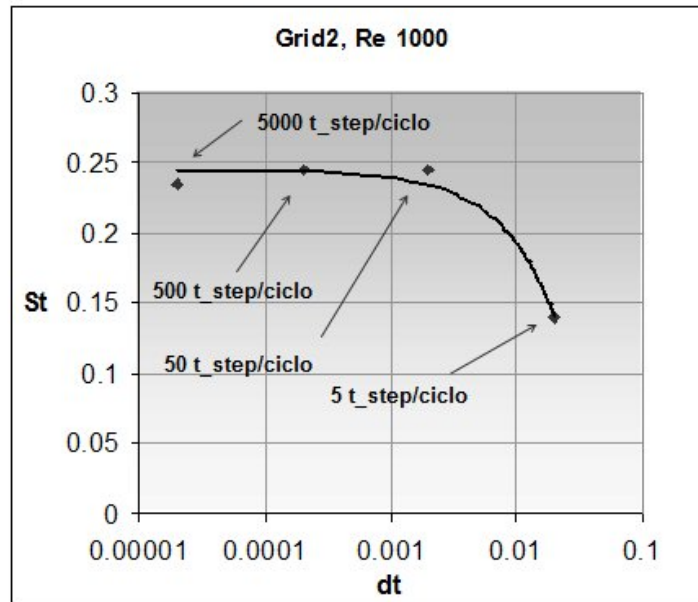
Figure 5-14 Time-step sensitivity study to the Strouhal number for 2D cylinder.

It can be seen that 100 timestep per cycle is sufficient to obtain an accurate solution.

In Figure 5-15 all the URANS simulations are presented in terms of drag coefficient and Strouhal number; they are compared with experimental data and with the simulations performed by Rumsey and Brenter from NASA Langley Research Centre, [11].
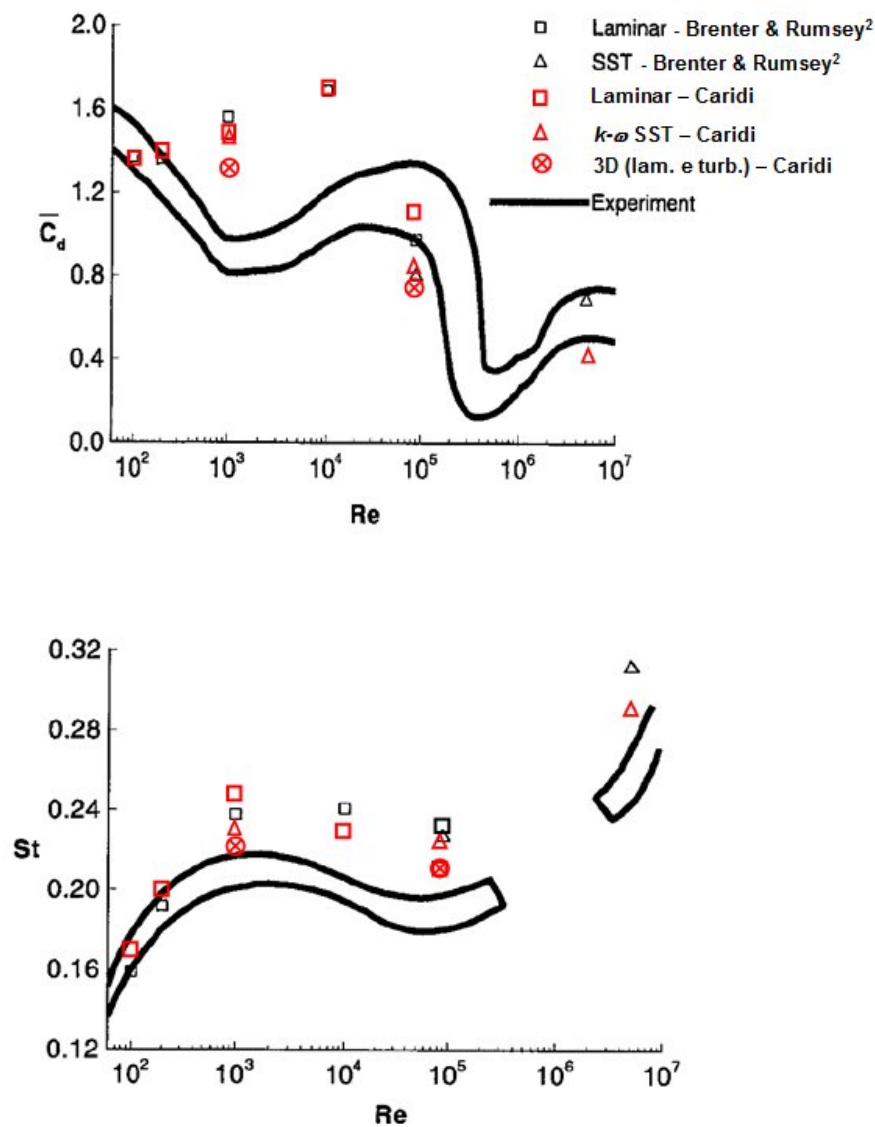
Figure 5-15 Comparison of URANS predicted *Cd* and *St* with experiment.

It can be seen that the results obtained in the present work are very close to the ones obtained by Rumsey and Brenter. At Re < 10,000 3D effects are important and this leads to an over prediction for the 2D simulations of the drag coefficient as well as of the Strouhal number. In fact the 3D laminar simulation follows the experimental trends more closely and thus gives a better prediction at Re=1000. For Re < 200 the behaviour of the

flow is almost 2D and the 2D simulations compare much better with experiments. Re = 89,000 is a very sensitive Reynolds number as it is close to the transition from the *subcritical* to the *supercritical* regime. In this case we found out that the simulation is very sensitive to the variation of the turbulence of the flow at the far field (i.e. inlet turbulence boundary condition), [45]. It can be seen that the overall trends are well captured.
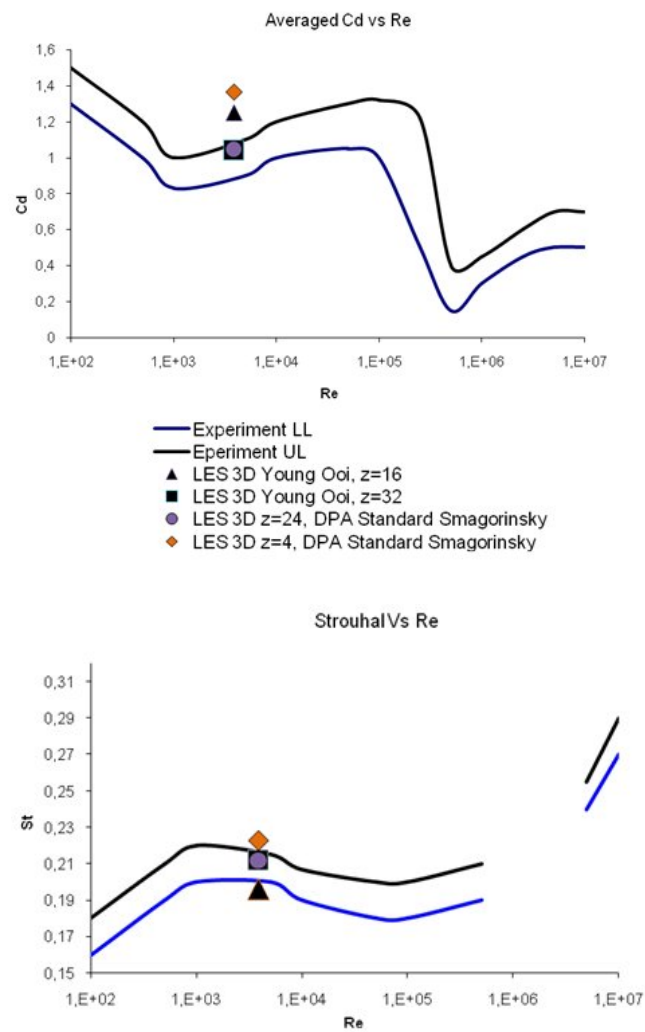
Figure 5-16 Comparison of LES predicted *Cd* and *St* with experiment.

In Figure 5-16 LES simulation results are reported at Re = 3,900. Two cases were run with 4 and 24 planes along the span (referred to as DPA in the Figure). Also results from Young Ooi [45] are reported for comparison. It is evident that 4 planes are insufficient and the drag and Strouhal number obtained are very close to 2D results. While with 24 planes the agreement with experimental data is very good and much better than the one obtained with URANS at similar Reynolds number.
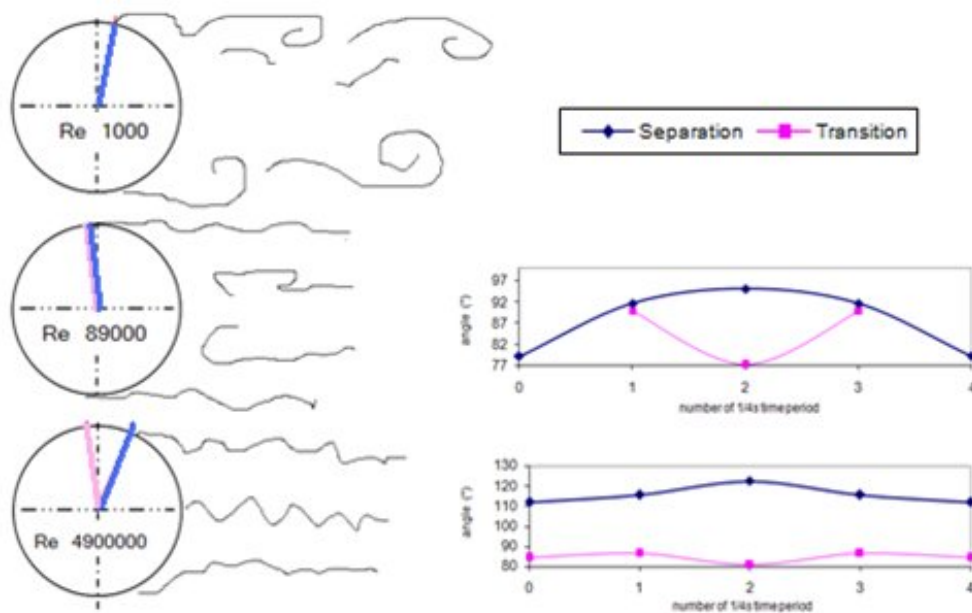
Figure 5-17 Computed separation and transition over 2D cylinder by URANS simulation.

A study was performed to investigate the transition and the separation point for the different flow regimes, i.e. at different Reynolds numbers. Because the separation and transition are both unsteady phenomena, an average value for their position was computed. Results for URANS are reported in Figure 5-17. This behavior is in agreement with experimental evidence.

In the following Figure 5-18 the comparison between the computed and experimental flow field is shown.
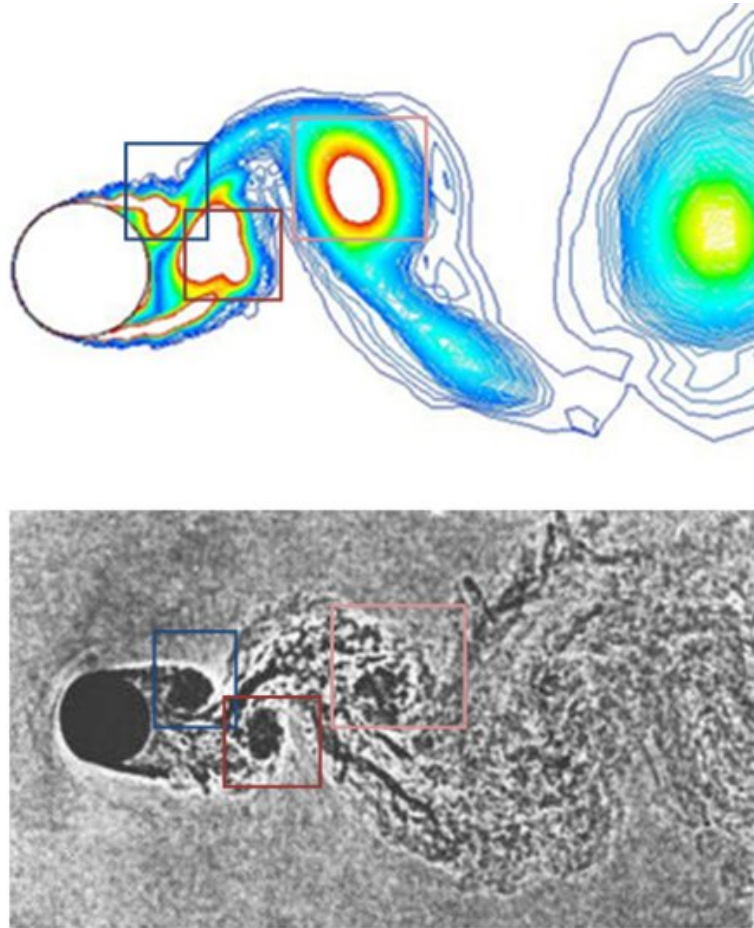
Figure 5-18 URANS flow field comparison.

The noise at a microphone placed at 128 diameters and at 90 degrees to the flow direction was computed using the FW-H Acoustic Analogy. For 2D simulation a correlation length must be specified as the contribution to the noise comes from all the 2D sections that makes up the real cylinder which is 3D, see Figure 5-19. Experimental testing shows that the vortices are correlated, that is they fluctuate at the same frequency, for a length that ranges from about 5 to 10 diameters.
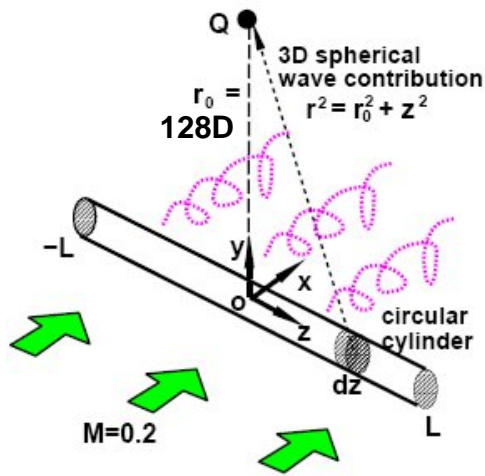
Figure 5-19 Concept of correlation length.

A sensitivity analysis to the correlation length was performed and is reported in the next Figure 5-20.
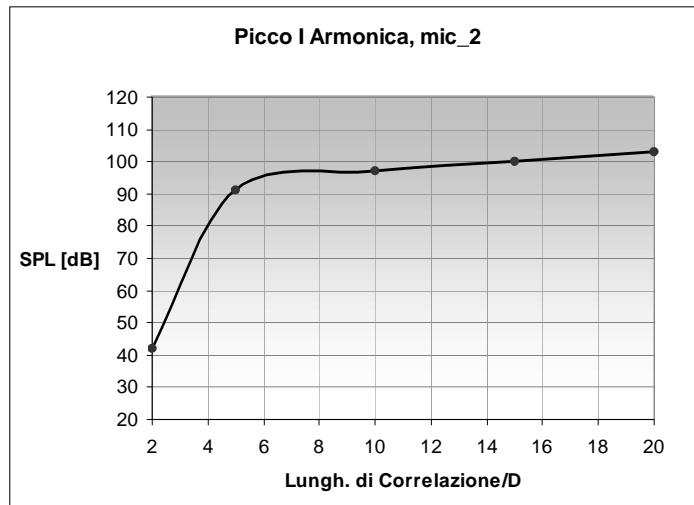
Figure 5-20 Correlation length sensitivity study.

It shows that the big change in the SPL occurs between 2 and 6 diameter length. For the 2D computation a correlation length of 10 diameters was used as suggested in [11].

The SPL spectrum for the 2D URANS computation is reported in Figure 5-21. It can be seen that the peak level is well captured, but noise coming from other frequencies is missing. This is due to the RANS model used which is incapable of describing all of the turbulence scales. The smallest scales are generally damped out and this can explain some lack of agreement for higher Strouhal numbers. We must also consider that 2D simulations force the behaviour of the fluid to be much more ordered as there is no third dimension which can create instabilities and can add other noise frequencies. The shift in the Strouhal number is the same reported in the aerodynamic computations, see Figure 5-15. It must be considered that the experimental data from Revell et al. shows a Strouhal number of 0.17 which is the lower limit for the data at Reynolds 89,000 of Figure 5-5.
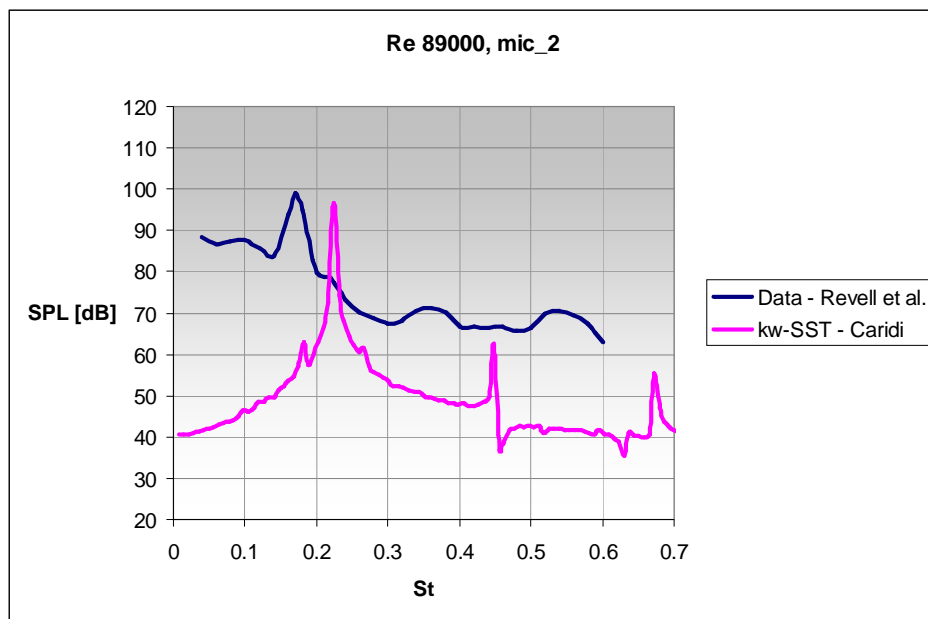
Figure 5-21 Comparison of predicted and measured sound pressure level, FLUENT 2D URANS simulation.

The results obtained are quite similar to the ones obtained by Rumsey and Brenter [11], which are shown in Figure 5-22. In this figure the different turbulent models are also compared.
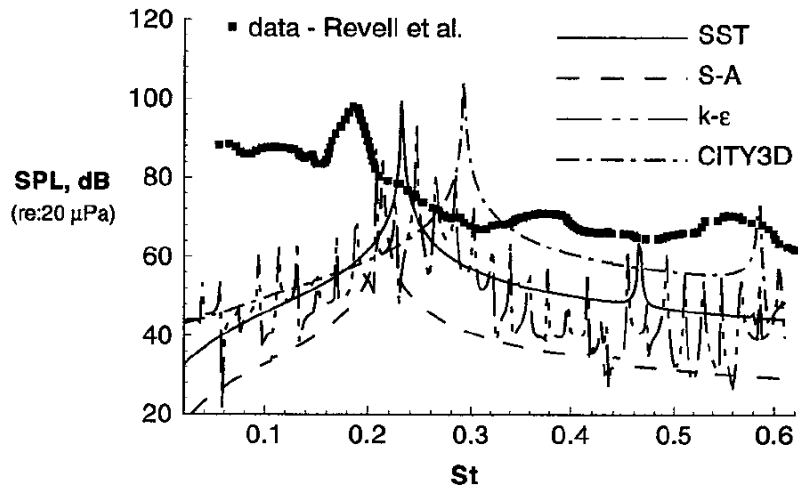
Figure 5-22 Comparison of measured and predicted sound pressure level by Rumsey and Brenter, [11].

5.3   PROPELLER NOISE

Two main propellers were chosen for simulating propeller noise:

- NASA SR2

- NACA 4-(3)(08)-03

The choice was made because of the availability of aerodynamics, aeroacoustics and geometry data. Before proceeding with aeroacoustic computations it was thought to be necessary to calculate the loading on the propellers and to compare it with experimental data. In fact if the blade loading is incorrectly predicted the computed noise will also be erroneous.

5.3.1   Experiments

In the following sections the details of the experimental testing for the NASA SR2 and NACA 4-(3)(08)-03 are reported.

5.3.1.1   NASA SR2

Aerodynamic test data for NASA SR2 propeller were taken from the NASA TM-87054 report [28]. In this case a low speed wind tunnel performance test was completed at the NASA Lewis Research Center as part of the NASA Advanced Turboprop Program (1975-1985). The 62.2 cm (24.5 in) diameter 8 blade adjustable pitch model was tested at Mach numbers typical of takeoff, initial climb out, and landing speeds (i.e. from 0.10 t o 0.34) in the NASA Lewis 10- by 10-Foot Supersonic Wind Tunnel. The attractiveness of advanced turboprop propulsion results from its potential for very high propulsive efficiency at cruise speeds up to Mach 0.8.

In Figure 5-23 the design parameters curves that were used to build up the CAD model of the NASA SR2 are shown. The propeller configuration chosen was that with 41.7 degree blade angle at 75% of the radius (β_{ref} =41.7 deg) for simulation at M=0.1 and 59.7 degree blade angle at M=0.34.
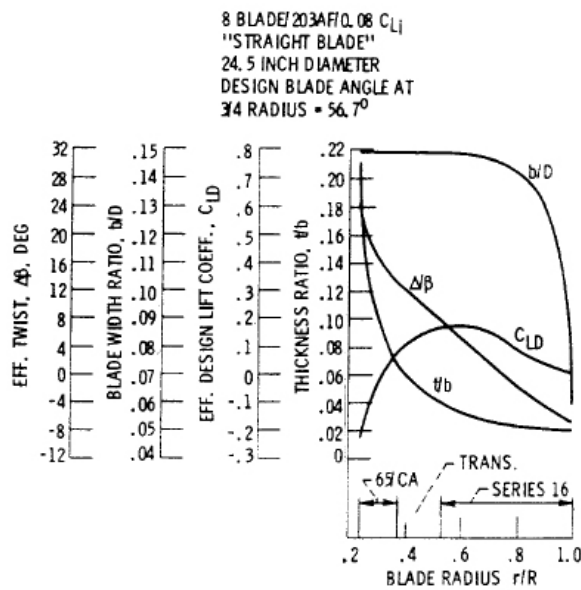
Figure 5-23 Variation of propeller design parameters with blade radius for the unswept SR-2 propeller.

Figure 5-24 shows the test facility and it can be seen that the propeller is mounted on a spinner. No information was given about the propeller geometry in the report but it was possible to design it by a careful analysis of some pictures.

Figure 5-25 shows the CAD model of the NASA SR2 with the spinner that was considered axisymmetric in order to apply the periodic condition in the CFD simulation.

126
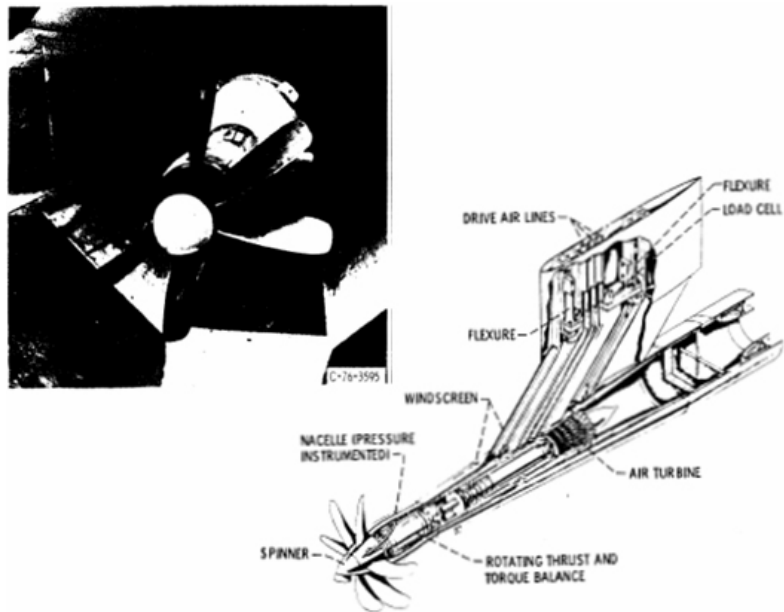
Figure 5-24 Test facility: close up of the propeller and a cutaway view of the strut-mounted Lewis propeller test rig.
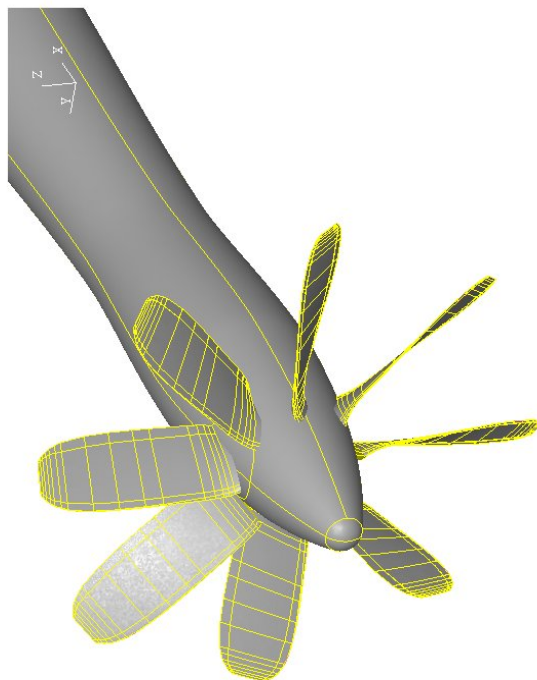
Figure 5-25 CAD of the NASA SR2 propeller with the spinner.

127

The aerodynamics experimental data are shown in Figure 5-26 and 5-27, for M=0.1 and M=0.34.

To understand these maps the following formulas are reported:

- Advanced Ratio $\qquad J_{REF} = \dfrac{V_0}{nD}$

- Trust Coefficient $\qquad C_T = \dfrac{T}{\rho_0 n^2 D^4}$

- Power Coefficient $\qquad C_P = \dfrac{P}{\rho_0 n^3 D^5}$

- Efficiency $\qquad \eta_{net} = \dfrac{TV_0}{P} = J\dfrac{C_T}{C_P}$
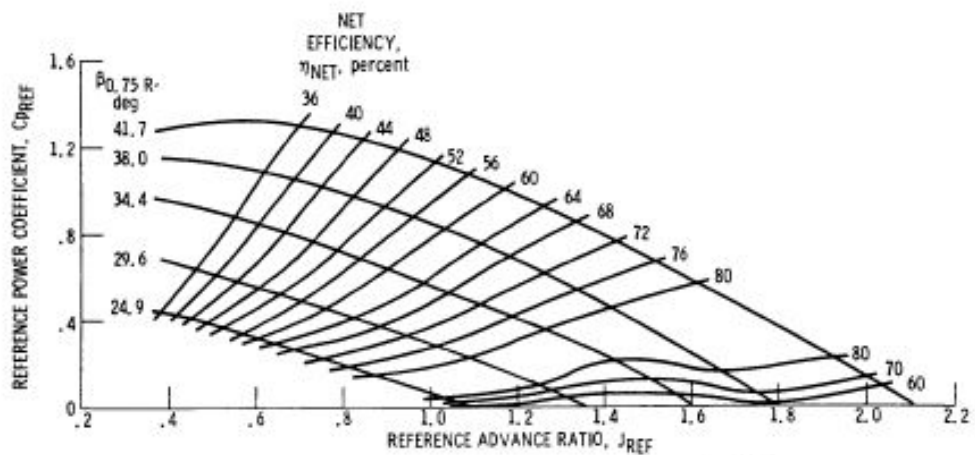
Figure 5-26 SR-2 propeller efficiency map at a Mach number of 0.10.
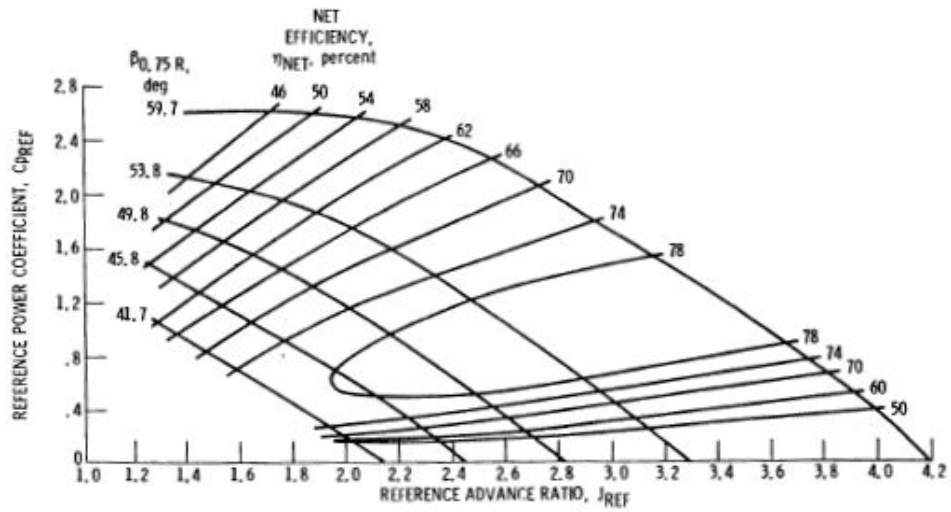
Figure 5-27 SR-2 propeller efficiency map at a Mach number of 0.34.

Noise data on the SR-2 model propeller were taken in the NASA Lewis Research
Center using a 8- by 6-Foot Wind Tunnel, [31]. The propeller was tested at a fixed blade
setting angle of 59 degrees for all the various tunnel axial Mach numbers. Data are
available for M = 0.6, 0.65, 0.7, 0.75, 0.8, 0.85, 0.9. A schematic diagram of the
experimental facility with the transducers is shown in Figure 5-28.
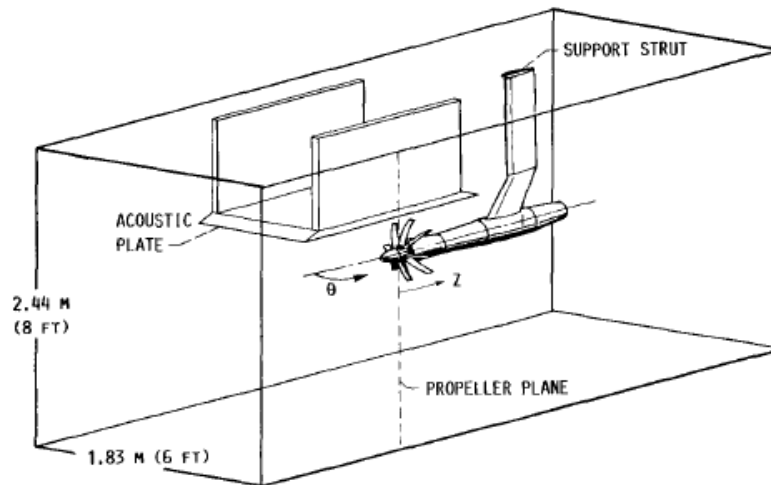
TRANSDUCER (PLATE 0.3 DIAMETER FROM TIP)											
1	2	3	4	5	6	7	8	9	10	11	12
TRANSDUCER DISTANCE FROM PROPELLER PLANE, Z, CM (IN.)											
-46.7 (-18.4)	-41.7 (-16.4)	-30.5 (-12.0)	-16.0 (-6.3)	-8.9 (-3.5)	0.8 (0.3)	8.9 (3.5)	12.4 (4.9)	18.0 (7.1)	25.0 (9.9)	28.7 (11.3)	42.4 (16.7)
ANGLE FROM UPSTREAM, θ, DEG											
46.8	50.0	58.5	72.2	80	90.9	100	104	110	116.8	120	130.4

(b) TRANSDUCER LOCATIONS.

Figure 5-28 Experimental facility for noise measurements of SR2 propeller at Lewis Research Center Cleveland, Ohio.

5.3.1.2   NACA 4-(3)(08)-03

Tests for the aerodynamic characteristics of the NACA 4-(3)(08)-03 two-blade propellers were conducted in the Langley 8-foot high-speed tunnel for blade angles between 40° and 65° and through a Mach number range up to 0.925, [25]. In the present work the configuration with the blade angle at 55° and M=0.45 was considered. The facility is shown in Figure 5-29 while the aerodynamic experimental data are reported in Figure 5-30.
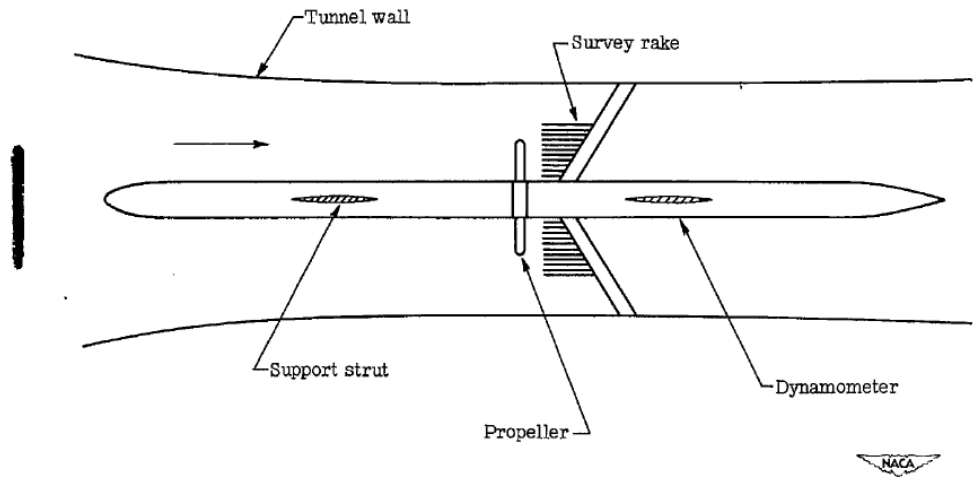
Figure 5-29 Test apparatus for aerodynamic force measurements.

Noise data were not available for the test condition of M=0.45, but it was considered useful to validate the numerical model for the prediction of aerodynamic loading before proceeding to acoustics computations.
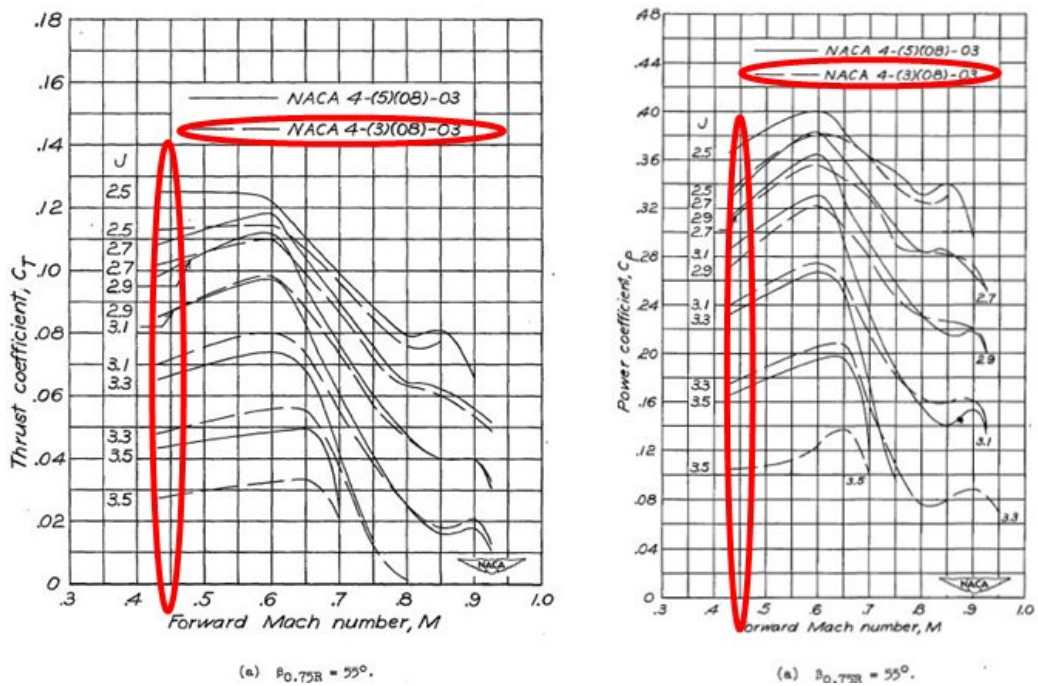
Figure 5-30 Thrust and Power Coefficient for NACA 4-(3)(08)-03, 55° blade angle.

Aeroacoustics data for the two, four and seven blade NACA 4-(3)(08)-03 propeller are available in the report NACA-TN-1354, [26], In this case the measurements were made in an open field and the flow stream velocity is 0. The propeller has a diameter of 4 feet. A 200-horsepower variable-speed electric motor was used to drive the test propellers. The motor was rigidly mounted on an outdoor test stand, Figure 5-31.

Figure 5-31 Seven blade NACA 4-(3)(08)-03 propeller mounted on test stand.

A microphone was placed at ground level to ensure maximum pick-up of all frequencies and was located at a point 30 feet from the propeller hub and at 15° angle behind the plane of rotation, β =105° (where β is the angle from propeller axis of rotation, 0 in front). This particular angular position was chosen because it is near the value of β for maximum sound pressures for the range of sound harmonics measured.

A survey of rakes to measure total pressure was clamped to the motor housing at approximately 4 inches behind the propeller. The measured total pressure was integrated over the disk area to obtain an estimate of total thrust. These measurements are believed to be sufficiently accurate (± 25 %) for sound calculations. This error in thrust represents approximately 1 decibel error in sound intensity.

Sound pressures and frequencies were measured with a Western Electric moving-coil pressure-type microphone and a Hewlitt Packard Wave Analyzer. Data were obtained at tip Mach numbers of 0.3, 0.5, 0.7 and 0.9. Gusts of wind cause a violent fluctuation in sound pressures for all frequencies of the emitted noise. Measurements on the seven-blade propeller at a 20° blade angle, taken on a day when gusts were approximately 20 miles per hour, showed sound pressure variations of approximately 15 decibels at all speeds of the propeller. In order to obtain consistent data, testes were run only on days when the wind velocities were low.

5.3.2 Simulation Set Up

Before simulating NASA SR2 and NACA 4-(3)(08)-03 propeller a thorough investigation was carried out regarding the methods available in the FLUENT software for the simulation of rotors [44]. In order to do this a simple rotor test was designed and the fluid domain was generated with a tetrahedral mesh, Figure 5-32. This test case was to define some methodologies for improving the iterative convergence and reducing the CPU time of the simulation.
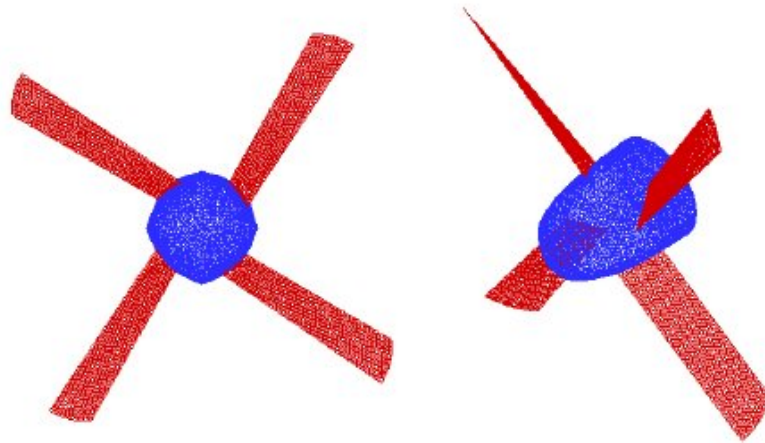
Figure 5-32 Rotor test for investigating the rotating object models.

The following studies were carried out:

- Moving Reference Frame (MRF) vs. Sliding Mesh (SLM) approach

- Periodic Boundary Condition testing

- Convergence analysis

- CPU time reduction

After these studies, it was clear that SLM model is much more expensive as it requires transient simulation. Furthermore, in order to achieve the same results of MRF very small time-steps and/or many sub-iterations are necessary. But if we are interested in the evaluation of average value of the loading, the MRF model can represent a cheaper alternative to the more expensive SLM, with about the same accuracy. The Periodic Boundary Condition implemented in FLUENT works very well and can be utilised to significantly reduce the dimension of the computational domain. For both MRF and SLM models gradually increasing the rotational speed with a first order accurate solution was found to be the best approach to reduce the computation time and avoid as possible convergence problems.
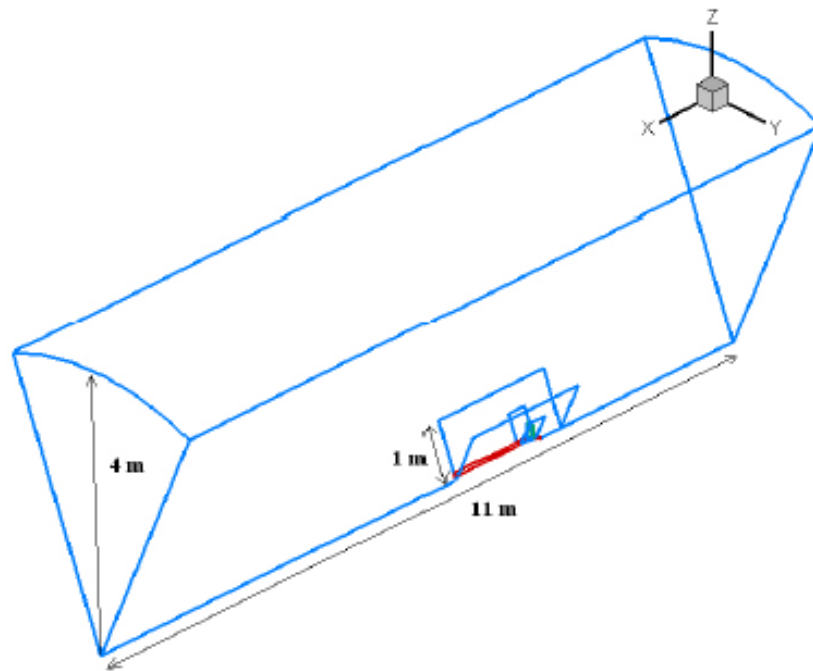
Figure 5-33 Periodic domain for NASA SR2 propeller.

The periodic domain designed for NASA SR2 propeller is shown in Figure 5-33.

Two grids for SR2 model were generated with TGRID and tested:

- 2.2 million hybrid grid (5 prism layers + tetrahedral cells)

- 1.7 million polyhedral grid (generated from the hybrid one)

Some details of the grid are shown in Figure 5-34 and 5-35.
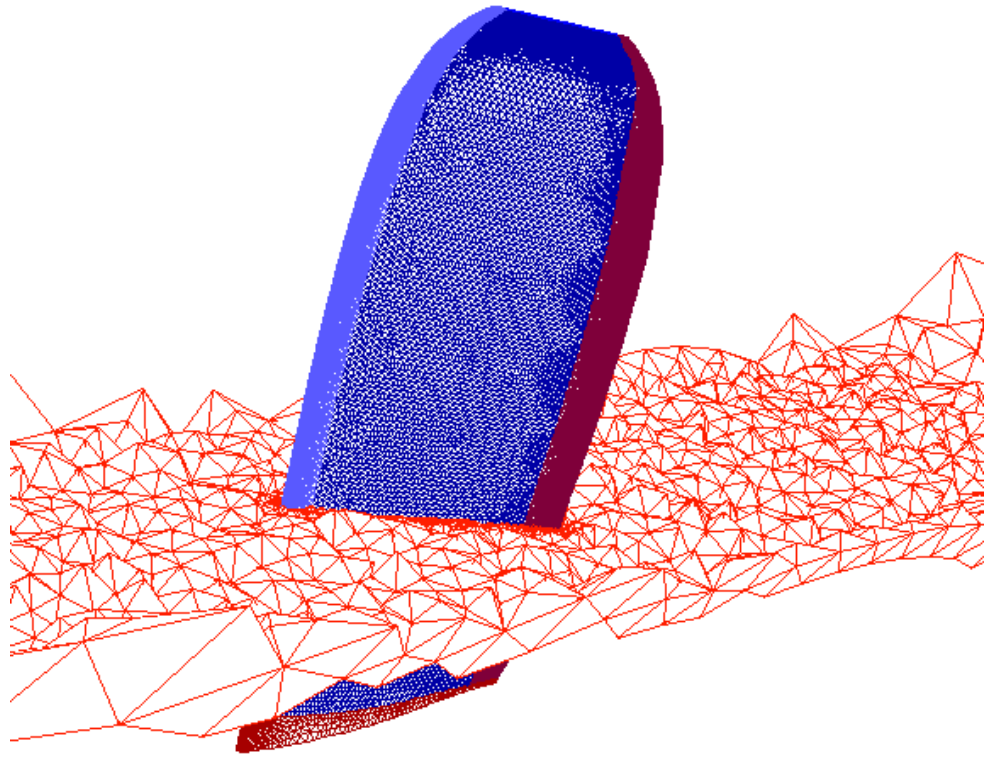
Figure 5-34 Surface and hybrid volume grid for SR2 propeller.
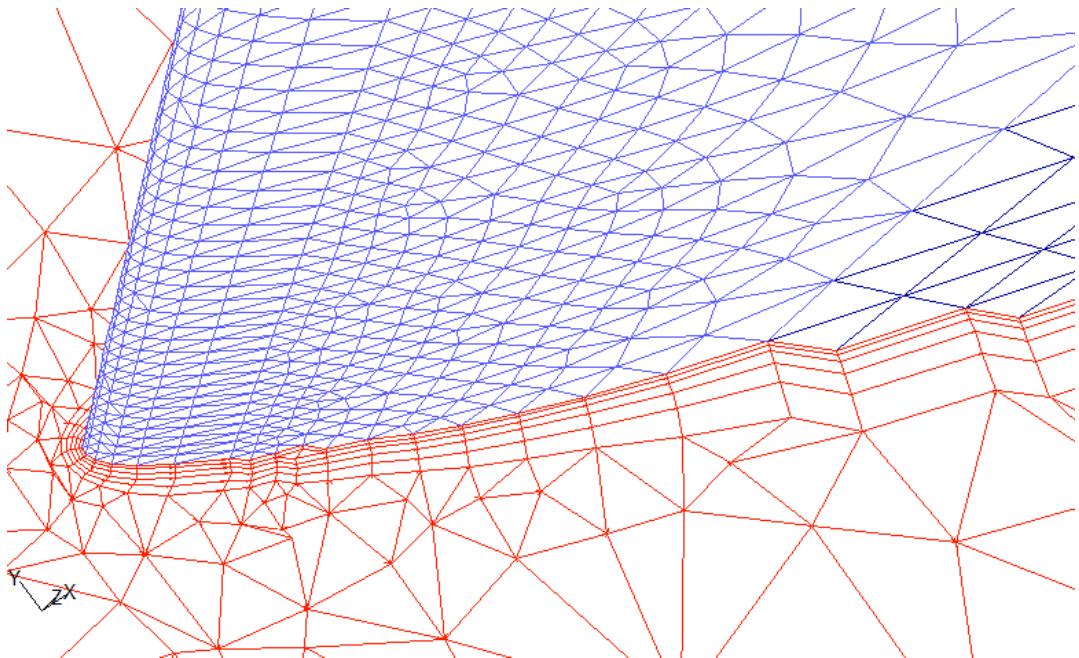
Figure 5-35 Detail of the 5 prism layers. Notice that the growth of the prism layers is taking into account the curvature of the airfoil section.

The quality of the volume grid obtained was good with a maximum skewness of 0.85. Attention was paid to create a regular surface and volume mesh. The mesh generation was automated by writing some scripts for TGRID. Hence, it was possible to quickly change grid parameters, such as the growth rate of prism or volume mesh, numbers of prism layers, constraints on orthogonality of prism layers to generate a number of different grids. The best quality grid could then be chosen for CFD simulations. In Figure 5-36 it is possible to see the surface polyhedral mesh generated as conversion of the tetrahedral one.
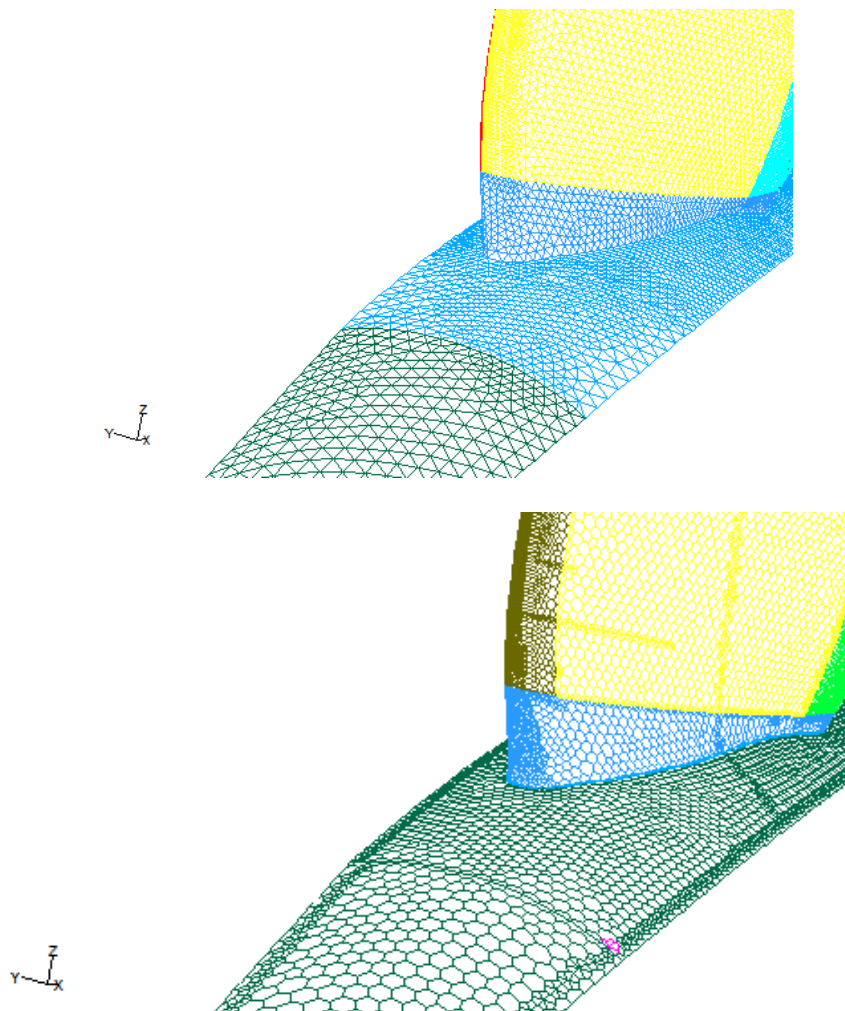
Figure 5-36 Comparison of the surface mesh for tetrahedral and polyhedral grid.

For the NACA 4-(3)(08)-03 three domains were created, two similar to the SR2 (for 2 and 7 blade propeller), and one that was reproducing the experimental apparatus used for aeroacoustic measurements, see Figures 5-37 and 5-38.
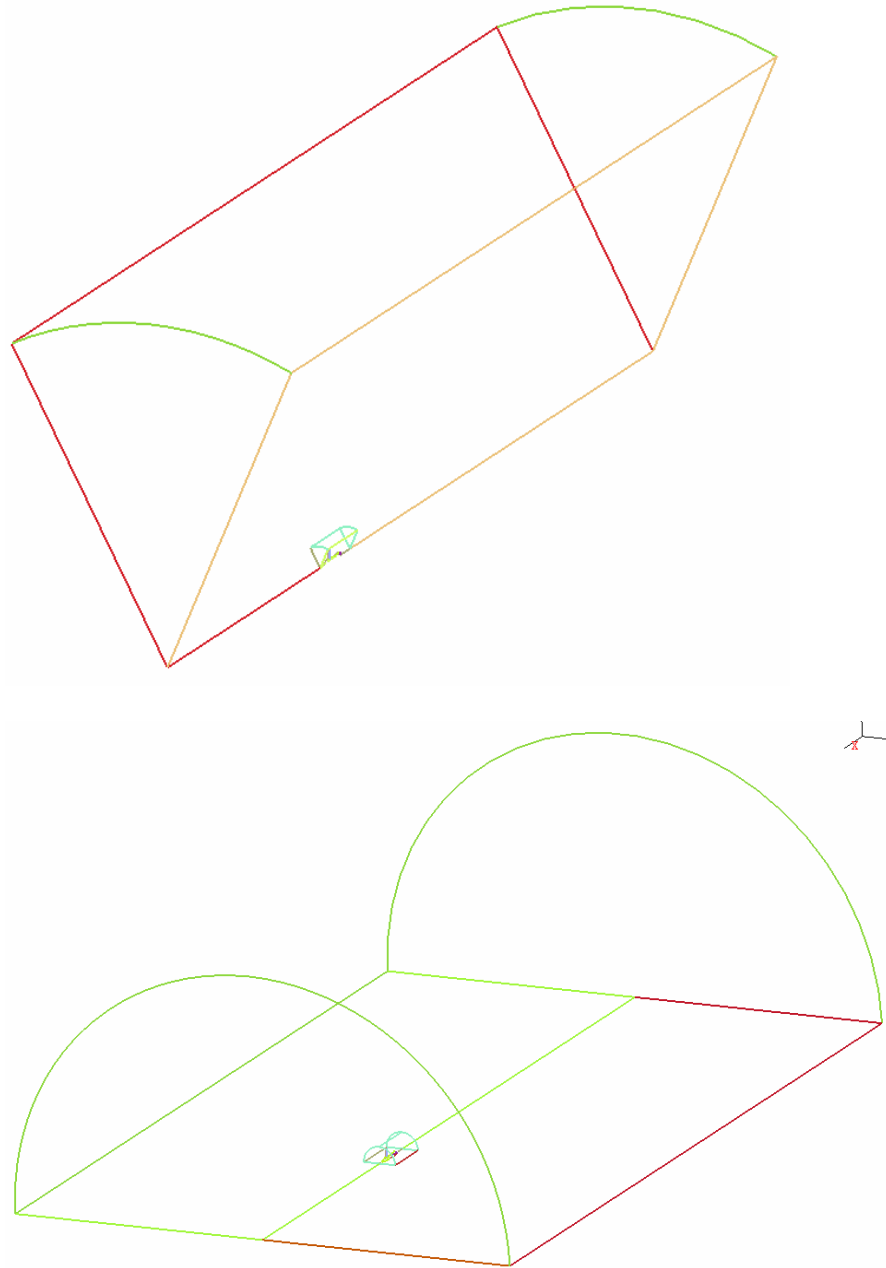
Figure 5-37 Computational domain for 7 and 2 blade NACA 4-(3)(08)-03 propeller.
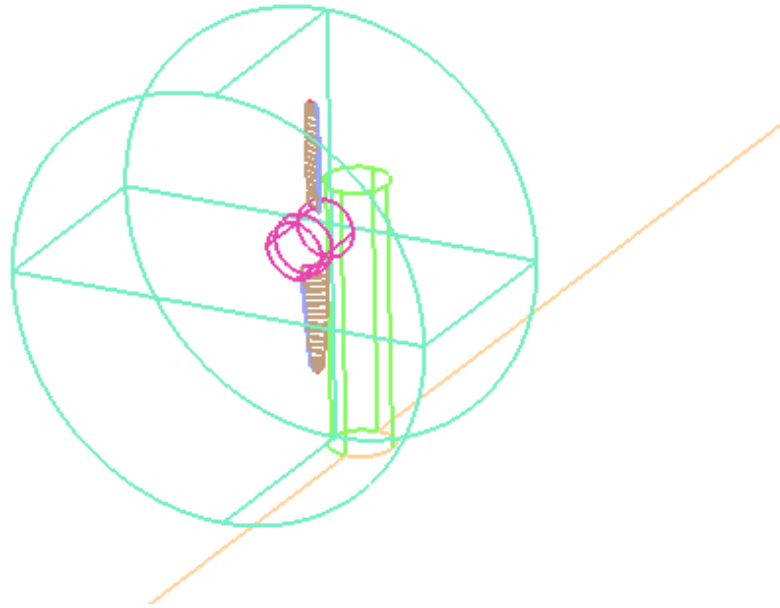
Figure 5-38 Computational domain for 2 blade NACA 4-(3)(08)-03 propeller reproducing the experimental apparatus for aeroacoustic measurements.

Figure 5-38 shows the detail of the domain realized to reproduce the experimental test facility used for the aeroacoustic test. It can be noticed the fluid volume surrounding the propeller that will be used as rotational domain for Sliding Mesh simulation. The ground was also modelled in this case.
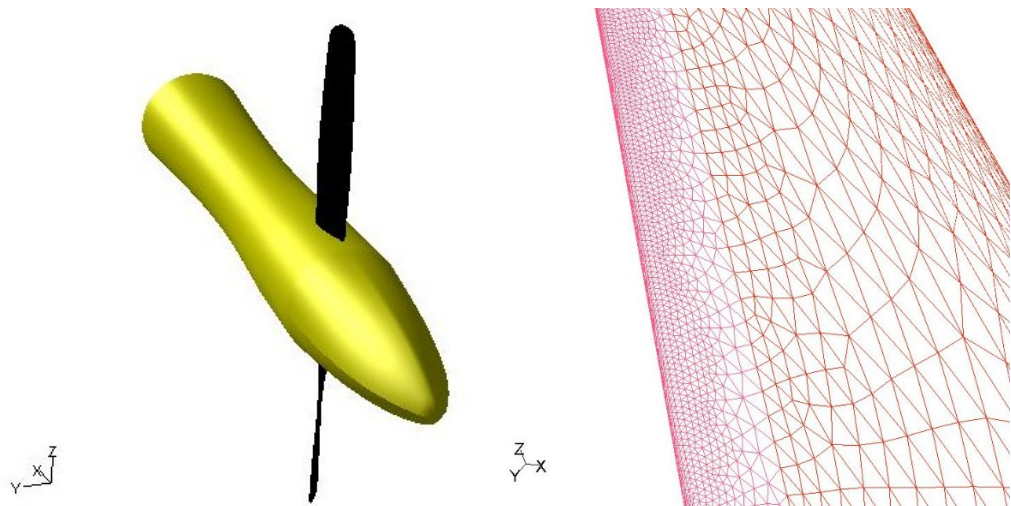
Figure 5-39 Detail of 2 blade NACA 4-(3)(08)-03, CAD and surface mesh.

139

The mesh generated for the NACA 4-(3)(08)-03 propeller was a hybrid mesh similar to that used for the NASA SR2 simulation. 5 prism layers were used and the final mesh contained approximately 2.4 million cells for the 2 and 7 blade configurations in free field. The mesh which included the experimental aeroacoustic apparatus required a cell count of around 4.4 million. All the grids were generated with TGRID.

The height of the first prism layer was chosen in order to be able to use wall function wall modelling available in FLUENT, $30 < y^+ < 150$. In particular, non-equilibrium wall functions were used, which have some correction terms to account for pressure gradient effects.

The main settings used for the simulations are listed below:

- Pressure Based Coupled Solver

- II order implicit Unsteady formulation for transient SLM

- Discretization Scheme: PRESTO for Pressure, II order upwind for all the other convective terms

- Viscous Model: k-ε realizable, non equilibrium wall function

- Green Gauss Node Based gradient discretization

- MRF or SLM model

Some incompressible simulations (e.g. M=0.1) were run with the segregated solver because the coupling of pressure and velocity equations requires much more computer RAM and sometimes 2 GB were not sufficient. Hence, the segregated or coupled solvers were chosen depending on the hardware resources available. The segregated solver should arrive at an identical result, but it can take many more iterations to reach a converged solution.

As stated above, to accelerate the convergence and to avoid some convergence problems, the rotational speed was gradually increased to the target value, starting with a first order discretization scheme to improve stability.

5.3.3 Results

5.3.3.1 NASA SR2

Initial simulations were carried out to investigate the effect of the computational grid on the results. In order to do this, results from tetrahedral and polyhedral grids were compared. The number of prism layers utilised was also varied, but the results did not show large differences. Hence, only results for grids containing 5 prism layers will be reported here. In Figure 5-40 tetrahedral MRF simulation results in terms of aerodynamic coefficients are compared to experimental data. Figure 5-41 shows the same results from a simulation carried out with a polyhedral grid for comparison.
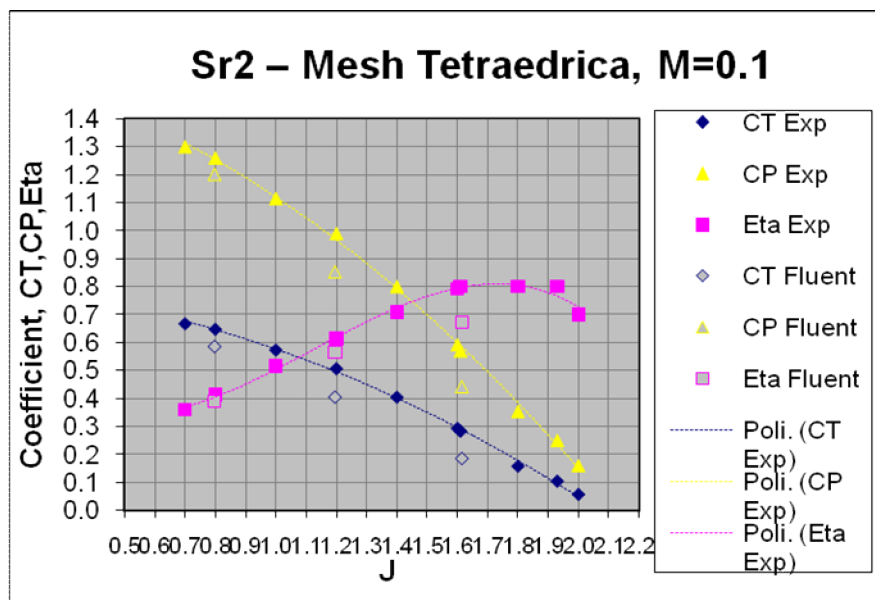
Figure 5-40 Predicted and measured aerodynamic coefficients of SR2 (tetrahedral grid).

141
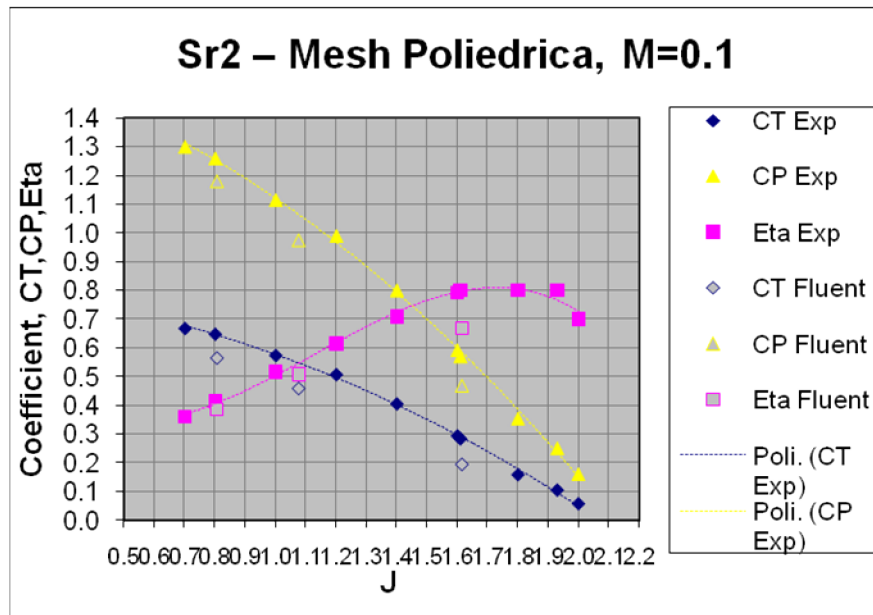
Figure 5-41 Predicted and measured aerodynamic coefficients of SR2 (polyhedral grid).

In can be noticed that the thrust coefficient is always under-predicted, as well as the power coefficient. The error in the computation of the efficiency increases with advanced ratio. Because of these discrepancies encountered at the beginning of the study on the tetrahedral grid a grid sensitivity analysis was carried out to see if the problems could be attributed to the grid being used. The polyhedral grid investigated is quite different in its topology and also changing the number of prism layers is a quite significant change to the grid. But the results of the CFD simulations did not change on these very different grids. It is noted that a more accurate solution could have been achieved by running a simulation with a high quality hexahedral grid. It is known that hexahedral elements are less numerically dissipative and thus results can be more accurate when they are utilised. Other numerical modelling effects were also investigated without changing the grid, by reducing the viscosity of the simulation, changing turbulence modelling, and eliminating turbulence effects completely by carrying out a

laminar simulation. Furthermore, an inviscid simulation was performed which is an even more extreme case. The effect of viscosity on the aerodynamic coefficients is shown in Figure 5-42.
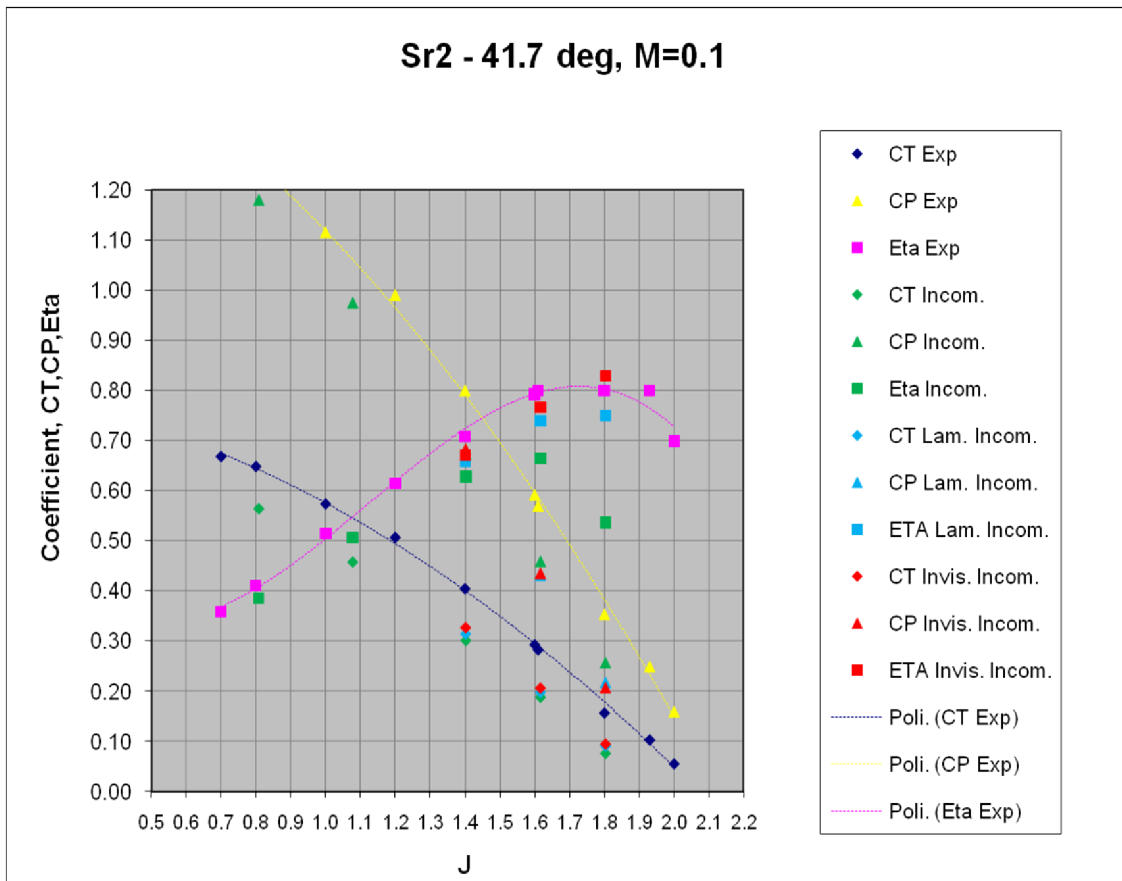

Figure 5-42 The effect of viscosity on the aerodynamic coefficients.

It can be seen that even with an extreme inviscid simulation the thrust is strongly under-estimated as is the aerodynamic power. This may be expected as the thrust depends mainly on the lift generated by the airfoils, which is not very much affected by the viscosity when the flow is not separated on the airfoil sections (as it was verified to be attached). It is clear that decreasing the fluid viscosity reduces the power which is also related to the viscous losses that the propeller experiences in its rotation (P=Mω). These two effects generate the increase in propeller efficiency.

143

It was thought that maybe the thrust and power discrepancies could be caused by a blade angle defect, as may be expected when comparing a simulation which is in an ideal free field with experimental data measured in a real-world wind tunnel. The efficiency errors may be due to an overly dissipative numerical solution of the flow field. For this reason, a blade angle analysis was carried out, Figure 5-43.
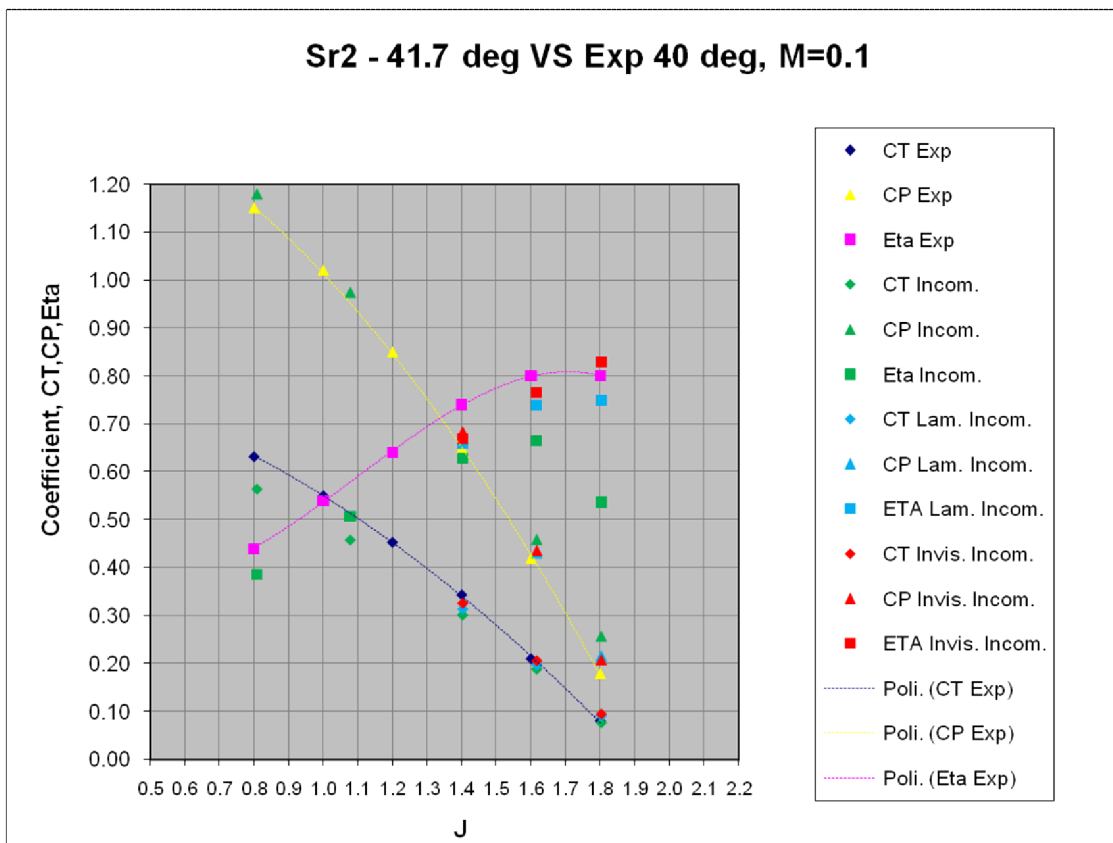

Figure 5-43 Blade angle analysis: computed coefficients at 41.7° are compared to experimental data at 40° blade angle.

The blade angle analysis involved carrying out a simulation at a blade angle of 41.7°. The results of this simulation were found to better match the thrust and power curves for experimental data at 40°. However, an inconsistency was also discovered: the efficiency correlation is actually worse in this case, even for the inviscid simulation. Hence, some doubts about the geometry construction and about how the experimental

measurements were taken arose. Unknown factors in the experimental measurements may be unaccounted for in the CFD analysis. These issues may be caused by a combination of effects: geometry (which was built from tables), experimental data and maybe some inaccuracy in the simulation, in particular at higher advanced ratio, when the absolute values of the forces are smaller and are thus more prone to numerical error. This last error could be reduced by a high quality hexahedral mesh and using less dissipative higher order schemes available in FLUENT (although it was shown that even with an inviscid simulation the agreement with experiments was not improved). Because of these highly relevant discrepancies with the loading computation, further aeroacoustic simulations were not performed. It was decided to work on the NACA 4-(3)(08)-03 propeller which, as we will see shortly, gave much better results for aerodynamic force predictions. Although aeroacoustic analysis was not carried out, the aerodynamic simulations still gave a deep insight into the flow mechanics of the propeller, see Figure 5-44.
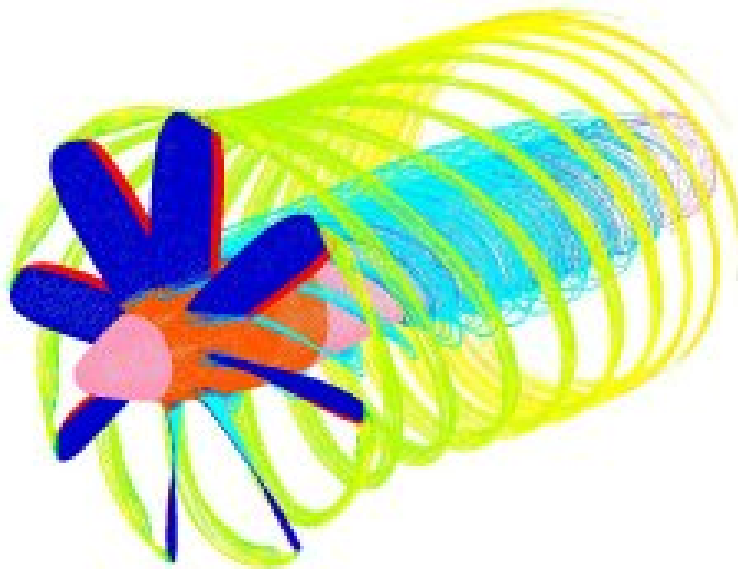

Figure 5-44 Tip vortices detail of the flow field of SR2 propeller.

5.3.3.2 NACA 4-(3)(08)-03

In the Figure 5-45, aerodynamic coefficients computed with the MRF model at M=0.45, 55° blade angle are compared with experimental data. The simulations included compressibility effects, increasing the physical complexity from those carried out on the NASA SR2. This made numerical convergence of the simulations more problematic.
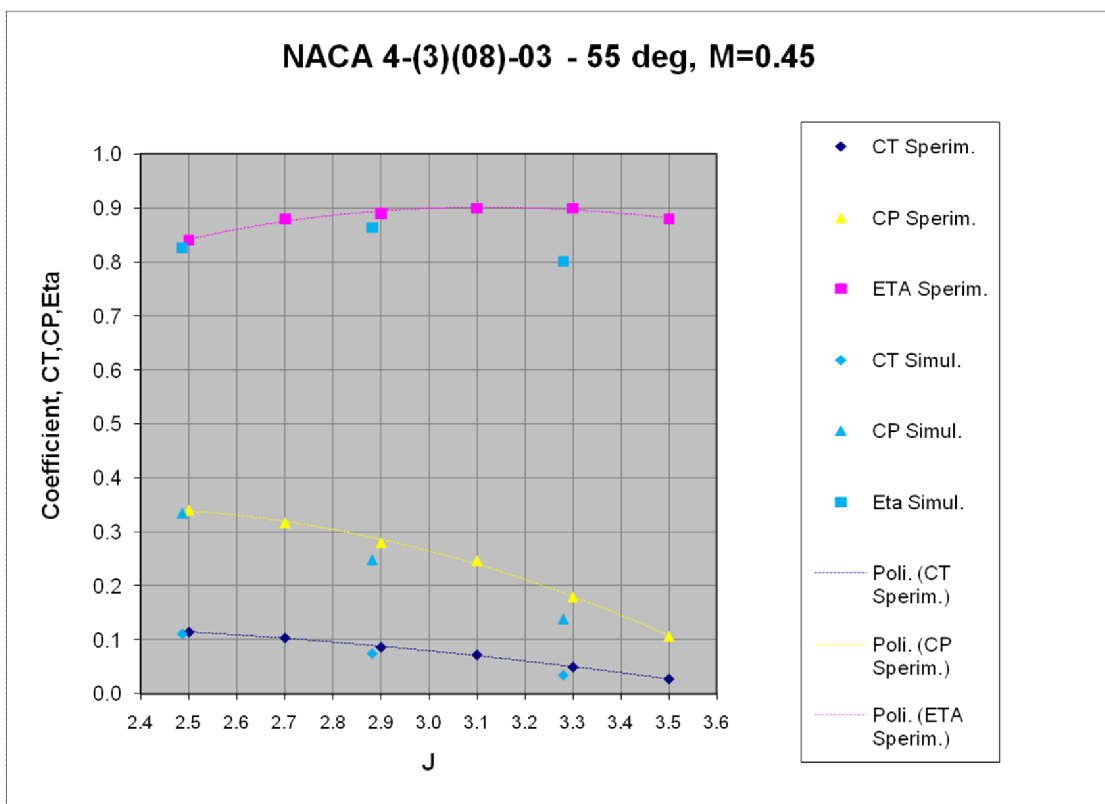

Figure 5-45 Predicted and measured aerodynamic coefficients of NACA 4-(3)(08)-03.

The agreement in this case is very good indeed, for all the curves. At higher advanced ratio the computed efficiency curve start bending before the experimental one. As mentioned above, at higher advanced ratio the forces are smaller and numerical errors may become more significant. As the aerodynamics simulations were in good agreement with experimental data, it was decided to continue with an investigation into the

aeroacoustics. When the simulation is steady as in the MRF it is possible to use the steady state formulation of the Ffowcs-Williams and Hawkings Acoustic Analogy: the Gutin model, available in FLUENT 6.3.23. This is very important because the CPU time can be reduced by almost one order of magnitude from that required for the unsteady formulation.
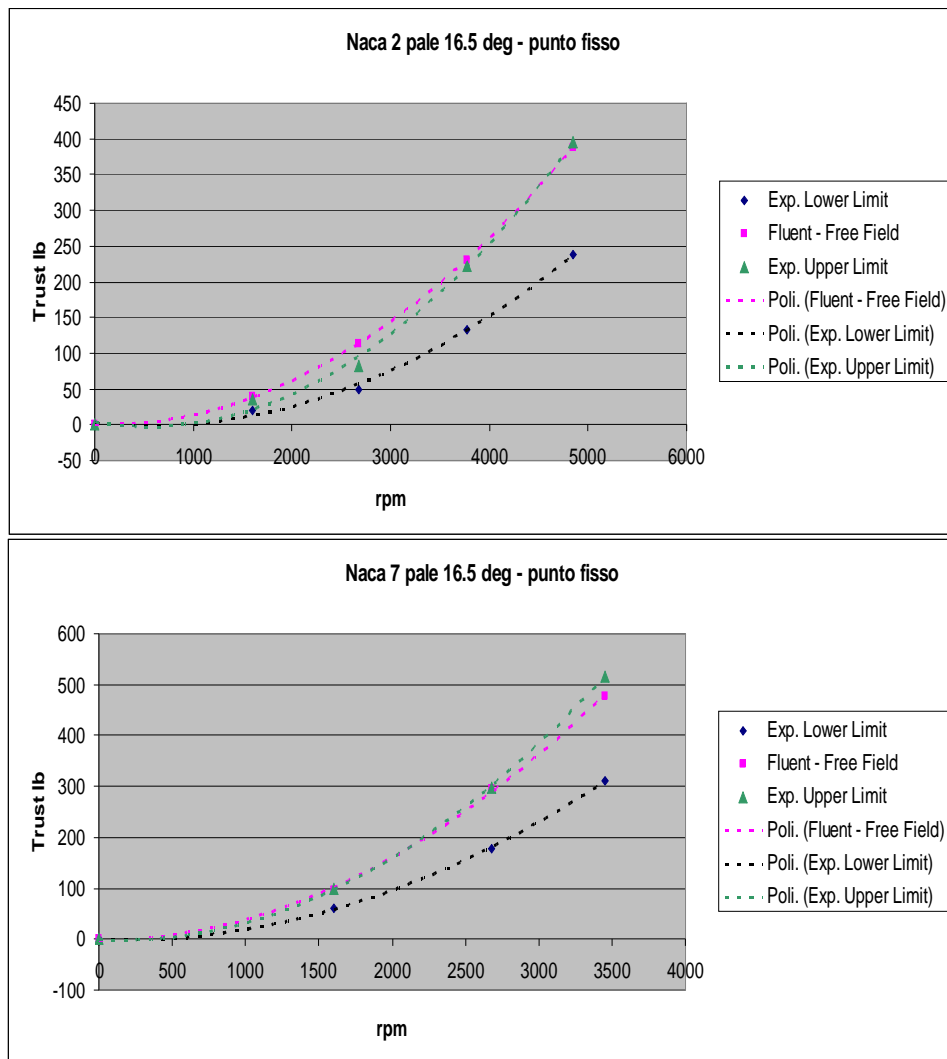

Figure 5-46 Predicted and measured thrust for NACA 4-(3)(08)-03 at M=0.

When the flow direction is not aligned with the axis of rotation it is not possible to use the Gutin model because the loading on the blade is unsteady, so a transient SLM simulation should be performed and the full Ffowcs-Williams and Hawkings Analogy

should be used. The results for the acoustic simulations were first compared in terms of aerodynamic forces.

Figure 5-47 shows the comparison between the computed and experimental thrust for 2 and 7 blade NACA 4-(3)(08)-03 at M=0, 16.5 blade angle as in the aeroacoustic experiments. Simulated results match with the upper limit experimental thrust curve.

After this aerodynamic analysis, noise was computed for different configurations:

- For 2 blade propeller: periodic MRF simulation in free field

- For 7 blade propeller: periodic MRF simulation in free field, unsteady periodic SLM simulation only at 1600 rpm

- 2 blades simulation with ground and test stand: unsteady SLM simulation

An example of the acoustics analysis is shown in Figure 5-45: both with Gutin or full FW-H analogy time pressure history is recorded at the microphone location and then the signal is Fourier transformed in the frequency domain.
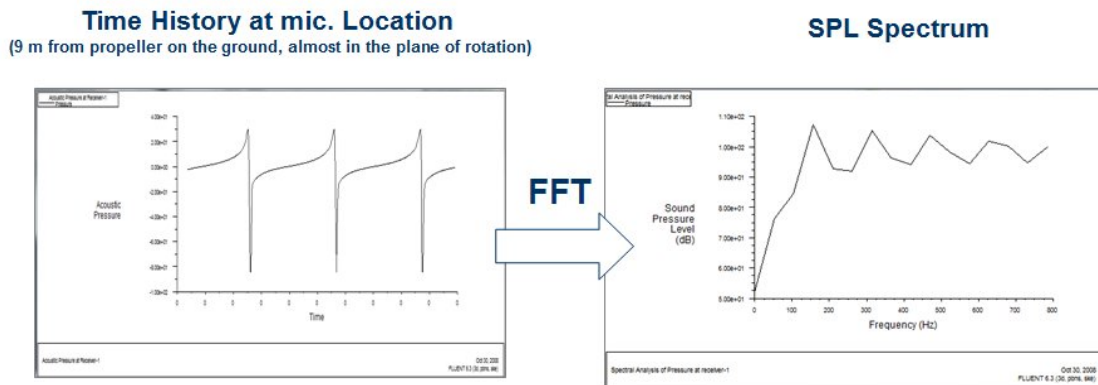

Figure 5-47 Acoustic data post-processing.

Aeroacoustics results for 2 blade propeller are reported in Figure 5-48. The comparison is made at 1600, 2680, 3770, 4850 rpm. For a better understanding of the results it is necessary to explain and detail the legend:

- **OSPL**: Overall Sound Pressure Level

- **OSPL FLU:** OSPL FLUENT - Steady CFD Moving Reference Frame with Gutin Aeroacoustic Model

- **OSPL FLU mod. GUTIN**: OSPL computed with an other Gutin formula [26] with blade loads computed by FLUENT

- **Exp. Wave A. Mic.**: Experimental data OSPL processed with Wave Analyzer (only blade Frequencies and Harmonics are taken into account)

- **Exp. Volt. Mic.**: Experimental data OSPL

- **OSPL FLU GROUND SLM**: OSPL FLUENT - Unsteady CFD Sliding Mesh with FW-H, with ground and test stand
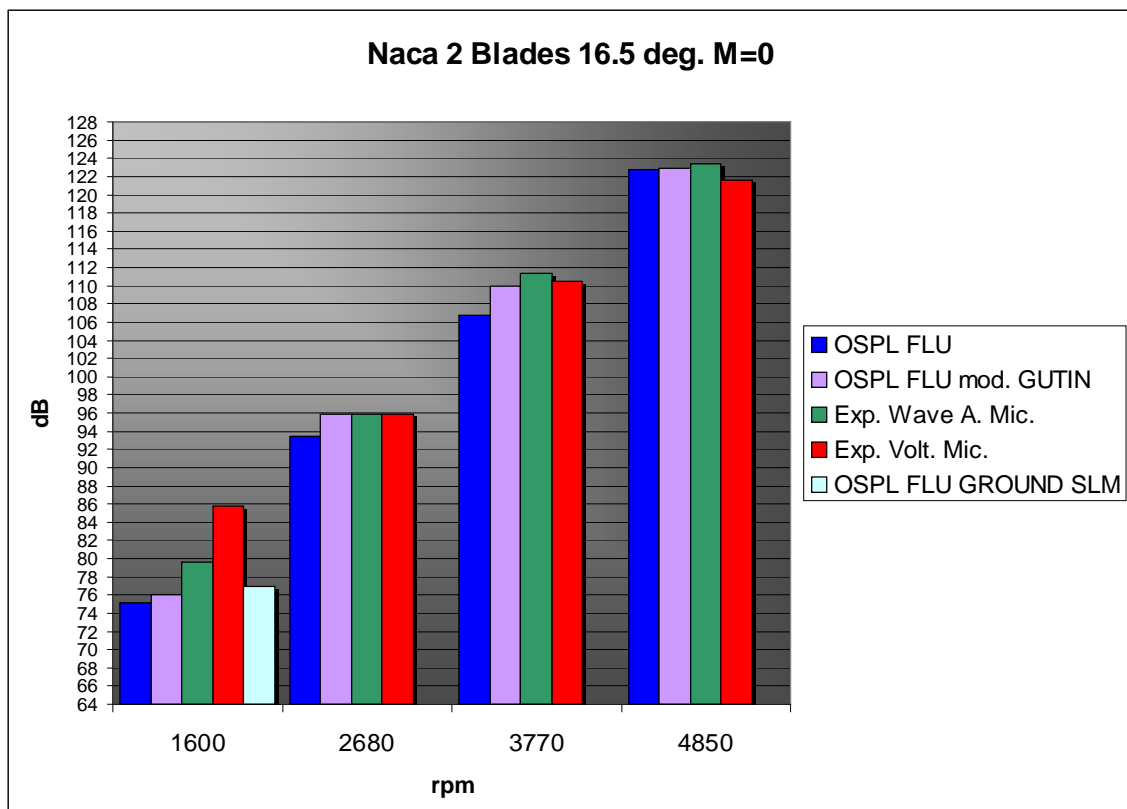
Figure 5-48 Predicted and measured SPL for 2 blade NACA 4-(3)(08)-03 at M=0.

Very good agreement with experimental measurements is obtained at 2680, 3770 and 4850 rpm. The difference with experiments is maximum 1-3 dB for both the computed methods used: directly with FLUENT (referred to as OSPL FLU) and using Gutin formula [26] with the aerodynamic loads computed with FLUENT (referred to as OSPL FLU mod. GUTIN). It is quite evident the under-prediction at low rotational speed.

To understand better these discrepancies we have to point out which is the difference between the two methods used to measure the propeller noise: classic microphone-voltmeter (referred to Exp. Volt. Mic.) and wave-analyzer processed data (referred to as Exp. Wave A. Mic.).

In the first case the measured total microphone voltage is converted directly to decibels. This gives the summation of the entire band of frequencies emitted. When measurements are filtered by wave-analyzer only the sound pressure corresponding to the rotational noise-frequency peaks are summed (the first 5 harmonics).

Therefore, if the vortex noise is strong compared with the rotational noise, as it is usually the case at low tip Mach numbers, values determined by microphone voltage will be larger than values determined from wave-analyzer measurements [26].

So it seems that with a steady MRF simulation the Gutin model it is not possible to predict vortex noise at low rotational speed. For this reason, an unsteady Sliding Mesh simulation was also performed at 1600 rpm (referred to as OSPL FLU GROUND SLM in Figure 5-48) with the ground and the test stand. The sound pressure level computed was 76.5 which was 2 dB higher than the MRF free field simulation, but still under predicting microphone-voltmeter experimental data. It is thought that it is more appropriate to compare aeroacoustic computations with the wave-analyzer measurements. This is

because by using URANS turbulence models we do not detect most of the contribution from all the band of frequencies, in particular broadband noise which is indeed measured by the voltage microphone. Generally by using URANS we catch only the first harmonics peaks. So if we compare to the wave-analyzer measurements we have 76.5 dB level against experimental 79 dB. Similar considerations can be done for the 7 blade propeller configuration shown in Figure 5-49. The agreement between steady periodic MRF simulation and experiment is very good at 3450 rpm and 2680 rpm but it is again much worse at the lower rotational speed of 1600 rpm. It can be seen that the difference between the two methods of experimental measurement is very large at 1600 rpm for the 7 blade propeller. This suggests that vortex noise weighs more compared to rotational noise in the case of a 7 blade configuration compared to a 2 blade one.
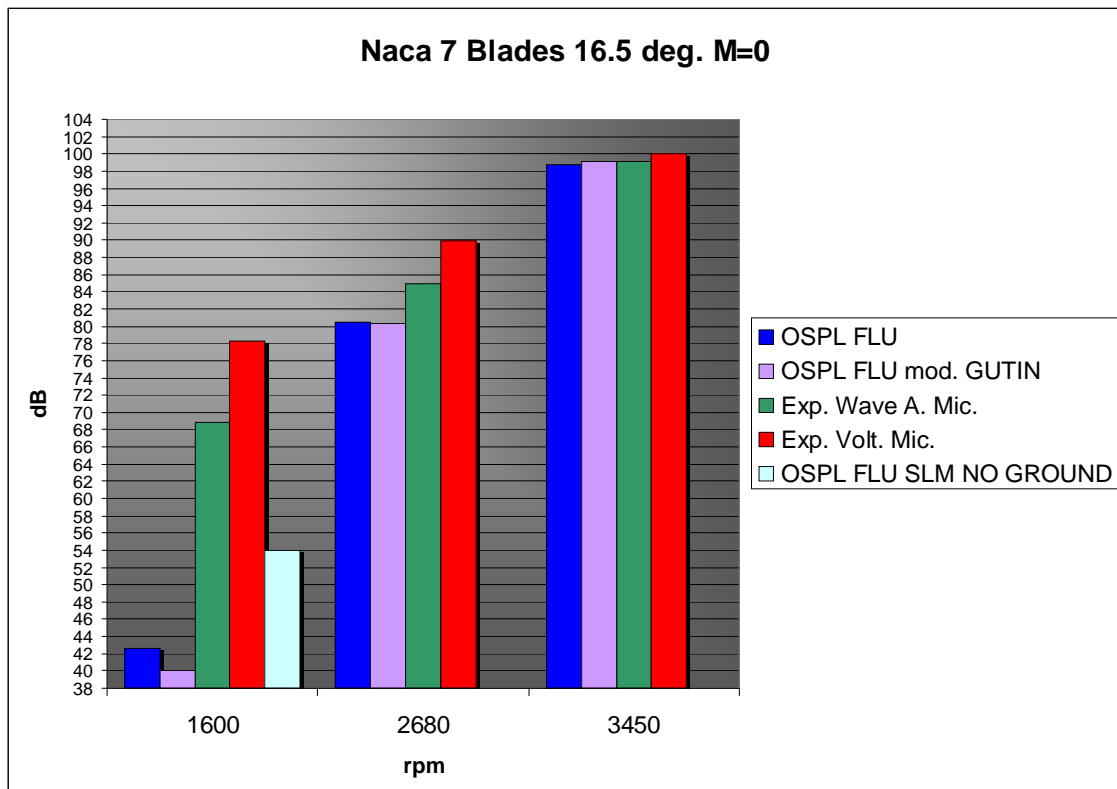

Figure 5-49 Predicted and measured SPL for 7 blade NACA 4-(3)(08)-03 at M=0.

With an unsteady SLM simulation (referred to as OSPL FLU SLM NO GROUND in Figure 5-49, because it is in free field without ground and test stand) the computed results were improved from 42.5 dB to 54 dB, but wave-analyzer is still in poor agreement at approximately 68 dB. The reason for not performing a simulation including the ground and test stand is that, for the 7 blade configuration, the mesh size would have increased to 14 million cells. This is far too computationally expensive for running a transient SLM simulation. An MRF simulation in free field was simulated using periodic boundary conditions such that only one-seventh of the domain could be considered. In order to match the experimental data at 1600 rpm, it is suggested that a much more accurate simulation is needed to be able to catch all the transient features and broadband noise (smaller timestep, DES or LES turbulence model, hexahedral grid).

Figure 5-50 shows a detail of the tip vortices of the SLM simulation with test stand and ground.

Particle Traces Colored by vorticity-mag (1/s) (Time=8.3285e-01) Oct 24, 2008
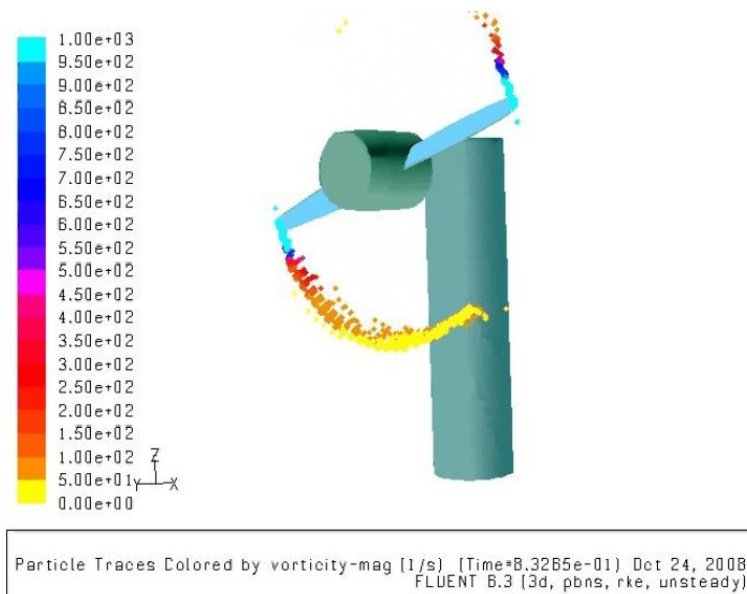FLUENT 6.3 (3d, pbns, rke, unsteady)

Figure 5-50 Flow field detail showing the tip vortices of the NACA 4-(3)(08)-03 at M=0, simulated with SLM model and reproducing the ground test facility for noise measurements.

5.4 JET NOISE

In the following sections the simulation of a heated jet by 2D URANS and 3D LES modelling and the comparison with laboratory experiments will be described. In this case, for noise computation, FW-H analogy with porous surface is the right choice because using CAA is not practical as the microphones are placed quite away, no big obstacles are presents between the source and the receiver, furthermore no physical surfaces are present and the phenomenon is due to the free turbulence of the jet.

5.4.1 Experiments

The experiment was performed in the Small Hot Jet Acoustic Rig in the Aeroacoustics Propulsion Laboratory (AAPL) of NASA Glenn Research Center. AAPL is a 65 ft (20 m) radius, anechoic, geodesic-dome. The walls of the dome and approximately half of the floor area are treated with acoustic wedges made from fibreglass wool to render the facility anechoic above 220 Hz. A 60 in. (1.5 m) exhaust fan in the top of the dome provides air circulation. Flows from all rigs are directed out the 55 ft (16.8 m) wide by 35 ft (10.7 m) high doorway to an open field (Castner 1994). The jet facility is capable of producing heated jets with total temperature from ambient to 920 K in the Mach number range $0 < M < 2$, and therefore ideal for studying the effect of heating. A 2 in. (50.8 mm) diameter convergent nozzle was used for all measurement conditions. Among the all tested conditions it was simulated the case at $M_a=0.9$, TR=2.7.

M_a $=U_j/a_o$	TR $=T_j/T_a$	T_{plen} (K)	M_j $=U_j/a_j$	Uj	ρ_j/ρ_a	Re $X10^6$	γ	Tanna point
0.90	0.840	289	0.982	306	1.19	1.41	1.3999	7
0.90	1.000	335	0.900	306	1.00	1.03	1.3995	12
0.90	1.429	458	0.754	306	0.70	0.55	1.3947	19
0.90	1.818	569	0.671	306	0.55	0.37	1.3845	27
0.90	2.273	699	0.604	306	0.44	0.25	1.3690	36
0.90	2.700	821	0.557	306	0.37	0.19	1.3550	46*
0.60	2.273	675	0.402	204	0.44	0.17	1.3690	33
1.48	2.273	772	0.993	504	0.44	0.42	1.3690	39
1.48	2.700	893	0.916	504	0.37	0.32	1.3550	49*

* Higher temperature ratio (2.86) used by Tanna, Dean and Burrin (1976)

Figure 5-51 Operating conditions of the tested jet.

Here M_a is the commonly used parameter for sound radiation (that involves coupling between jet velocity, referred to as U_j in Figure 5-51, and ambient sound speed, referred to as a_0), the compressibility effect is represented by the jet Mach number $M_j = U_j/ a_j$, $TR=T_j/T_a$ is the jet static temperature ratio, where a_j is the speed of sound and T_j the temperature in the jet core.

The far field sound pressure fluctuations were measured by an array of seven ¼ in. (6.35mm) microphones kept on an arc of 100 D (5.08 m) and centred at the nozzle exit. The microphones were angularly placed with 10° increments: from 150° to 90° to the jet exit (Figure 5-52). Polar angles were measured from the flight direction (opposite to the jet direction). The presence of the large traversing unit, optical components and other metal surfaces was a concern for significant acoustic reflection. To minimize such reflection a large part of such surfaces were covered by 50 mm thick polyurethane foams.

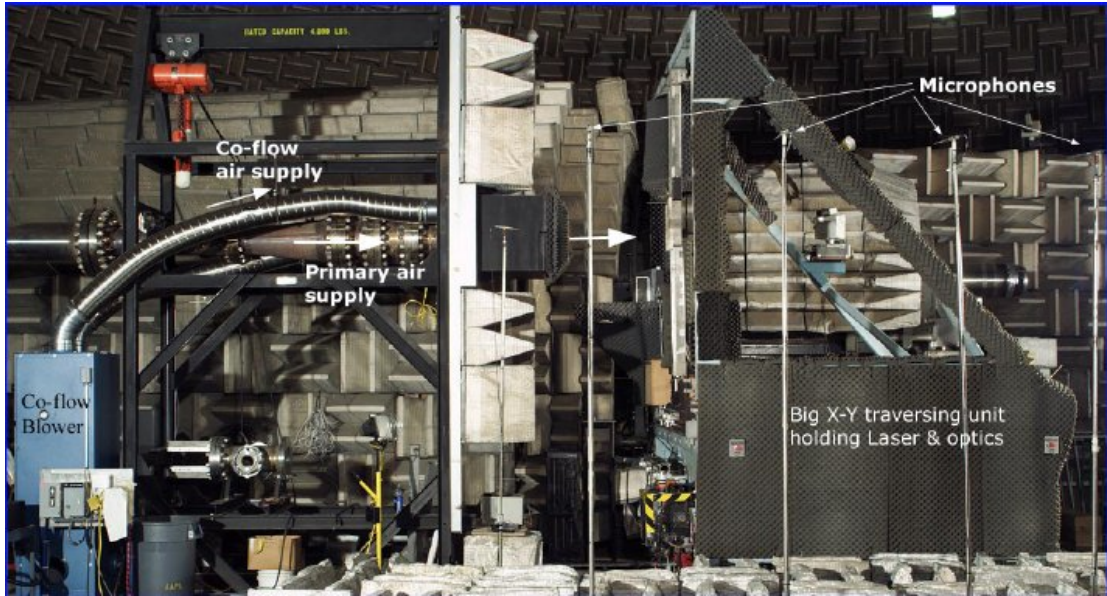Figures 5-52, 53 show some details of the experimental apparatus.

154

Figure 5-52 Photograph showing side view of the Small Hot Jet Acoustic Rig, X-Y traverse holding the Rayleigh setup, and microphones.
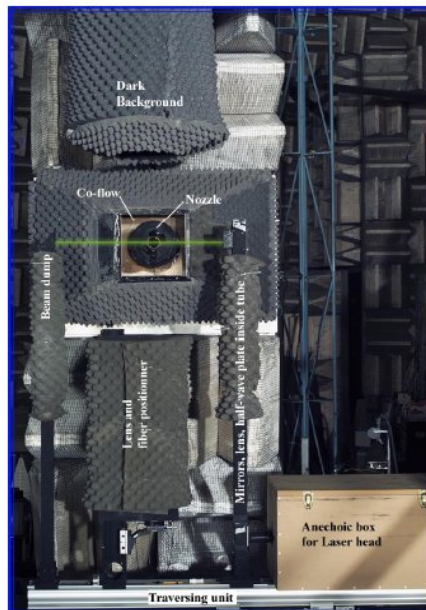

Figure 5-53 Photograph showing the front view of the jet facility and the Rayleigh setup.
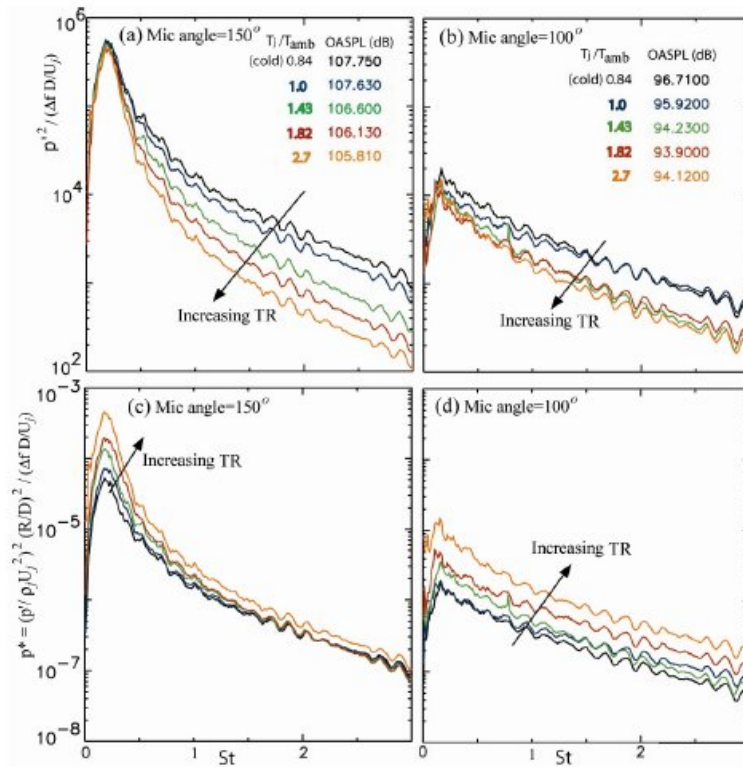
Figure 5-54 Far field, narrowband, microphone spectra from indicated polar angles obtained from fixed $M_a = 0.9$ jets at indicated temperature ratios. (c) and (d) show the same data in (a) and (b) but normalized by a different factor. All microphones were positioned on a 100 diameters arc (diameter=2 inches).

The effect of heating on the far field noise spectra of a fixed velocity ($M_a = 0.9$) is shown in Figure 5-54. The narrowband spectra were obtained from power spectra calculations of the microphone time signals. The frequency values were converted to Strouhal number $St = fD/U_j$ (f is frequency), and the power spectra S_p^2 were converted into spectral density per unit Strouhal frequency $S_p^2/ (\Delta f D/ U_j)$, where Δf is the width of each frequency bin. Interestingly, Figure 5-54 (a) shows that in the shallow angle the low frequency part $0 \leq St \leq 0.5$ remains nearly unchanged with increasing plume temperature, while the higher frequency part continually decreases. For the 100° location, heating causes progressive lowering of sound emission at all frequencies. The increase in the jet temperature is expected to reduce high frequency radiation from the shallow angles due

156

to increased refraction. However, refraction can not be attributed to the reduction measured by the 100° microphone. The effect of heating at Ma = 0.9 is weakening of the noise sources [37].

A different conclusion can be reached when the effect of the density reduction with increased plume temperature is accounted for [37]. The lowering of air density proportionately reduces the thrust generated by the jet (proportional to $\rho_j U_j^2$). To account for the density variation noise spectra are normalized following the procedure of Mollo-Christensen and Narasimha (1960) and Zaman and Yu (1985). In this method, the narrow band spectra is normalized by $\rho_j U_j^2$, jet diameter, microphone distance from the nozzle exit R and Strouhal frequency, Figure 5-54 (c), (d).

The far field spectra measured by Tanna [38] show the same trends at the same conditions of the experiments presented above at Aeroacoustics Propulsion Laboratory (AAPL) of NASA Glenn Research Center.

It was decided to compare the simulated data to the experimental one by Tanna at the chosen conditions showed in Figure 5-51, because more detail was found about the post-processing of spectra, [38]. The only difference is the distance of the microphones, 72 diameters instead of 100.

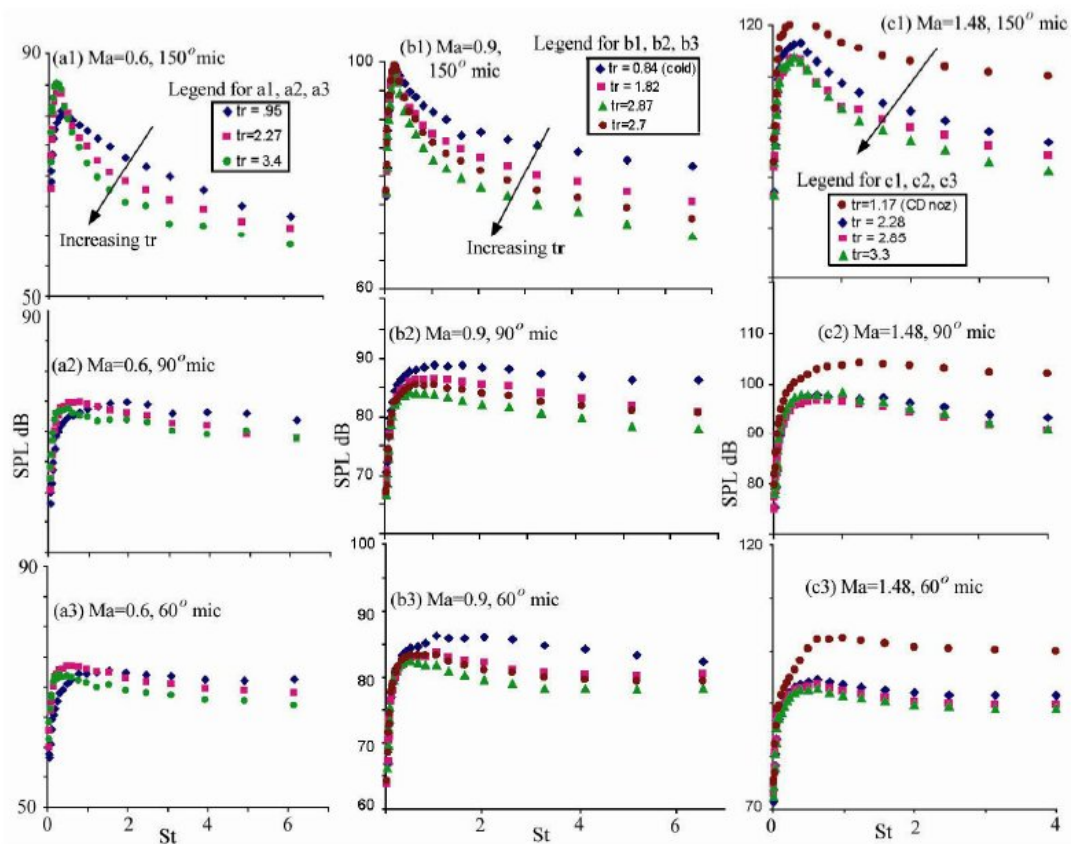In Figure 5-55 the measurements of Tanna are showed.

Figure 5-55 Far field noise spectra from jets produced by 2 inches diameter nozzle at different Ma and TR. Columns (a), (b), and (c) presents data at Ma = 0.6, 0.9, and 1.48 respectively; rows (1), (2), and (3) are from different microphone angles θ = 150°, 90°, and 60° respectively. All microphones were positioned on a 72 diameters arc. All data are from a convergent nozzle except for a convergent-divergent nozzle for the unheated Ma = 1.48 jet. Measurements by Tanna, [38].

5.4.2   Simulation Set Up

Before proceeding to simulate the 3D case, it was decided to tune the methodology using a 2D URANS axisymmetric simulation. The aims of the 2D simulation were to design the dimension of the domain, to verify the boundary conditions used and to find a suitable position for the porous surface (referred to also as permeable surface) where pressure fluctuations are recorded for the Acoustic Analogy. The 2D grid is then used to create the 3D grid.

158

In the following Figure 5-56 the 2D domain is shown along with the boundary conditions used. Figure 5-57 shows the details around the nozzle exit area..
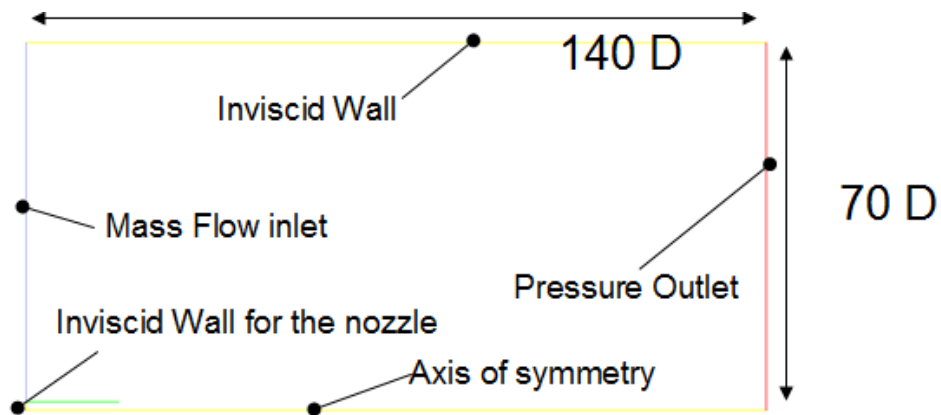

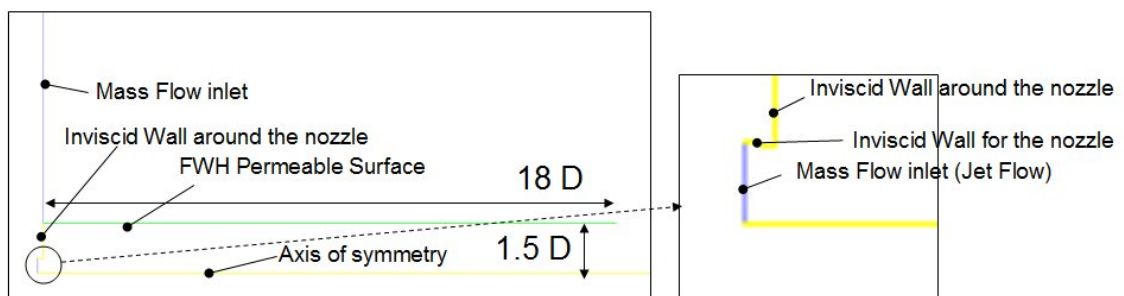**Figure 5-56 Computational 2D axisymmetrical domain with boundary conditions used.**

Figure 5-57 Detail at the nozzle exit and of the FW-H porous surface.

A large domain was utilized for the following reasons:

- To eliminate spurious reflections when not using Non Reflective Boundary Condition (NRBC are available only for Density Based Solver with some limitations, and not for PBCS)

- To allow large cells at the far-field to act as a numerical filter damping high frequency pressure wave

- To eliminate reversed flow at the boundaries. To obtain this it was also added a low mass flow inlet (about 4 m/s) at the inlet boundary, far from the shear layer.

This will have a negligible influence on the noise prediction (Jet Velocity ~ 300 m/s)

The guideline for designing the mesh was the following:

- high quality hexahedral cells
- mesh edge length
    - ~ length scale of turbulent eddies
    - ~ 20 grid points/wavelength
- high resolution in the shear layer and close to the nozzle exit

The grid in the propagation region (the fluid volume inside the FW-H porous surface) we had a maximum grid spacing of 4.6 mm, up to frequencies of 2000 Hz (St=0.4). Such a grid spacing allows 35 points per wavelength. Figure 5-58 shows some details of the grid. The 3D model was about 3,2 million hexahedral cells.
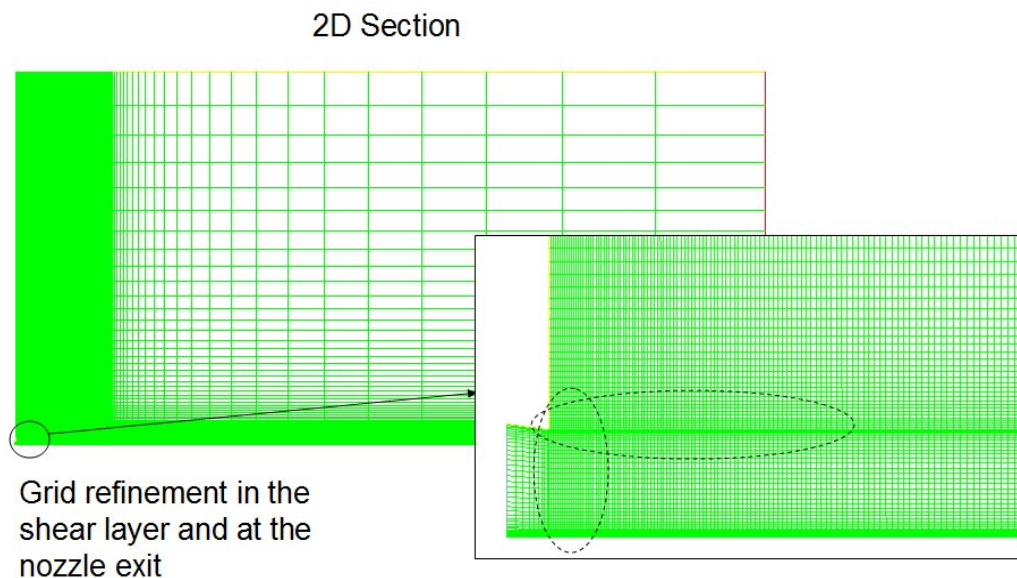
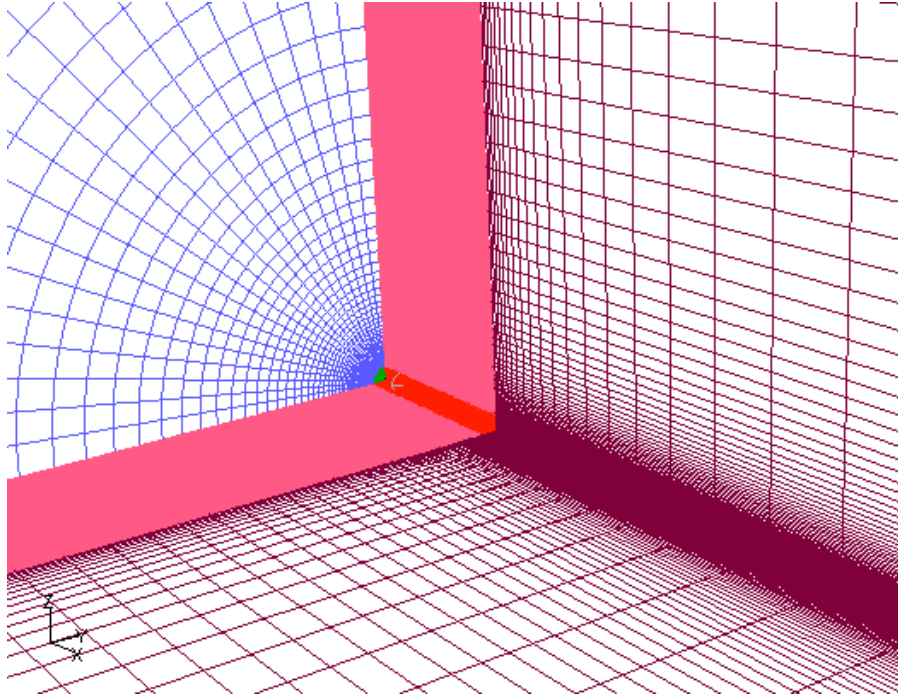**Figure 5-58 Detail of the grid used for the Jet simulation.**

160

Figure 5-59 Detail of the grid used for the Jet simulation.

The FW-H porous surface position was set based upon results from the 2D simulation according to the following requirements:

- must enclose all the main aeroacoustic sources of interest

- must be as small as possible because inside sound propagation must be computed (CAA) and for longer paths more sound will be dissipated

- must not cross high vorticity and non linear regions (in this case it was left open at the bottom)

Figure 5-60 shows the results of the 2D simulation verifying the position of the FW-H porous surface. Areas of high vorticity can be seen to lie within the FW-H surface.
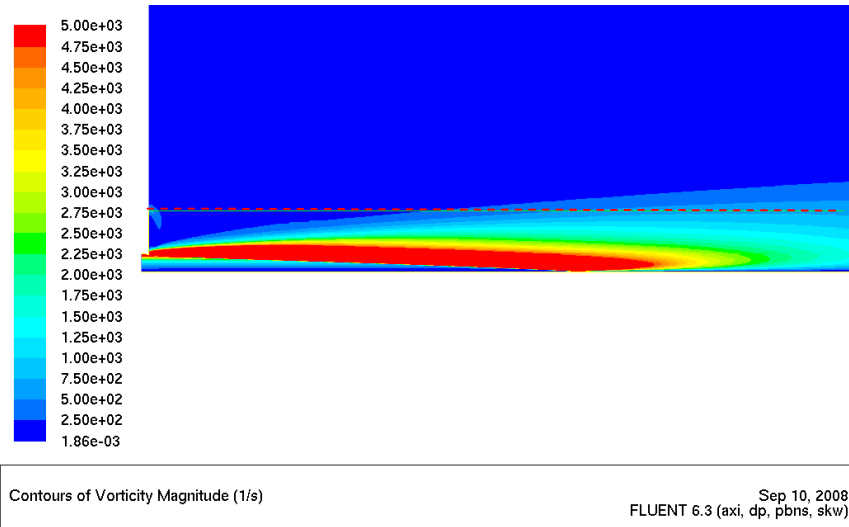
Figure 5-60 Vorticity Magnitude for the 2D axisymmetric simulation.

Figure 5-61 shows the contour plot of the acoustic power using the Proudman's formula [46]. This gives an indication about the quadrupole source strength; areas of high acoustic power are all inside the FW-H permeable surface.
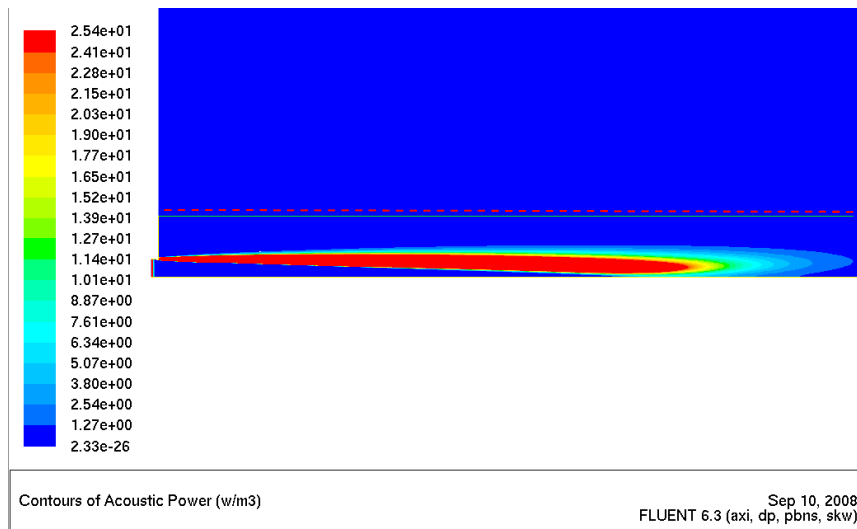

Figure 5-61 Contour of Acoustic Power calculated by Proudman's formula, 2D axisymmetric simulation.

The timestep was set to 1e-05 s, which guarantees more than 30 points in the period corresponding to the signal of 2000 Hz. Cell Courant number was <1 in almost all the domain as shown in Figure 5-62 for the 3D LES simulation.
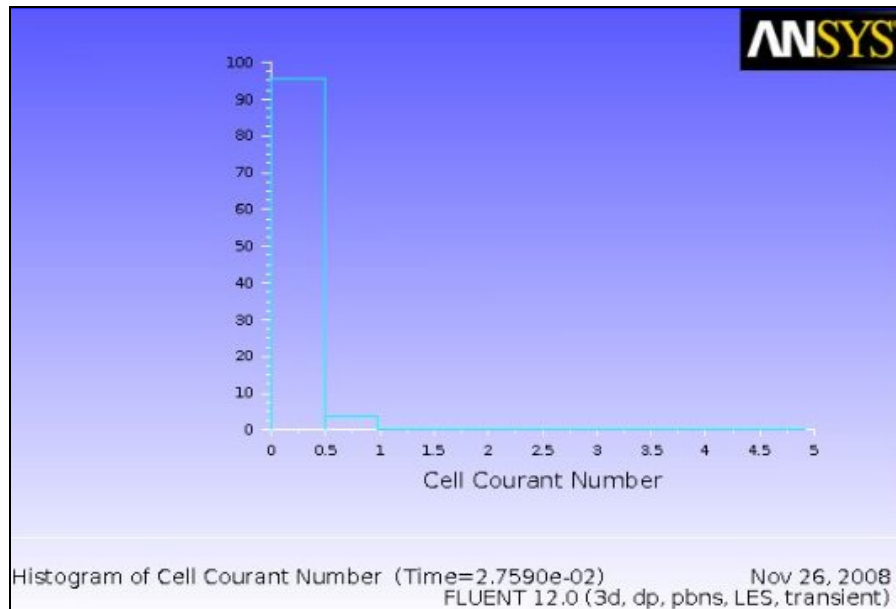

Figure 5-62 Histogram of cell Courant number for 3D LES simulation, 99% of the cells in the domain have a value<1.

The main settings used for the simulations are listed below:

- Double Precision Pressure Based Coupled Solver

- Ideal gas law for air density

- II Order implicit unsteady formulation

- Discretization: III order QUICK for URANS simulation, Bounded Central Differencing for LES

- Viscosity: Sutherland Model

- Thermal Conductivity: Kinetic Theory Model

- Viscous model: k-ω standard for URANS, Lilly-Smagorinsky for LES

163

The simulation was initially run until a dynamically steady state was reached. Subsequently, the FW-H model was activated and the simulations run for 2000-3000 time-steps.

5.4.3 Results

In Figures 5-63 and Figure 5-64, the sound computed at a distance of 72 diameters and at 150° and 90° to the jet axis by 3D LES simulation is shown (the axis direction is opposite to the jet flow direction), using FW-H porous formulation. The agreement with experiments is good, in terms of absolute values and trend predictions. The spectra are 1/3 octave band SPL and the frequencies are reported as Strouhal numbers. In this case the conditions were M_a=0.9, TR=2.7, T_j=821 K.
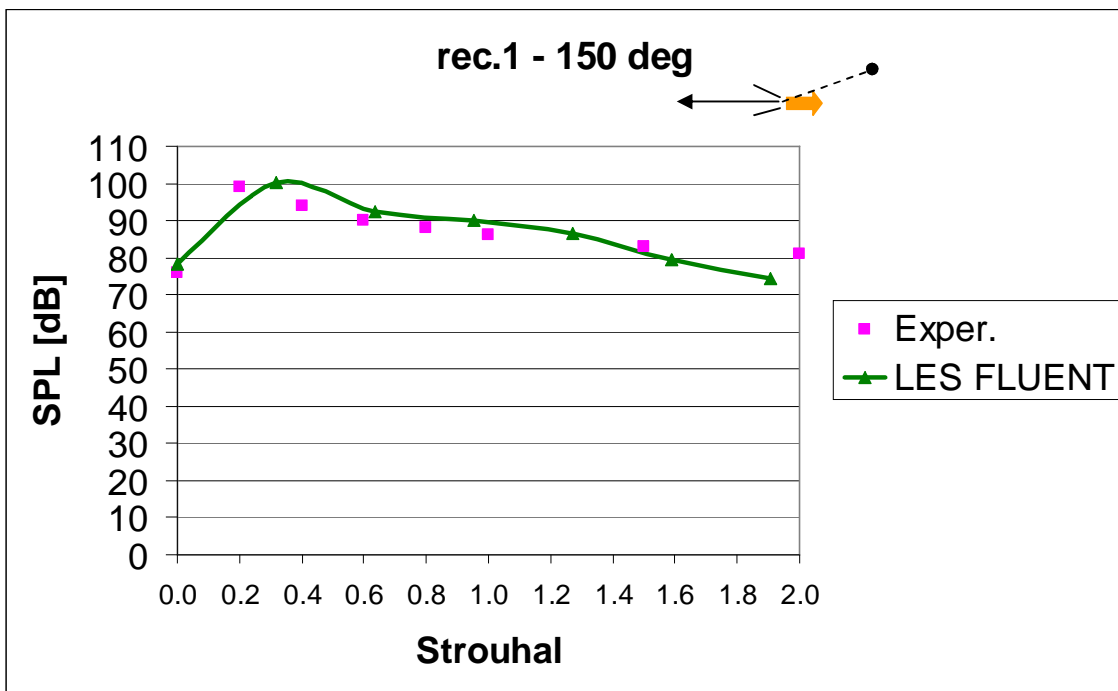

Figure 5-63 Predicted and measured SPL of the heated jet at 150° to the jet axis.

Figure 5-63 shows that at 150° the SPL peak is predicted at a slightly higher frequency than the experimental measurement. In Figure 5-64 it is shown that at 90°, the reduction of SPL (relative to that calculated at 150°) is well captured, as is the lesser gradient of the curve.

As outlined in the previous section regarding the design of the grid and of the time-step size, the results should be considered reliable up to a Strouhal number of about 1 (10-15 points per wavelength for a signal of 6000 Hz ~ St=0.95).
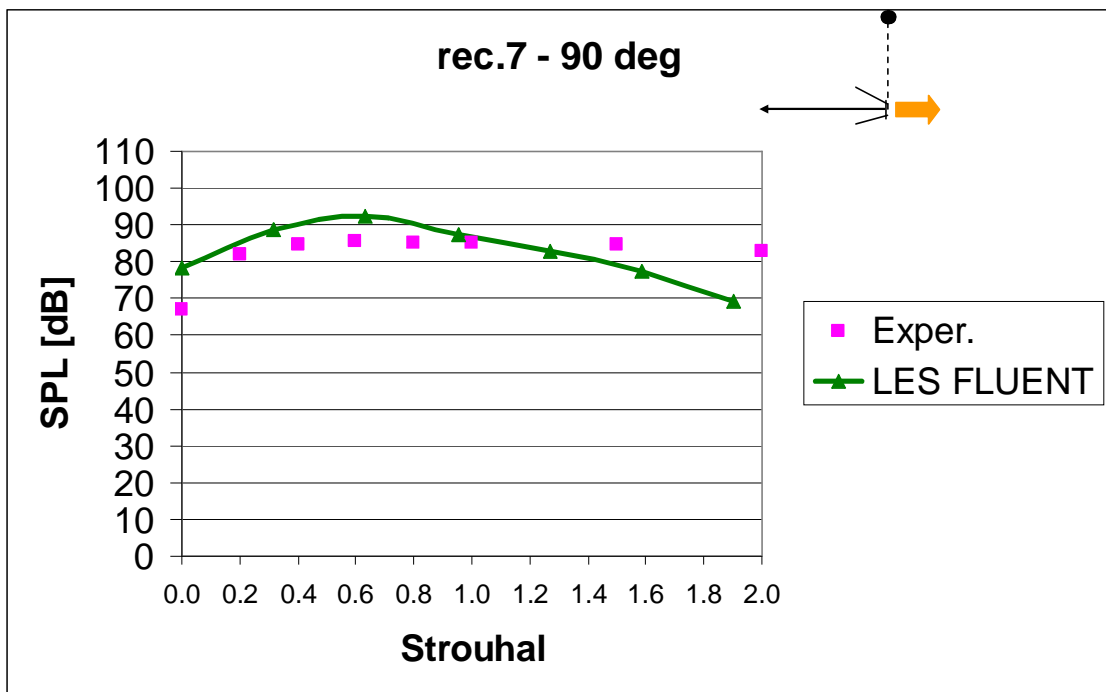

Figure 5-64 Predicted and measured SPL of the heated jet at 90° to the jet axis.

LES simulations can give a great insight into the physics of the heated jet. In Figure 5-65 and 5-66 the instantaneous velocity magnitude contour as well as the time–averaged velocity magnitude contour over a long duration are shown.

It is interesting to notice that the potential core is well distinguishable only in the time averaged image, see Figure 5-66.
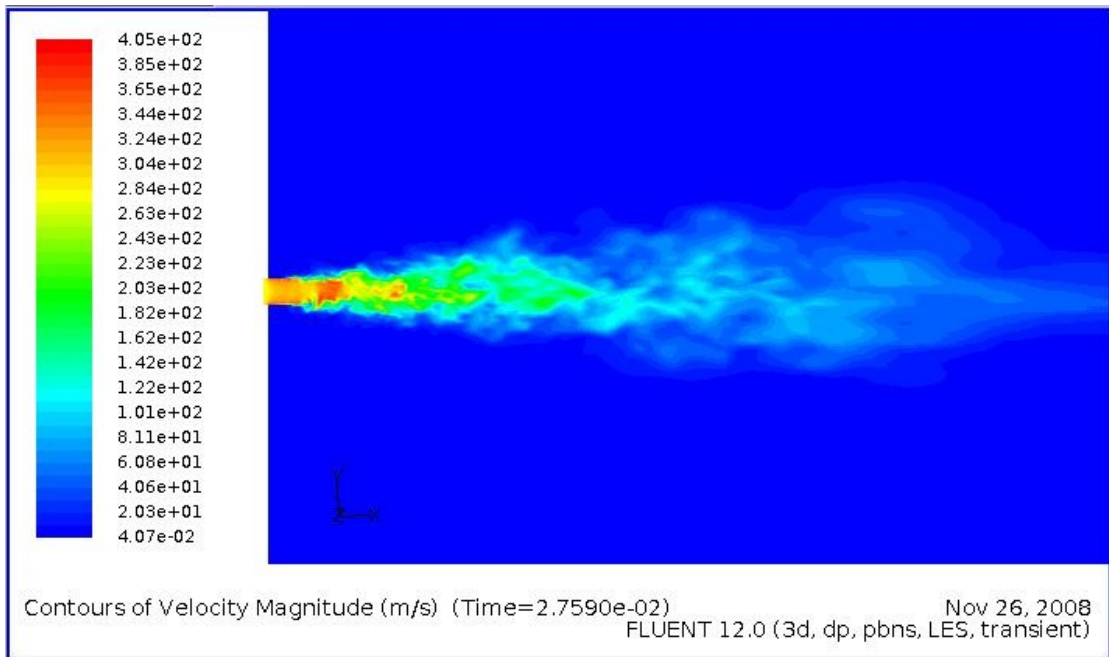
Figure 5-65 Instantaneous contour plot of velocity magnitude in the centre plane.
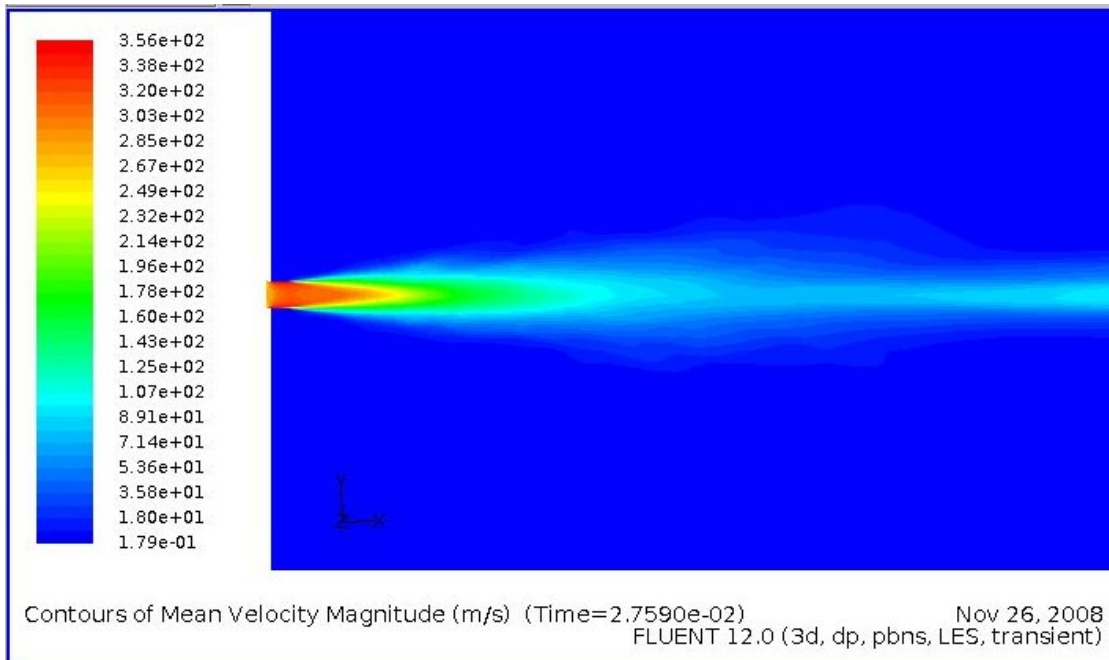

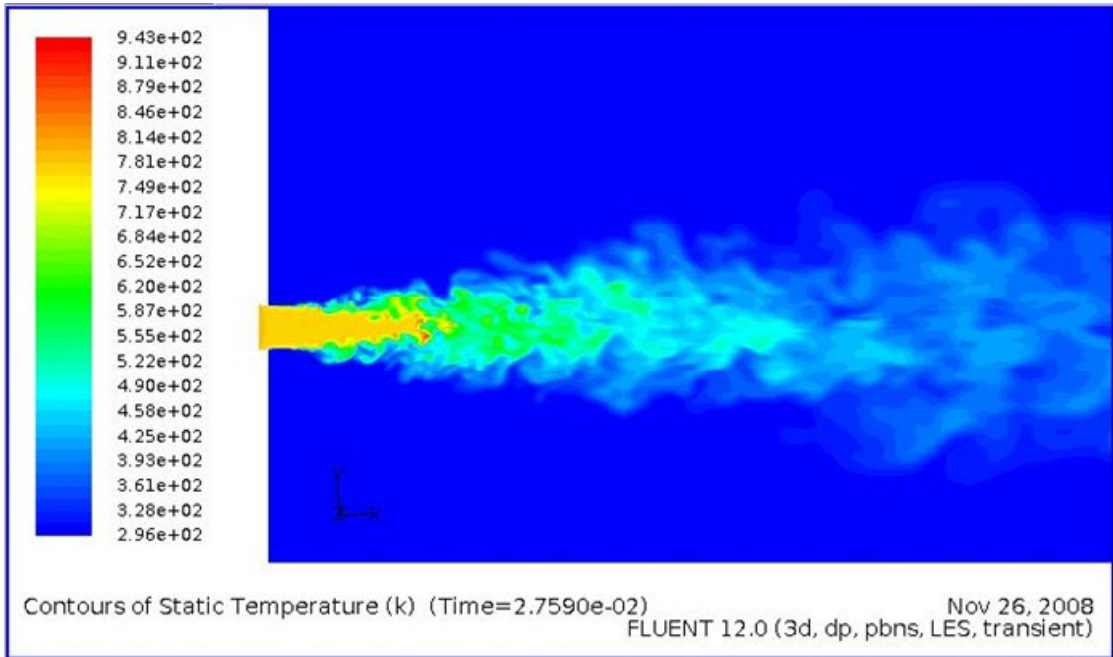**Figure 5-66 Time averaged contour plot of velocity magnitude in the centre plane.**

Figure 5-67 Instantaneous contour plot of static temperature in the centre plane.
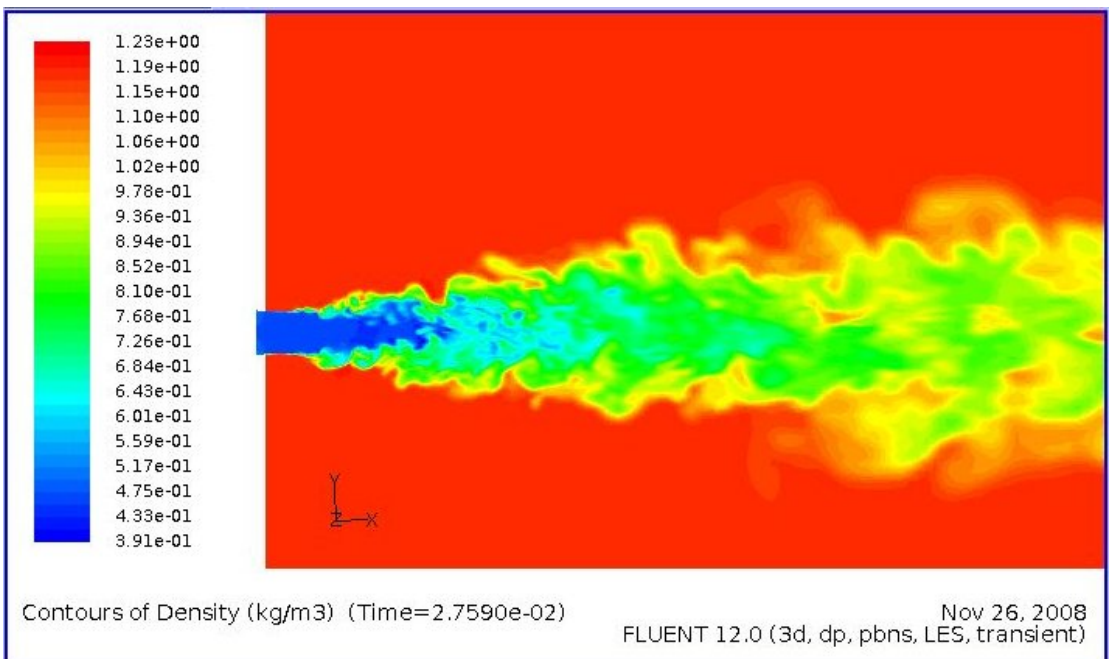

Figure 5-68 Instantaneous contour plot of air density in the centre plane.

167

Figure 5-67 and 5-68 show instantaneous contours of the static temperature and air density through the centre of the jet. It is clear that all the mixing happens in the shear layer, which is appropriately named the mixing region. In Figure 5-69 the Root Mean Square (RMS) of the static temperature shows where the main unsteadiness of temperature occurs. It is evident that the potential core is very stable as it experiences almost negligible fluctuations.
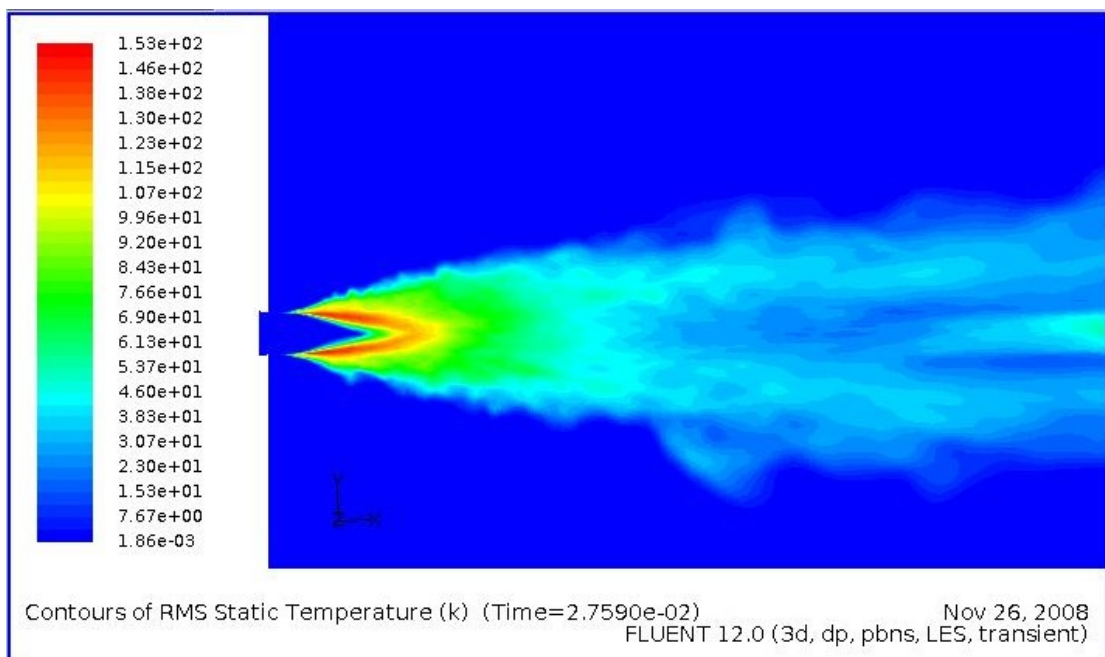
Figure 5-69 RMS contour plot of static temperature fluctuations in the centre plane.

High vorticity regions are visible around the end of the potential core and few diameters downstream, see Figure 5-70. As this is also the area that experiences the main unsteadiness in pressure, see Figure 5-71, it may be considered a region of strong noise sources according to the theory presented in Chapter IV.

Figure 5-72 gives an insight into the turbulent length scale structure of the jet. Iso-surfaces, using the *Q*-criterion (Hunt, Wray & Moin, 1988) are coloured by static

temperature. The smaller scales near the potential core and the bigger scales further downstream are clearly visible.
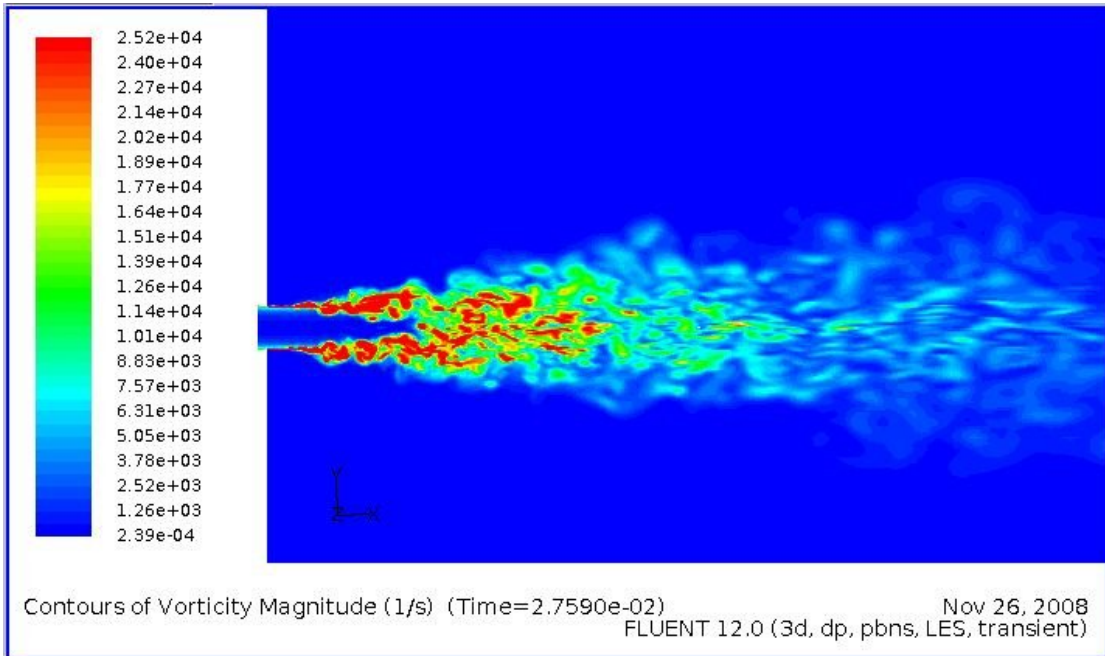

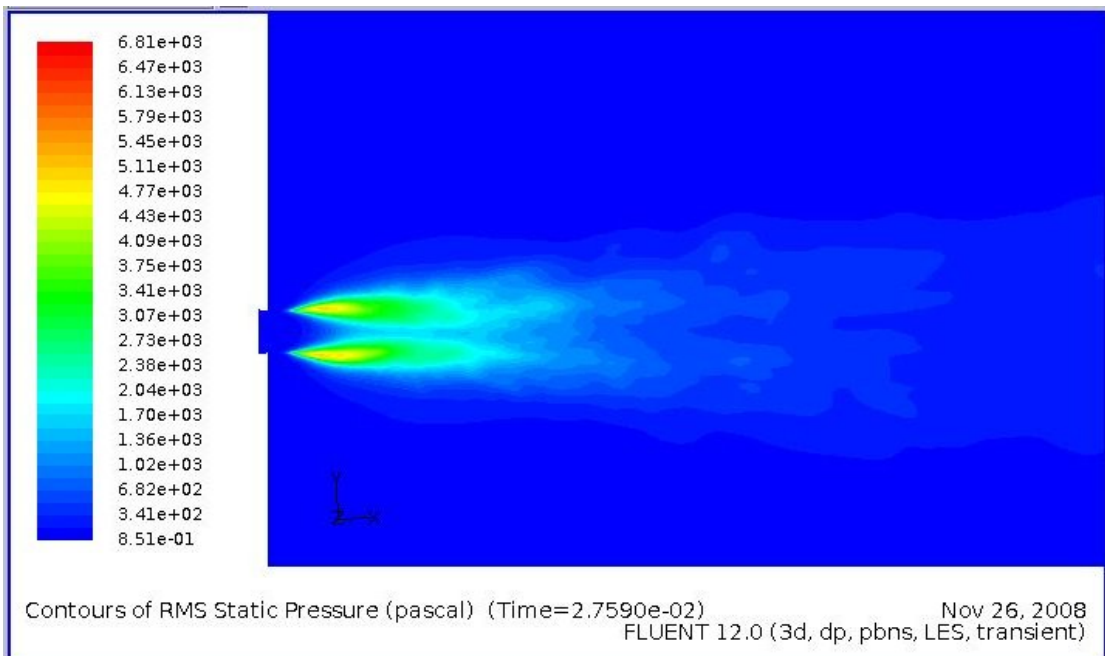**Figure 5-70 Instantaneous contour plot of vorticity magnitude in the centre plane.**

Figure 5-71 Contour plot of RMS static pressure fluctuations in the centre plane.
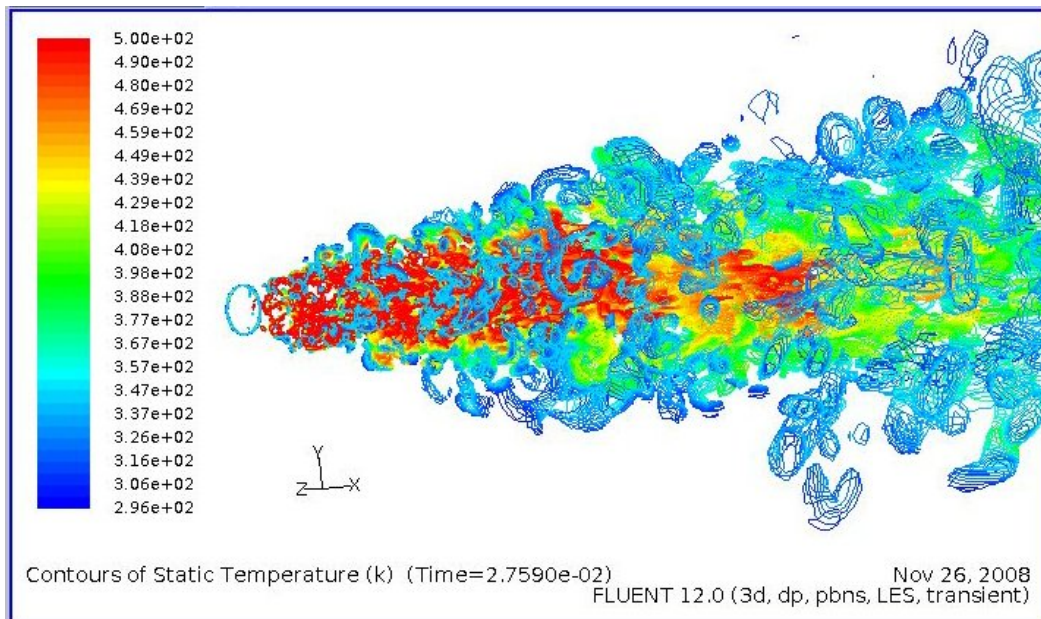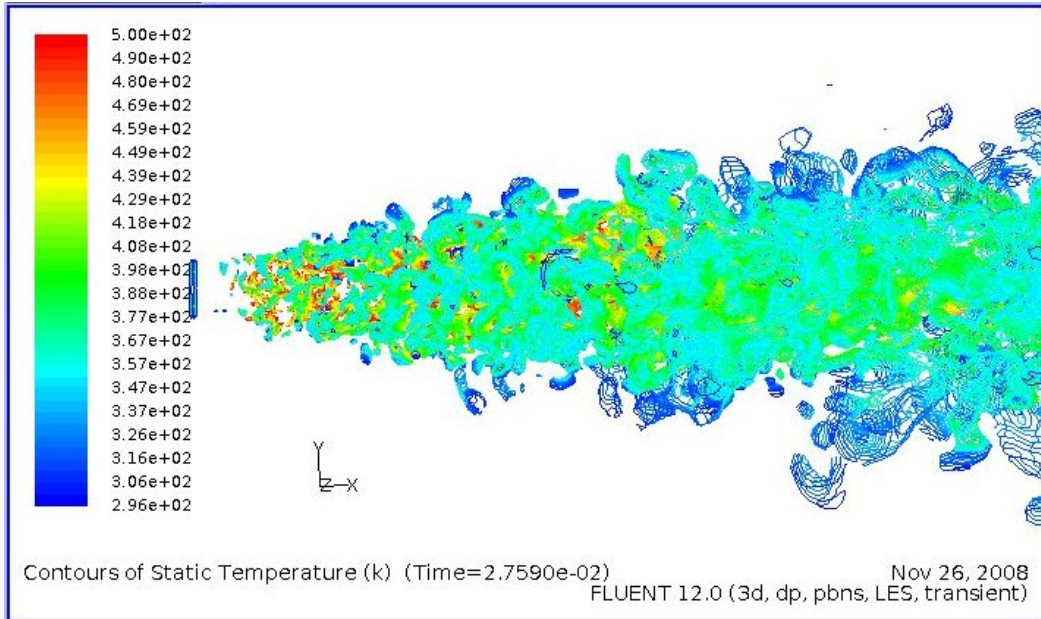
169

Figure 5-72 Iso-surfaces created by applying the Q-criterion, colored by static temperature.

6 CONCLUSION

Methodologies for simulating different types of aerodynamically generated noise have been developed herein. Limitations in these methods have been highlighted and suggestions have been made for the optimum approach to simulate each type of noise considered. In order to do this, an entire Chapter of this study is dedicated to the understanding of noise generation mechanisms. Such an understanding is fundamental to ensure the simulation is set up correctly and to properly analyze the results. Engineers today can often be too hasty to simulate almost everything by CFD, without first deepening their understanding of the fundamental physical phenomena which they look to investigate. This generally leads to poor results and the impossibility to understand which step to subsequently take in order to improve their results. Today, this is particularly true in the area of aeroacoustics, which still represents a promising but challenging area of research in the industrial environment.

The investigation into cavity noise showed how it is possible to predict the fundamental physics of buffeting with a "cheap" CAA 2D, compressible URANS simulation. Results were presented which illustrated the ability of such a simulation to predict the frequency of the coupled system, as well as the noise. Particular attention has been paid to the construction of the computational grid and simulation procedure used. It was shown how important the prediction of the boundary layer thickness at the leading

edge of the cavity is, as this affects the convective velocities of the shed vortices and thus the frequency of buffeting. Comparisons with experiments and with other CFD simulations from an important Aeroacoustic Benchmark [36] were reported. The computational cost was considered "cheap" because the simulation time, on a modern dual or quad core PC, would be around 2 days. This gives the possibility to use such a simulation method as a tool to compare many different design configurations in order to improve the acoustic performance, e.g. automotive door gaps. Recommendations for future work on this subject would be to focus on computationally expensive 3D simulations using LES or Detached Eddy Simulation (DES) turbulence models, to enable the prediction of not just the tonal peak but also some broadband components.

The vortex shedding noise caused by fluid flow over cylinders has been thoroughly investigated. Acoustic computations made use of the FW-H acoustic analogy. The locations of the main sources of noise were found and used to choose optimal positioning for the FW-H integration surface. The limitations of 2D URANS simulations were highlighted which could be overcome by more detailed 3D LES simulations. Unfortunately, it was not possible to run high Reynolds number simulations for aeroacoustic comparison as they would be too computationally expensive to be run on the hardware available (dual or quad core PCs). Such simulations would require a large cluster of PCs for parallel CFD computations. A 3D LES simulation was run at a Reynolds number of 3,900, showing very good improvement in both drag and Strouhal number prediction. A study was also detailed on how to size a LES computational grid by post-processing a cheaper RANS simulation. As expected boundary layer separation and transition were shown to be highly dependent on the Reynolds number of the flow. These

phenomena strongly affect the vortex shedding and the emitted noise, and they were seen to be accurately captured by the use of the k-ω SST transitional-flow turbulence model. Comparison with unsteady aerodynamics and noise measurements were shown.

An extensive study was dedicated to propeller noise simulation. The investigation began with aerodynamic simulations of propellers. A deep exploration into the computational methods available for simulating rotors was carried out using moving reference frames, sliding meshes and periodic modeling approaches.

After the analysis of the noise source type and location, two main methods were investigated and compared: Steady (Gutin) and Unsteady formulation of FW-H analogy, both with solid surface of integration. The first method is very efficient as it can be used with a 3D periodic RANS simulation, while the latter requires a more expensive unsteady simulation such as a periodic or non-periodic sliding mesh approach. Comparison with experiments were performed for two and four blade NACA propellers at different rotational speeds, using the different methods explained above. Good agreement was found with the most inexpensive computational approach, i.e. the 3D RANS simulation with the Gutin model, at medium and higher rotational speeds (errors were around 1-2 dB). At lower rotational speeds, the vortex noise component was not well predicted by the steady state approach with the Gutin model. For this reason, a sliding mesh URANS simulation which accurately reproduced the experimental facility using the full FW-H analogy was performed. These simulations improved the results considerably but they were still in poor agreement with the experimental data. It is thought that a much more expensive and accurate unsteady simulation would be needed to improve upon these results. Steady-state simulations are relatively inexpensive, requiring 1 day on a modern

quad core PC, while unsteady sliding mesh simulations required use of a 16 processor PC cluster for about 3-4 CPU days. Although this is considered computationally expensive, it is still affordable within an industrial environment. Such a sliding mesh approach is the only one available to guarantee the accurate analysis of a complex configuration such as a wing installed aircraft propeller. Future work on propeller aeroacoustics will be continued as today there is a strong interest in this field.

Another important aeroacoustics problem encountered in aeronautical engineering was studied here: the jet noise. The noise emitted by the exhaust plume from a gas turbine engine continues to be a significant contributor to the total sound radiated from current commercial airplanes. This is expected to be a bigger problem for future commercial supersonic flights with lower bypass ratio engines. A methodology was developed for predicting this phenomenon. In this case, due to the fact that the sound receivers are positioned quite far from the jet and no large obstacles are present in the domain, the FW-H analogy is the best choice of acoustics model. In this case, the permeable formulation should be applied as no solid surfaces are present, and because the noise sources are all due to the turbulence inside the jet. The Mach number of the jet investigated here was 0.9.

It was suggested to first perform a 2D URANS axisymmetric simulation to verify where to position the FW-H permeable surface. Guidelines were given for designing the fluid domain and the computational grid. In this case, the acoustic analogy was applied, but inside the FW-H surface a full CAA simulation was carried out in order to capture the transmission of all the acoustic pressure fluctuations up to the permeable surface.

An accurate compressible LES simulation was performed, and results compared to measurements. It can be seen that the agreement is satisfactory in terms of trends and absolute values for both the microphones at 150° and 90° to the jet axis. The absolute computed SPL values for the 150° microphone are within a few dB up to a Strouhal number of about 1. A small shift is observed in the SPL peak compared to experimental values. Results at 90° are slightly over-predicted, but the overall trends are predicted very well. Post-processing of the simulation data has clearly shown the fundamental physics of the jet, highlighting the potential core, the mixing region and the area of major noise sources. A *Q*-criterion iso-surface visualization illustrated the turbulent length scale structure of the jet in great detail. This simulation was run on a 16 processor PC cluster for about 5-6 days. It was shown that the information gained by this LES simulation could not have been realized using a cheaper URANS simulation.

References

[1]   Lighthill, M. J., "On Sound Generated Aerodynamically, I. General Theory", *Proceedings of the Royal Society of London*, Vol. A211, No 1107, pp. 564-587, 1952.

[2]   Lighthill, M. J., "On Sound Generated Aerodynamically, II. Turbulence as a source of sound", *Proceedings of the Royal Society of London*, Vol. A222, No 11048, pp. 1-32, 1954.

[3]   Curle, N., "The Influence of Solid Boundaries upon Aerodynamic Sound", *Proceedings of the Royal Society of London*, Vol. A231, pp. 505-514, 1955.

[4]   Crighton, D.G., "Basic principles of aerodynamic noise generation", *Prog. Aerospace Sci.*, 16:31-96, 1975.

[5]   Howe, M.S., "Theory of Vortex Sound", *Cambridge University Press*, 2003.

[6]   J.E. Ffowcs Williams, D.L. Hawkings, "Sound generated by turbulence and surfaces in arbitrary motion", *Philosophical Transaction of the Royal Society*, A 264, No 1151, pp. 321-342, 1969.

[7]   Colonius, T., Lele, S.K., "Computational aeroacoustics: progress on non linear problems of sound generation", *Progress in Aeorspace Sciences*, Vol. 40, pp. 345-416, 2004.

[8]   Brentner, K.S., Farassat, F., "An Analytical Comparison of the Acoustic Analogy and Kirchhoff Formulations for Moving Surfaces", *AIAA Journal*, Vol. 36, pp. 1379-1386, 1998.

[9] Rodi, W., Ferziger, Breuer, J. H., Pourquie, M. M., *"Status of Large Eddy Simulation: Results of a Workshop"*, *Journal of Fluids Engineering*, Vol. 119, June 1997.

[10] Bakker, A., "Lessons of Applied Computational Fluid Dynamics", Fluent Inc., 2002

[11] Cox, J. S., Rumsey, C. L., Brentner, K. S., and Younis, B. A., "Computation of Sound Generated by Viscous Flow Over a Circular Cylinder", *NASA Technical Memorandum,* N. 110339, 1997.

[12] Morkovin, M. V., "Flow Around a Circular Cylinder - A Kaleidoscope of Challenging Fluid Phenomena", *ASME Symposium on Fully Separated Flows,* pp. 102-118, 1964.

[13] Zdravkovich, M. M., "Conceptual Overview of Laminar and Turbulent Flows Past Smooth and Rough Circular Cylinders", *Journal of Wind Engineering and Industrial Aerodynamics,* Vol. 33, pp. 53-62, 1990.

[14] Roshko, A., "Experiments on the Flow Past a Circular Cylinder at Very High Reynolds Number", *Journal of Fluid Mechanics,* Vol. 10, No. 2, pp. 345-356, 1961.

[15] Achenbach, E., and Heinecke, E., "On Vortex Shedding from Smooth and Rough Cylinders in the Range of Reynolds Numbers 6×10^3 to 5×10^6", *Journal of Fluid Mechanics,* Vol. 109, pp. 239-251, 1981.

[16] Schlichting, H., "Boundary-Layer Theory", McGraw-Hill Series in Mechanical Engineering, McGraw-Hill, New York, Seventh edition, Translated by J. Kestin, 1979.

[17] Blackburn, H. M., and Melbourne, W. H., "The Effect of Free-Stream Turbulence on Sectional Lift Forces on a Circular Cylinder", *Journal of Fluid Mechanics,* Vol. 306, pp. 267-292, 1996.

[18] Alemdaroglu, N., Rebillat, J. C., and Goethals, R., "An Aeroacoustic Coherence Function Method Applied to Circular Cylinder Flows", *Journal of Sound and Vibration,* Vol. 69, No. 3 , pp. 427-439, 1980.

[19] Mittal, R., and Balachandar, S., "Effect of Three-Dimensionality on the Lift and Drag of Nominally Two-Dimensional Cylinders", *Physics of Fluids*, Vol. 7, No. 8, pp. 1841-1865, Aug. 1995.

[20] Belov, A., Jameson, A., and Martinelli, L., "Three-Dimensional Unsteady Incompressible Flow Calculations Using Multigrid", *AIAA* paper 97-0443, Jail. 1997.

[21] Franke, R., Rodi, W., and Schonung, B., "Numerical Calculation of Laminar Vortex-Shedding Flow Past Cylinders", *Journal of Wind Engineering and Industrial Aerodynamics,* Vol. 35, pp. 237-257, 1990.

[22] Revell, J. D., Prydz, R. A., and Hays, A. P., "Experimental Study of Airframe Noise vs. Drag Relationship for Circular Cylinders", *Lockheed Report,* No. 28074, Final Report for NASA Contract NAS1-14403, Feb. 1977.

[23] "Aeroacoustics of Flight Vehicles: Theory and Practice", *NASA Reference Publication,* No. 1258, Vol. 1 WRDC Technical Report 90-3052, 1991.

[24] Brooks, T. F., Pope, D. S., and Marcolini, M. A, "Airfoil Self-Noise and Prediction", *NASA Reference Publication*, No. 1218, 1989.

[25] Camel, M. M., Morgan, F. G. Jr., and Coppolino D. A. "Effect of Compressibility and Camber as Determined from an Investigation of the NACA 4-(3) (08) -03 and 4-(5)(08) -03 Two-Blade Propellers up to Forward Mach Numbers of 0.925", *NACA RM*, No. L50D28, Langley Aeronautical Laboratory, Langley Air Force Base, Va, 1950.

[26] Hicks, C. H., and Hubbard, H. H., "Comparison of Sound Emission from Two-Blade, Four-Blade and Seven-Blade Propellers", *NACA Technical Note*, No. 1354, 1947.

[27] Garrick, L. E., and Watkins, C. E., "A Theoretical Study on the Effect of Forward Speed on the Free-Space Sound-Pressure Field Around Propellers", *NACA Technical Note*, No. 3018, 1953.

[28] Stefko, G. L., Jeracki, R. J., "Wind Tunnel Results of Advanced High Speed Propellers in the Takeoff, Climb and Landing Operating Regimes", *Nasa TM*, No. 87054, , Lewis Research Center, Cleveland Ohio, 1985.

[29] Jeracki, R. J., Mikkelson, D. C., Blaha, B. J., "Wind Tunnel Performance of Four Energy Efficient Propellers Designed for Mach 0.8 Cruise", *Nasa TM*, No. 79124, Lewis Research Center, Cleveland Ohio, 1979.

[30] Mikkelson, D. C., Blaha, B. J., Mitchell, G. A., Wikete, J. E., "Design and Performance of Energy Efficient Propellers for Mach 0.8 Cruise", *Nasa TMX*, No. *73612*, Lewis Research Center, Cleveland Ohio, 1977.

[31] Dittmar, J. H., "Cruise Noise of the SR-2 Model in a Wind Tunnel", *NASA Technical Memorandum*, No. 101480, Lewis Research Center Cleveland, Ohio, 1989

[32] Nelson, P. A., Halliway, N. A., and Doak, P. E., ''Fluid dynamics of flow excited resonance. I. Experiment'', *Journal of Sound and Vibration*, Vol. 78, pp. 15–27, 1981.

[33] Nelson, P. A., Halliway, N. A., and Doak, P. E., ''Fluid dynamics of flow excited resonance. II. Flow excited resonance'', *Journal of Sound and Vibration*, Vol. 91, pp. 375–385, 1983.

[34] Rossiter, J. E., "Wind tunnel experiments on the flow over rectangular cavities at subsonic and transonic speed", *Aero. Res. Counc. R. & M.*, No. 3438, 1964.

[35] Inagaki, M., Murata, O., Kondoh, T., and Abe, K.,''A flow excitation of acoustic resonance'', *AIAA Journal*, No. 40.9, pp. 1823–1830, 2002.

[36] "Fourth Computational Aeroacoustics (CAA) Workshop on Benchmark Problems", *NASA/CP*, No. 2004-212954, 2004.

[37] Panda, J., Seasholtz, G. R., Elam, K. A., Mielke, A. F., Eck, D. G., "Effect of Heating on Turbulent Density Fluctuations and Noise Generation From High Speed Jets", *NASA/TM*, No. 2004-213126, Glenn Research Center, 2004.

[38] Tanna, H. K., Dean, P. T., and Burrin, R. H., "The generation and radiation of supersonic jet noise, Vol. III Turbulent Mixing Noise data", *Air Force Aero-Propulsion Laboratory Report AFAPL-TR-65,* 1976.

[39] McDufford, M. D., "Identification of Noise Sources in a Heated Jet Flow", *Thesis*, The Ohio State University, 2006.

[40] Hileman, J., "Large-Scale Structures and Noise Generation in High-Speed Jets", *Diss. The Ohio State University*, 2004.

[41] Antoine, N., "Aircraft Noise Overview," *Stanford University*, 2000.

[42] Hansen, C. H., "Fundamentals of Acoustics", *Lecture Notes*, Department of Mechanical Engineering, University of Adelaide.

[43] Bies, D. A., and Hansen, C. H., "Engineering noise control: theory and practice", *2nd edn. London: E. & F.N. Spon.*, 1996.

[44] De Gennaro, M., "Numerical Approaches for the Full Navier-Stokes Simulation of Rotating Objects" (in Italian), *Master Thesis in Aerospace Engineering*, Università degli Studi di Napoli Federico II, A.A. 2006-2007.

[45] Petrone, G., "Large Eddy Simulation for Aeroacoustics and Aerodynamics", *Master Thesis in Aerospace Engineering*, Università degli Studi di Napoli Federico II, A.A. 2007-2008.

[46] "FLUENT 6.3 User's Guide", *Fluent User's Guide*, ANSYS FLUENT, 2006.

[47] Hirschberg, A., and Rienstra, S. W., "An Introduction to Aeroacoustics", *Lecture Notes*, Eindhoven University of Technology, Jul 2004

[48] Sovani, S., Seibert, W., Ehlen, M., "Simulation of Transient Aerodynamics – Predicting Buffeting, Roaring and Whistling using CFD", *MIRA International Vehicle Aerodynamics Conference*, 2004.

[49] Migliore, P., Oerlemans, S., "Wind Tunnel Aeroacoustic Tests of Six Airfoils for Use on Small Wind Turbines", *AIAA Wind Energy Symposium Reno, Nevada*, 2004.